

University of Wollongong

Research Online

Faculty of Science, Medicine and Health -
Papers: part A

Faculty of Science, Medicine and Health

1-1-2016

Revised stratigraphy and chronology for Homo floresiensis at Liang Bua in Indonesia

Thomas Sutikna

University of Wollongong, ts788@uowmail.edu.au

Matthew W. Tocheri

Smithsonian National Museum of Natural History, tocherim@si.edu

Michael J. Morwood

University of Wollongong, mikem@uow.edu.au

E Wahyu Saptomo

University of Wollongong

- Jatmiko

University of Wollongong

Follow this and additional works at: <https://ro.uow.edu.au/smhpapers>

See next page for additional authors



Part of the [Medicine and Health Sciences Commons](#), and the [Social and Behavioral Sciences Commons](#)

Recommended Citation

Sutikna, Thomas; Tocheri, Matthew W.; Morwood, Michael J.; Saptomo, E Wahyu; Jatmiko, -; Awe Due, Rokus; Wasisto, Sri; Westaway, Kira E.; Aubert, Maxime; Li, Bo; Zhao, J -X; Storey, Michael; Alloway, Brent V.; Morley, Mike W.; Meijer, Hanneke J.M; van den Bergh, Gerrit D.; Grün, Rainer; Dosseto, Anthony; Brumm, Adam R.; Jungers, William L.; and Roberts, Richard G., "Revised stratigraphy and chronology for Homo floresiensis at Liang Bua in Indonesia" (2016). *Faculty of Science, Medicine and Health - Papers: part A*. 3778.

<https://ro.uow.edu.au/smhpapers/3778>

Research Online is the open access institutional repository for the University of Wollongong. For further information contact the UOW Library: research-pubs@uow.edu.au

Revised stratigraphy and chronology for *Homo floresiensis* at Liang Bua in Indonesia

Abstract

Homo floresiensis, a primitive hominin species discovered in Late Pleistocene sediments at Liang Bua (Flores, Indonesia)^{1, 2, 3}, has generated wide interest and scientific debate. A major reason this taxon is controversial is because the *H. floresiensis*-bearing deposits, which include associated stone artefacts^{2, 3, 4} and remains of other extinct endemic fauna^{5, 6}, were dated to between about 95 and 12 thousand calendar years (kyr) ago^{2, 3, 7}. These ages suggested that *H. floresiensis* survived until long after modern humans reached Australia by ~50 kyr ago^{8, 9, 10}. Here we report new stratigraphic and chronological evidence from Liang Bua that does not support the ages inferred previously for the *H. floresiensis* holotype (LB1), ~18 thousand calibrated radiocarbon years before present (kyr cal. bp), or the time of last appearance of this species (about 17 or 13-11 kyr cal. bp)^{1, 2, 3, 7, 11}. Instead, the skeletal remains of *H. floresiensis* and the deposits containing them are dated to between about 100 and 60 kyr ago, whereas stone artefacts attributable to this species range from about 190 to 50 kyr in age. Whether *H. floresiensis* survived after 50 kyr ago-potentially encountering modern humans on Flores or other hominins dispersing through southeast Asia, such as Denisovans^{12, 13}-is an open question.

Disciplines

Medicine and Health Sciences | Social and Behavioral Sciences

Publication Details

Sutikna, T., Tocheri, M. W., Morwood, M. J., Saptomo, E. Wahyu., Jatmiko, , Due Awe, R., Wasisto, S., Westaway, K. E., Aubert, M., Li, B., Zhao, J., Storey, M., Alloway, B. V., Morley, M. W., Meijer, H. J.M., van den Bergh, G. D., Grün, R., Dosseto, A., Brumm, A., Jungers, W. L. & Roberts, R. G. (2016). Revised stratigraphy and chronology for *Homo floresiensis* at Liang Bua in Indonesia. *Nature*, 532 (7599), 366-369.

Authors

Thomas Sutikna, Matthew W. Tocheri, Michael J. Morwood, E Wahyu Saptomo, - Jatmiko, Rokus Awe Due, Sri Wasisto, Kira E. Westaway, Maxime Aubert, Bo Li, J -X Zhao, Michael Storey, Brent V. Alloway, Mike W. Morley, Hanneke J.M Meijer, Gerrit D. van den Bergh, Rainer Grün, Anthony Dosseto, Adam R. Brumm, William L. Jungers, and Richard G. Roberts

Revised stratigraphy and chronology for *Homo floresiensis* at Liang Bua in Indonesia

Thomas Sutikna^{1,2*}, Matthew W. Tocheri^{3,4*}, Michael J. Morwood^{1,‡}, E. Wahyu Saptomo^{2,1}, Jatmiko^{2,1}, Rokus Due Awe^{2,1,‡}, Sri Wasisto², Kira E. Westaway⁵, Maxime Aubert^{6,7}, Bo Li¹, Jian-xin Zhao⁸, Michael Storey⁹, Brent V. Alloway^{10,1}, Mike W. Morley¹, Hanneke J. M. Meijer^{11,12,4}, Gerrit D. van den Bergh¹, Rainer Grün¹³, Anthony Dosseto¹⁴, Adam Brumm^{13,7}, William L. Jungers¹⁵, Richard G. Roberts¹

¹ Centre for Archaeological Science, School of Earth and Environmental Sciences, University of Wollongong, Wollongong, New South Wales 2522, Australia.

² Pusat Penelitian Arkeologi Nasional, Jakarta 12510, Indonesia.

³ Department of Anthropology, Lakehead University, Thunder Bay, Ontario P7B 5Z5, Canada.

⁴ Human Origins Program, National Museum of Natural History, Smithsonian Institution, Washington DC 20013, USA.

⁵ Traps MQ Luminescence Dating Facility, Department of Environmental Sciences, Macquarie University, Sydney, New South Wales 2109, Australia.

⁶ Research Centre for Human Evolution, Place, Evolution and Rock Art Heritage Unit, Griffith University, Gold Coast, Queensland 4222, Australia.

⁷ School of Earth and Environmental Sciences, University of Wollongong, Wollongong, New South Wales 2522, Australia.

⁸ School of Earth Sciences, University of Queensland, Brisbane, Queensland 4072, Australia.

⁹ QUADLAB, Earth and Planetary System Science, Natural History Museum of Denmark, 1350 Copenhagen, Denmark.

¹⁰ School of Geography, Environment and Earth Sciences, Victoria University of Wellington, Wellington 6012, New Zealand.

¹¹ Department of Ornithology, Senckenberg Forschungsinstitut und Naturmuseum, 60325 Frankfurt, Germany.

¹² University Museum, Department of Natural History, University of Bergen, 5007 Bergen, Norway.

¹³ Research Centre for Human Evolution, Environmental Futures Research Institute, Griffith University, Brisbane, Queensland 4111, Australia.

¹⁴ GeoQuEST Research Centre, School of Earth and Environmental Sciences, University of Wollongong, Wollongong, New South Wales 2522, Australia.

¹⁵ Department of Anatomical Sciences, Stony Brook University Medical Center, Stony Brook, New York 11794, USA.

‡ Deceased.

* These authors contributed equally to this work.

Correspondence and requests for materials should be addressed to T.S. (thomasutikna@gmail.com), M.W.T. (tocherim@gmail.com), and R.G.R. (rgrob@uow.edu.au).

Homo floresiensis, a primitive hominin species discovered in Late Pleistocene sediments at Liang Bua (Flores, Indonesia)¹⁻³, has generated wide interest and scientific debate. A major reason this taxon is controversial is because the *H. floresiensis*-bearing deposits, which include associated stone artefacts²⁻⁴ and remains of other extinct endemic fauna^{5,6}, were dated to between about 95 and 12 thousand calendar years (kyr) ago^{2,3,7}. These ages suggested that *H. floresiensis* survived until long after modern humans reached Australia by ~50 kyr ago⁸⁻¹⁰. Here we report new stratigraphic and chronological evidence from Liang Bua that does not support the ages inferred previously for the *H. floresiensis* holotype (LB1), ~18 thousand calibrated radiocarbon years before present (kyr cal. BP), or the time of last appearance of this species (about 17 or 13–11 kyr cal. BP)^{1-3,7,11}. Instead, the skeletal remains of *H. floresiensis* and the deposits containing them are dated to between about 100 and 60 kyr ago, while stone artefacts attributable to this species range from about 190 to 50 kyr in age. Whether *H. floresiensis* survived after 50 kyr ago—potentially encountering modern humans on Flores or other hominins dispersing through Southeast Asia, such as Denisovans^{12,13}—is an open question.

The 2001–2004 excavations at Liang Bua (Fig. 1) revealed the skeletal remains of *H. floresiensis*^{1-3,14-20} at 4–7 m depth in multiple excavated areas (referred to here as Sectors). Charcoal samples collected from similar depths near the eastern wall of the cave (Sector VII) were dated to between about 19 and 13–11 kyr cal. BP^{2,3,7}, whereas an age of ~74 kyr was obtained by coupled electron-spin resonance/uranium-series dating of a *Stegodon florensis insularis* molar recovered from ~4.5 m depth from near the cave centre (Sector IV)^{2,7}. This molar was found ~30 cm below a *H. floresiensis* premolar and ulna (LB2) and ~20 cm and ~130 cm above other postcranial remains (LB10 and LB3, respectively)¹⁸.

The 2007–2014 excavations between and slightly south of these Sectors (Fig. 1c) have revealed new stratigraphic details that are crucial for (re)interpreting the ages inferred originally for *H. floresiensis* (Extended Data Fig. 1 and Supplementary video 1). The *H. floresiensis*-bearing deposits consist of multiple layers of fine-grained sediment interstratified by layers of weathered limestone, speleothem and loose gravel (Extended Data Fig. 2). These deposits are conformably overlain by a ~2 m-thick sequence of five tephras (referred to here as T1–T5; Extended Data Fig. 3 and Supplementary Information section 1), separated by clastic sediments and flowstones (Fig. 2). This stratigraphic sequence forms a large pedestal that extends ~12 m laterally from the eastern wall to the cave centre, and is at least 6 m long from north to south. The pedestal is thickest (~4 m) in the middle rear of the cave, where it extends to within ~2 m of the present surface of the cave floor.

The pedestal deposits have been truncated by one or more phases of erosion, resulting in an erosional surface (i.e., an unconformity) that slopes steeply down towards the cave mouth (Fig. 3 and Extended Data Figs 4 and 5). The specific timing and nature of the erosional events responsible for this unconformity remain unknown, but presumably include slopewash and other hydrogeological mechanisms, given the active karst setting of the cave. This unconformity was not recognised during the 2001–2004 excavations, raising serious questions about the accuracy of previous age estimates^{2,3,7} for *H. floresiensis*, which were based on inferred stratigraphic associations. To address these questions, we have applied several dating methods to the main stratigraphic units within this pedestal and to the skeletal remains of *H. floresiensis* and other fauna derived from this depositional sequence (see Supplementary Information sections 2–6 for details of each dating method).

Sediment samples for infrared stimulated luminescence (IRSL) and thermoluminescence (TL) dating^{21,22} (Extended Data Figs 6 and 7) were collected from the *H. floresiensis*-bearing deposits directly underlying T1 in the south baulks of Sectors XXI and XXIII, more than 2 m south of the erosional unconformity. These samples gave statistically indistinguishable weighted mean IRSL and TL ages ($\pm 1\sigma$) of 65 ± 5 kyr (LB12-OSL3 to -OSL6) and 71 ± 13 kyr (LB12-23-2 and -4), respectively, for the time since sand-sized grains of feldspar and quartz were last exposed to sunlight. A TL age of 89 ± 7 kyr (LB08-15-3) was obtained for the basal *H. floresiensis*-bearing deposits in Sector XV, while two further samples from the immediately underlying, gravel-rich layer (in Sectors XXI and XXIII) gave IRSL and TL ages of 128 ± 17 kyr (LB12-OSL7) and 113 ± 9 kyr (LB12-23-1), respectively. We also used $^{234}\text{U}/^{230}\text{Th}$ methods to date four samples of *in situ* speleothem from the *H. floresiensis*-bearing deposits in Sectors XII and XVII (LB07-SXII-F4 and LB09-SXVII-F1 to -F3), which gave ages ($\pm 2\sigma$) of between 80.8 ± 0.8 and 58.3 ± 0.5 kyr.

Three *H. floresiensis* ulnae and seven *Stegodon* bones were sampled for $^{234}\text{U}/^{230}\text{Th}$ dating, as well as a modern human femoral shaft fragment from the Holocene deposits in Sector IV (Extended Data Figs 8 and 9). Owing to the open system behaviour of bone, such analyses usually yield minimum ages for bone deposition and subsequent uranium uptake²³. The modelled age²⁴ of ~ 7.5 kyr for the modern human bone (132A/LB/IV/27D/03) is consistent with charcoal ^{14}C ages for the underlying and overlying sediments (about 9.5 and 6.4 kyr cal. BP, respectively⁷). The *H. floresiensis* ulnae have modelled $^{234}\text{U}/^{230}\text{Th}$ ages ($\pm 2\sigma$) for individual laser-ablation tracks that range from 86.9 ± 7.9 to 71.5 ± 4.3 kyr for LB1 (Sectors VII and XI), 71.4 ± 1.1 to 66.7 ± 0.8 kyr for LB2 (Sector IV), and 66.0 ± 4.3 to 54.6 ± 2.1 kyr for LB6 (Sector XI). The *Stegodon* bone samples (all from Sector XI) span a modelled age range of 80.6 ± 11.3

to 40.5 ± 2.0 kyr, with the youngest minimum age deriving from a bone (U-s-05/LB/XI/51/04) recovered from the same sediments and depth as LB6. Delayed diffusion of uranium into the dense bone matrix of *Stegodon* may account for the youngest minimum ages appearing more recent than those obtained for the bones of *H. floresiensis*, the speleothems and the sediments.

We dated T1, which directly overlies the *H. floresiensis*-bearing deposits, using $^{40}\text{Ar}/^{39}\text{Ar}$ methods^{25,26}. The inverse isochron age ($\pm 1\sigma$) of 79 ± 12 kyr (Extended Data Fig. 3) is imprecise due to the low yield of radiogenic argon from the hornblende crystals, but the 2σ age range (103–55 kyr) is consistent with the luminescence and $^{234}\text{U}/^{230}\text{Th}$ ages for the underlying samples. Immediately overlying T1 is a series of interstratified sedimentary units, including T2 and several flowstones. These are in turn overlain by T3, a ~0.75 m-thick volcanoclastic mass flow deposit, formerly referred to as the ‘black tuff’ or similar^{18,27}.

Sediments between T2 and T3 in Sector XXI yielded a weighted mean IRSL age of 66 ± 9 kyr (LB12-OSL1 and -OSL2) and a TL age of 59 ± 13 kyr (LB12-23-3). Interbedded flowstones and a small stalagmite in the same Sector gave $^{234}\text{U}/^{230}\text{Th}$ ages of between 66.1 ± 0.3 and 54.4 ± 0.3 kyr (LB-S.XXI 5 #08, LB-S.XXI 8-T #09 and 8-B #10, and LB/S.XXI 10-01 and -01R), while in Sector XII—nearer the cave centre—a flowstone immediately underlying T3 (LB07-SXII-F1) was dated to 49.6 ± 0.5 kyr. Hominin skeletal remains have not been recovered from the deposits between T2 and T3. However, stone artefacts are present and these display similar raw material proportions to those found underneath T1 (~80% silicified tuff and ~20% chert), in contrast to the preference of modern humans for chert (~60%) observed at Liang Bua during the Holocene⁴. Also present in these sediments and those underlying T1 are the remains of other extinct large-bodied taxa, including *Stegodon*, giant marabou stork and vulture^{5,6}. The specific

processes that ultimately resulted in the extinction of these taxa and *H. floresiensis* remain poorly understood.

Overlying T3 is T4, which is covered by loose, coarse gravel in two of the southernmost Sectors excavated (XII and XXVII). Three flowstone samples^{7,28} (weighted mean $^{234}\text{U}/^{230}\text{Th}$ age of 46.6 ± 0.5 kyr) directly overlie the southern parts of this coarse gravel layer. From the eastern wall to the cave centre, T4 is overlain by two flowstone layers that are separated from each other by T5. At 1.89 m depth in Sector XXIII, charcoal (sample OxA-X-2648-13) from immediately above the upper surface of T5 yielded a ^{14}C age of ~ 46 kyr cal. BP (95% confidence interval of 47.7–44.1 kyr cal. BP).

In contrast, all of the charcoal samples used previously to infer ages of ~ 18 kyr cal. BP for LB1 and about 17 or 13–11 kyr cal. BP as the *terminus ante quem* for *H. floresiensis* and *Stegodon*^{2,3,5,7} originate from deposits that unconformably overlie the remnant pedestal, based on their plotted coordinates (Fig. 3). These younger sediments are interstratified by three additional tephra (T6–T8; Extended Data Fig. 10). Tephra T6 is observed at ~ 5.8 m depth in the northern parts of Sectors VII and XVI, followed by T7 and T8 (formerly referred to as the ‘white’ tuffaceous silts^{2,3,18,27}) at about 3.5–5 m depth (Sectors III, IV, VII, XI, XV, XVI and XXII). The onset of accumulation of the depositional sequence above the unconformity ~ 20 kyr ago is consistent with a TL age of 23 ± 7 kyr for sediments collected less than 15 cm above the unconformity in Sector XVI (LB09-16-2) and two new ^{14}C ages of ~ 12.7 kyr cal. BP for charcoal recovered from just beneath T7 in Sector XXII (D-AMS 005953 and 005954).

Portions of the pedestal have been reworked into this younger depositional sequence. In Sector XXII, a displaced slab of intact pedestal deposit rests above the unconformity but underlies T7 (Extended Data Fig. 10c, d). In other Sectors, eroded fragments of T1, T2 and T3

are consistently observed in the younger, overlying deposits^{2,3,18}. We investigated the possibility that the luminescence ages for the sediment samples collected in 2003 from alongside LB1 and ~1 m above it² were compromised by inadvertently sampling across the unconformity and measuring multiple grains simultaneously from this mixture. The wide spread in ages (from about 170 to 10 kyr ago) obtained for individual feldspar grains using newly developed IRSL dating procedures²¹ supports this suggestion (Extended Data Fig. 7k, l).

The new stratigraphic and chronological evidence for Liang Bua indicates that a pedestal of remnant deposits, dating to more than ~46 kyr cal. BP, has an erosional upper surface that slopes steeply downwards to the north and is unconformably overlain by sediments younger than ~20 kyr cal. BP. All skeletal remains assigned to *H. floresiensis* are from the pedestal deposits dated to approximately 100–60 kyr ago, while stone artefacts reasonably attributable to this species range from about 190 kyr²⁸ to 50 kyr in age. Parts of Southeast Asia may have been inhabited by Denisovans^{12,13} or other hominins^{29,30} during this period, and modern humans had reached Australia by 50 kyr ago^{8–10}. But whether *H. floresiensis* survived after this time, or encountered modern humans, Denisovans or other hominin species on Flores or elsewhere, remain open questions that future discoveries may help answer.

References

1. Brown, P. *et al.* A new small-bodied hominin from the Late Pleistocene of Flores, Indonesia. *Nature* **431**, 1055–1061 (2004).
2. Morwood, M. J. *et al.* Archaeology and age of a new hominin from Flores in eastern Indonesia. *Nature* **431**, 1087–1091 (2004).
3. Morwood, M. J. *et al.* Further evidence for small-bodied hominins from the Late Pleistocene of Flores, Indonesia. *Nature* **437**, 1012–1017 (2005).
4. Moore, M. W., Sutikna, T., Jatmiko, Morwood, M. J. & Brumm, A. Continuities in stone flaking technology at Liang Bua, Flores, Indonesia. *J. Hum. Evol.* **57**, 503–526 (2009).
5. van den Bergh, G. D. *et al.* The Liang Bua faunal remains: a 95 k.yr. sequence from Flores, East Indonesia. *J. Hum. Evol.* **57**, 527–537 (2009).
6. Meijer, H. J. M. *et al.* Late Pleistocene–Holocene non-passerine avifauna of Liang Bua (Flores, Indonesia). *J. Vert. Paleontol.* **33**, 877–894 (2013).
7. Roberts, R. G. *et al.* Geochronology of cave deposits at Liang Bua and of adjacent river terraces in the Wae Racang valley, western Flores, Indonesia: a synthesis of age estimates for the type locality of *Homo floresiensis*. *J. Hum. Evol.* **57**, 484–502 (2009).
8. Roberts, R. G. *et al.* Thermoluminescence dating of a 50,000-year-old human occupation site in northern Australia. *Nature* **345**, 153–156 (1990).
9. Bowler, J. M. *et al.* New ages for human occupation and climatic change at Lake Mungo, Australia. *Nature* **421**, 837–840 (2003).
10. Clarkson, C. *et al.* The archaeology, chronology and stratigraphy of Madjedbebe (Malakunanja II): A site in northern Australia with early occupation. *J. Hum. Evol.* **83**, 46–64 (2015).
11. Morwood, M. J. *et al.* Preface: research at Liang Bua, Flores, Indonesia. *J. Hum. Evol.* **57**, 437–449 (2009).
12. Reich, D. *et al.* Genetic history of an archaic hominin group from Denisova Cave in Siberia. *Nature* **468**, 1053–1060 (2010).
13. Reich, D. *et al.* Denisova admixture and the first modern human dispersals into Southeast Asia and Oceania. *Am. J. Hum. Genet.* **89**, 516–528 (2011).
14. Falk, D. *et al.* The brain of *Homo floresiensis*. *Science* **308**, 242–245 (2005).
15. Larson, S. G. *et al.* *Homo floresiensis* and the evolution of the hominin shoulder. *J. Hum. Evol.* **53**, 718–731 (2007).
16. Tocheri, M. W. *et al.* The primitive wrist of *Homo floresiensis* and its implications for hominin evolution. *Science* **317**, 1743–1745 (2007).
17. Jungers, W. L. *et al.* The foot of *Homo floresiensis*. *Nature* **459**, 81–84 (2009).
18. Morwood, M. J. & Jungers, W. L. (Eds) Paleoanthropological Research at Liang Bua, Flores, Indonesia. *J. Hum. Evol.* **57**, 437–648 (2009).
19. Kaifu, Y. *et al.* Craniofacial morphology of *Homo floresiensis*: description, taxonomic affinities, and evolutionary implication. *J. Hum. Evol.* **61**, 644–682 (2011).
20. Orr, C. M. *et al.* New wrist bones of *Homo floresiensis* from Liang Bua (Flores, Indonesia). *J. Hum. Evol.* **64**, 109–129 (2013).
21. Li, B., Jacobs, Z., Roberts, R. G. & Li, S.-H. Review and assessment of the potential of post-IR IRSF dating methods to circumvent the problem of anomalous fading in feldspar luminescence. *Geochronometria* **41**, 178–201 (2014).

22. Westaway, K. E. & Roberts, R. G. A dual-aliquot regenerative-dose protocol (DAP) for thermoluminescence (TL) dating of quartz sediments using the light-sensitive and isothermally stimulated red emissions. *Quat. Sci. Rev.* **25**, 2513–2528 (2006).
23. Grün, R., Eggins, S., Kinsley, L., Moseley, H. & Sambridge, M. Laser ablation U-series analysis of fossil bones and teeth. *Palaeogeogr. Palaeoclim. Palaeoecol.* **416**, 150–167 (2014).
24. Sambridge, M., Grün, R. & Eggins, S. U-series dating of bone in an open system: the diffusion–adsorption–decay model. *Quat. Geochronol.* **9**, 42–53 (2012).
25. Storey, M., Roberts, R. G. & Saidin, M. Astronomically calibrated $^{40}\text{Ar}/^{39}\text{Ar}$ age for the Toba supereruption and global synchronization of late Quaternary records. *Proc. Natl Acad. Sci. USA* **109**, 18684–18688 (2012).
26. Rivera, T. A., Storey, M., Schmitz, M. D. & Crowley, J. L. Age intercalibration of $^{40}\text{Ar}/^{39}\text{Ar}$ sanidine and chemically distinct U/Pb zircon populations from the Alder Creek Rhyolite Quaternary geochronology standard. *Chem. Geol.* **345**, 87–98 (2013).
27. Westaway, K. E. *et al.* *Homo floresiensis* and the late Pleistocene environments of eastern Indonesia: defining the nature of the relationship. *Quat. Sci. Rev.* **28**, 2897–2912 (2009).
28. Westaway, K. E. *et al.* Establishing the time of initial human occupation of Liang Bua, western Flores, Indonesia. *Quat. Geochron.* **2**, 337–343 (2007).
29. Mijares, A. S. *et al.* New evidence for a 67,000-year-old human presence at Callao Cave, Luzon, Philippines. *J. Hum. Evol.* **59**, 123–132 (2010).
30. van den Bergh, G. D. *et al.* Earliest hominin occupation of Sulawesi, Indonesia. *Nature* **529**, 208–211 (2016).

Acknowledgements

The 2007–2014 excavations at Liang Bua were supported by an Australian Research Council (ARC) Discovery Project grant to M.J.M. (DP0770234), a Waitt Foundation/National Geographic Society grant to M.W.T and T.S. (No. 2121-2) and a Smithsonian Scholarly Studies Program award to M.W.T. Additional funding was provided by the Peter Buck Fund for Human Origins Research, the Smithsonian’s Human Origins Program, the University of Wollongong (UOW) and the ARC (DP1093049 to K.E.W.). T.S. is supported by a UOW postgraduate scholarship, M.W.T. by a Canada Research Chair, M.A. and A.B. by ARC Discovery Early Career Researcher Awards (DE140100254 and DE130101560, respectively), B.L. by an ARC Future Fellowship (FT14010038), R.G.R. by an ARC Australian Laureate Fellowship (FL130100116) and B.V.A. by a Victoria University of Wellington Science Faculty Research Grant (201255). QUADLAB is funded by the Villum Foundation. Fieldwork was authorised by Pusat Penelitian Arkeologi Nasional (Jakarta, Indonesia) and Pemerintah Daerah Kabupaten Manggarai (Flores, Nusa Tenggara Timur). We also thank I Made Geria, Valentinus N. Sene, Rick Potts, Paul Goldberg, Katerina Douka, Grace Veatch, Vince Rossi, Adam Metallo, Les Kinsley, Yasaman Jafari, Terry Lachlan, Ai Duc Nguyen, Dida Yurnaldi, Ruly Setiawan, I Dewa Kompiang and the entire Liang Bua Team from Teras, Golo Manuk and Bere.

Author contributions

M.J.M., R.P. Soejono and R.G.R. conceived and coordinated the original research program at Liang Bua (2001–2004). The new excavations were planned and directed by T.S., E.W.S and M.J.M. (2007–2009), and by T.S., M.W.T., E.W.S, J. and M.J.M. (2010–2014). T.S. led the stratigraphic analyses, with major contributions from M.W.T., S.W., M.J.M., K.E.W., R.D.A.,

E.W.S. and J., and additional input from M.W.M., H.J.M.M., G.D.vdB., B.V.A., A.B., W.L.J. and R.G.R. Dating analyses were conducted by B.L. and R.G.R. (IRSL), K.E.W. (TL), M.A., R.G. and A.D. ($^{234}\text{U}/^{230}\text{Th}$, bones), J.-x.Z. ($^{234}\text{U}/^{230}\text{Th}$, speleothems), and M.S. ($^{40}\text{Ar}/^{39}\text{Ar}$). B.V.A. analysed the volcanic tephra, R.D.A., H.J.M.M., G.D.vdB., M.W.T. and W.L.J. analysed the faunal remains, and J. analysed the stone artefacts. T.S., M.W.T. and R.G.R. wrote the paper, with early contributions from M.J.M and additional input from all other authors.

Author information

Reprints and permissions information is available at www.nature.com/reprints. Correspondence and requests for materials should be addressed to T.S. (thomasutikna@gmail.com), M.W.T. (tocherim@gmail.com) and R.G.R. (rgrob@uow.edu.au).

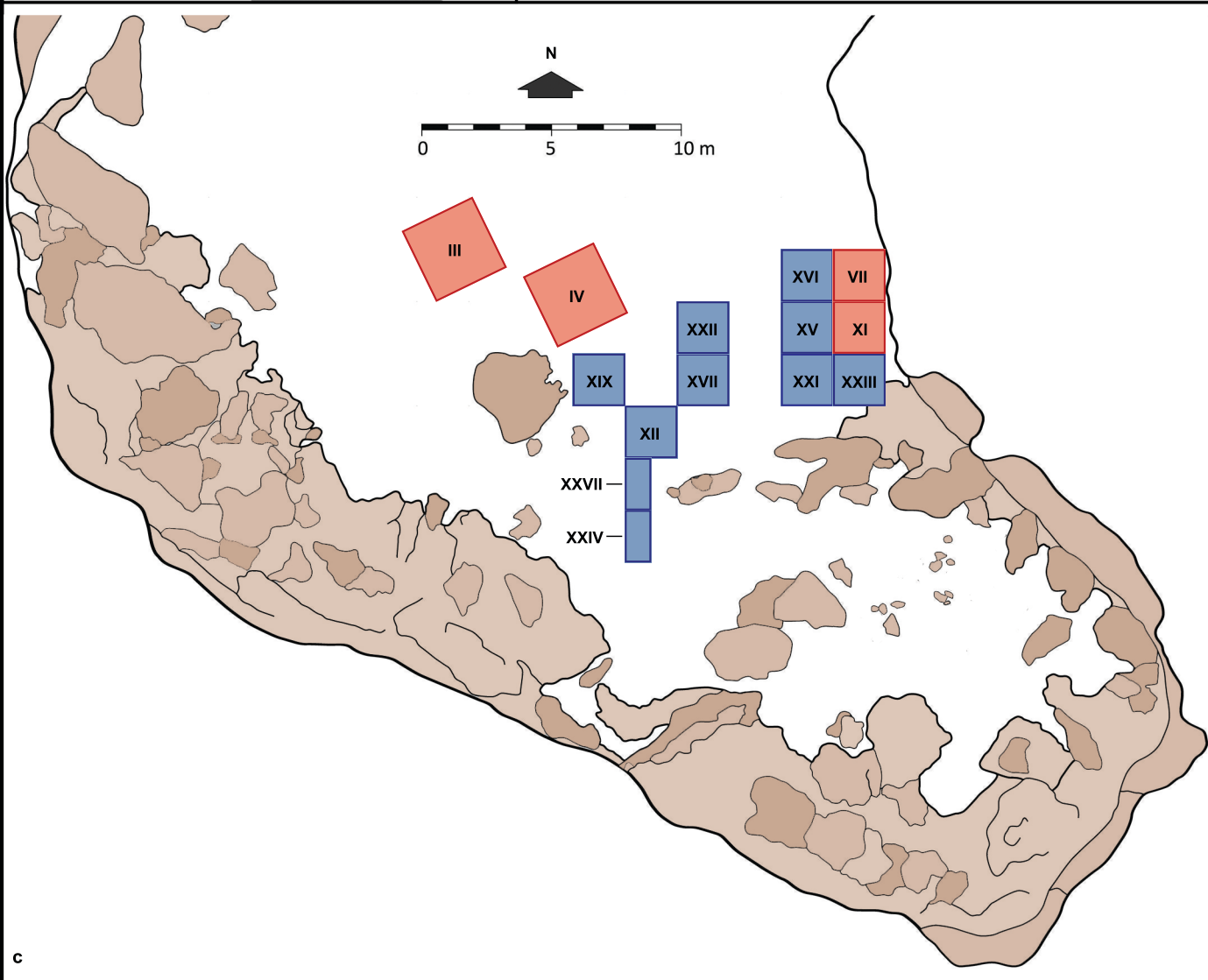
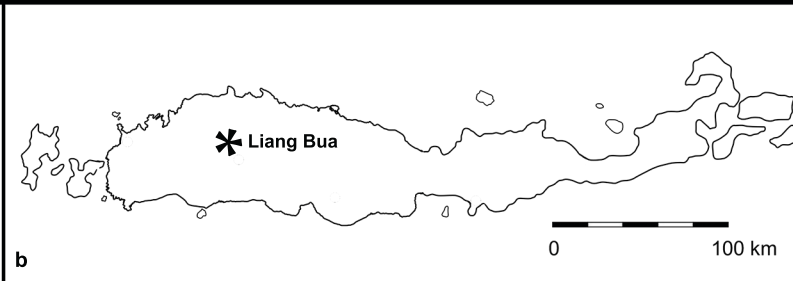
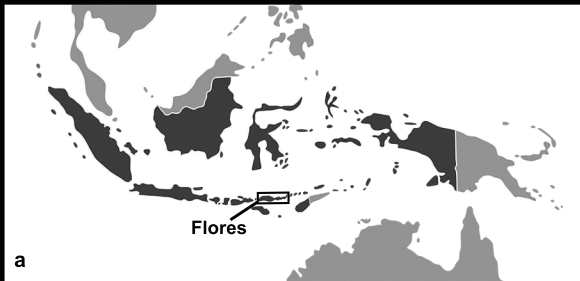
Figure legends

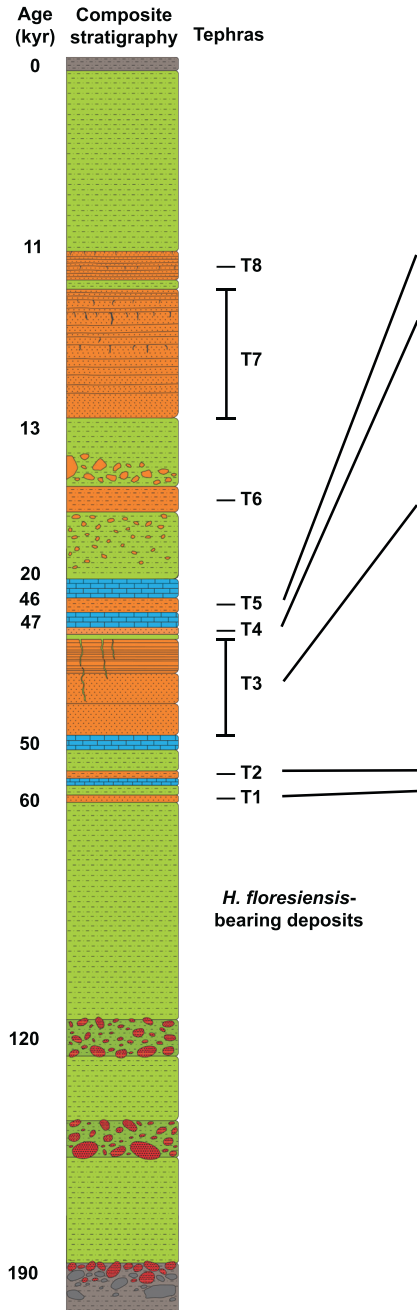
Figure 1 | Site location. **a**, Location of Flores within Indonesia. **b**, Location of Liang Bua on Flores. **c**, Site plan of Sectors discussed in the text (the 2001–2004 and 2007–2014 excavations are shaded red and blue, respectively). The remaining cave floor sediments are shaded white, while the areas shaded brown are exposed rocks, stalagmites and other surfaces covered in speleothems.

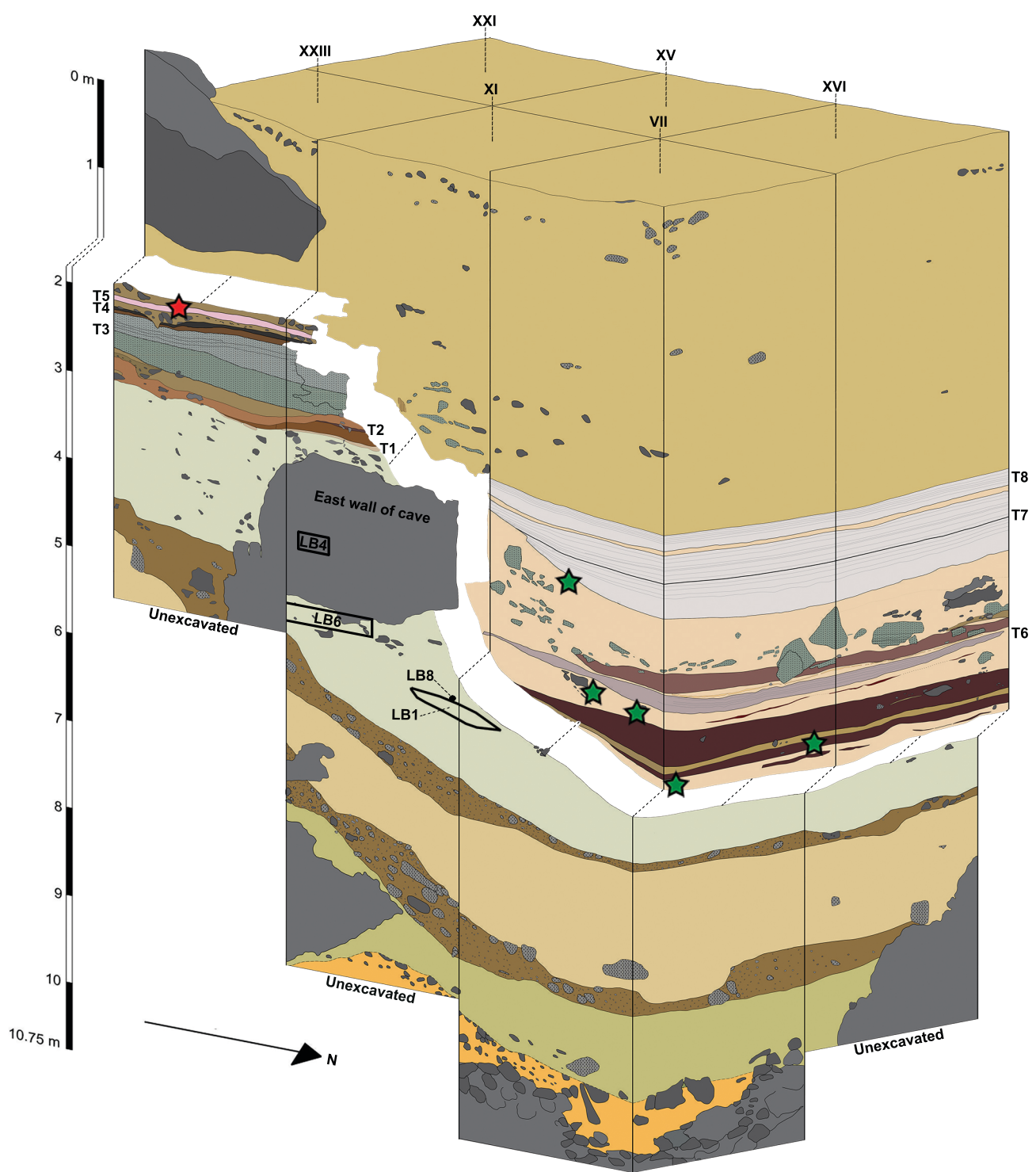
Figure 2 | Composite stratigraphic section of deposits at Liang Bua, with approximate ages.

The deposits accumulated above a fluvial conglomerate and are capped by recent sediments (both shown in grey). Skeletal remains of *Homo floresiensis* occur in deposits stratigraphically beneath a sequence of eight volcanic tephra (T1–T8), separated by calcitic speleothems (blue) and fine-grained clastic sediments (green). As the thickness, grain size and slope angle of each unit vary considerably within the cave, only the approximate relative thicknesses of the units discussed in the text are shown; the minimum depth of this composite section would exceed 15 m. See Fig. 3 and Extended Data Fig. 5a for three-dimensional representations of the stratigraphy. Also indicated are units with concentrations of rounded, gravel-size clasts of igneous rock (red) or irregularly shaped, eroded fragments of T1, T2 and T3 (orange), and units with signs of bioturbation (upper parts of T3 and T7). The photograph shows T1–T5 and interstratified sediments that conformably overlie the *H. floresiensis*-bearing deposits (south baulk of Sector XXI).

Figure 3 | Stratigraphy of excavated Sectors near the eastern wall of the cave. Multiple specimens of *Homo floresiensis* (LB1, LB4, LB6 and LB8) were recovered previously^{1–3,14–20} from sediments now recognised to directly underlie a sequence of five tephra (T1–T5) and interstratified deposits. Together, these remnant deposits form a pedestal, the top of which is dated to ~46 kyr cal. BP (charcoal sample denoted by the red star at ~2 m depth in Sector XXIII). The overlying section—separated here by a white band and dotted lines for emphasis—represents deposits (including three additional tephra, T6–T8) that rest unconformably on the steeply sloping erosional surface of the pedestal. The green stars in Sector VII mark the respective locations (from top to bottom) of the charcoal samples dated to approximately 13.0, 18.5, 18.1, 19.0 and 19.2 kyr cal. BP, which were used erroneously^{2,3,7} to infer the latest occurrences of *H. floresiensis*.







Methods

Archaeological excavation. The 2007–2014 excavations at Liang Bua, including eight 2 x 2 m and two 1 x 2 m areas (referred to as Sectors), proceeded in 10 cm intervals (referred to as spits) while following stratigraphic units. Timber shoring of the baulks was installed after ~2.5 m depth for safety. *In situ* findings (e.g., bone, artefact, charcoal) were plotted in three dimensions and the sediments from each spit were sieved by hand, followed by wet sieving (2 mm mesh). All recovered findings were cleaned, catalogued and transported to the National Centre for Archaeology (Jakarta, Indonesia) for curation and further study.

Electron microprobe analysis of volcanic glass. Bulk samples of four tephras were wet sieved at $>32\text{ }\mu\text{m}$ then dry sieved into $32\text{--}63\text{ }\mu\text{m}$, $63\text{--}125\text{ }\mu\text{m}$, $125\text{--}250\text{ }\mu\text{m}$, $250\text{--}500\text{ }\mu\text{m}$ and $500\text{ }\mu\text{m}\text{--}1\text{ mm}$ fractions. Depending on the grain-size distribution of the sample, the dominant dry fraction containing the most glass material was mounted into an epoxy mount. Glass from bubble-wall shards or vesiculated pumice fragments was analysed as individual grains ($>63\text{ }\mu\text{m}$) using an electron microprobe. Major element determinations were made using a JEOL Superprobe (JXA-8230) housed at Victoria University of Wellington, New Zealand, using the ZAF correction method³¹. Analyses were performed with 15 kV accelerating voltage, 8 nA beam current, and an electron beam defocused to $10\text{--}20\text{ }\mu\text{m}$. Standardisation was achieved by means of mineral and glass standards. Rhyolitic glass standard ATHO-G (ref. 32) was routinely used to monitor calibration in all analytical runs and to evaluate any day-to-day differences in calibration. All analyses were normalised to 100% (by weight) anhydrous and total iron was calculated as FeO (Supplementary Information section 1). The major element compositions of the four tephras and the Youngest Toba Tuff³³ are displayed as bivariate plots in Extended Data Fig. 3.

Infrared stimulated luminescence (IRSL) dating of feldspar grains. Sediment samples were collected using opaque plastic tubes hammered horizontally into cleaned stratigraphic sections and wrapped in black plastic after removal. Field measurements of the gamma dose rates at each sample location were made using a portable gamma-ray detector (Exploranium GR-320) inserted into the emptied tube holes. Sediment samples were also collected from the tube holes for laboratory determinations of water content and beta dose rate at the University of Wollongong. The environmental dose rate of each sample was calculated as the sum of the beta dose rate (estimated from beta-counting of dried and powdered sediment samples using a Risø low-level beta multicounter system and allowing for beta-dose attenuation and other factors³⁴), the *in situ* gamma dose rate, and the estimated cosmic-ray dose rate³⁵. The latter took account of the burial depth of each sample, the thickness of cave roof overhead, the zenith-angle dependence of cosmic rays, and the latitude, longitude and altitude of Liang Bua. Each of these external dose rate contributors were adjusted for long-term water content. The measured (field) water contents of the seven samples collected in 2012 range from 26 to 35%, but higher and lower field water contents have been reported for other sediment samples collected at Liang Bua: 15–30% (ref. 2), 3–22% (ref. 7) and 24–39% (Supplementary Information section 2). We used a value of $20 \pm 5\%$ as a mid-range estimate of the long-term water content, with the standard error sufficient to cover (at 2σ) most of the field measurements. The total dose rate of each sample also includes an estimate of the internal beta dose rate due to the radioactive decay of ^{40}K and ^{87}Rb . This estimate was based on a K concentration of $12 \pm 1\%$, determined from energy- and wavelength-dispersive X-ray spectroscopic measurements of individual feldspar grains^{36,37} (see Supplementary Information section 2), and an assumed Rb concentration of $400 \pm 100\text{ }\mu\text{g g}^{-1}$ (ref. 38).

Potassium-rich feldspar (K-feldspar) grains of 90–212 or 180–212 μm diameter were extracted from the sediment samples under dim red illumination and prepared using standard procedures³⁹, including the use of a sodium polytungstate solution of 2.58 g cm^{-3} density to separate the feldspar grains from heavier minerals. The separated grains were also washed in 10% hydrofluoric acid for 40 min to clean their surfaces and reduce the thickness of the alpha-irradiated outer layer by $\sim 15 \mu\text{m}$, which was taken into account in the dose rate calculation. For each sample, single aliquots composed of a few hundred grains were measured using an automated Risø TL/OSL reader equipped with infrared (875 nm) light-emitted diodes (LEDs) for stimulation⁴⁰ and a calibrated $^{90}\text{Sr}/^{90}\text{Y}$ source for beta irradiations. We also made measurements of individual K-feldspar grains (180–212 μm diameter) from two samples collected in 2012 (LB12-OSL3 and -OSL4) and the two original sediment samples (LBS7-40a and LBS7-42a) collected from above and alongside the remains of LB1 (ref. 2). Infrared stimulation of individual K-feldspar grains was achieved using a focussed laser beam (830 nm)⁴⁰. The IRSL emissions from the single aliquots and single grains were detected using an Electron Tubes Ltd 9235B photomultiplier tube fitted with Schott BG-39 and Corning 7-59 filters to transmit wavelengths of 320–480 nm. To estimate the equivalent dose (D_e) for each aliquot or grain^{39,41}, we initially used the multiple elevated temperature post-infrared IRSL (MET-pIRIR) regenerative-dose procedure^{21,30,42}, in which the IRSL signals are measured by progressively increasing the stimulation temperature from 50 °C to 250 °C in 50 °C increments. The samples yielded very dim signals, however, so we used a two-step pIRIR procedure^{21,43} to improve the signal-to-noise ratio. Grains were preheated at 320 °C for 60 s prior to infrared stimulation of the natural, regenerative and test doses at 50 °C for 200 s. The pIRIR signal was then measured at 290 °C for either 200 s (single aliquots) or 1 s (single grains), followed by an infrared bleach at 325 °C for 100 s at the end of each regenerative-dose cycle. Example pIRIR decay and dose-response curves are shown in Extended Data Fig. 7a–c. Performance tests of the regenerative-dose procedure and details of residual dose measurements^{21,44} and anomalous fading tests^{45,46} are described in Supplementary Information section 2. We estimated the pIRIR age of each sample from the weighted mean D_e (calculated using the central age model^{47,48}) divided by the environmental dose rate, and applied corrections for residual dose and anomalous fading. For the latter corrections, we used the weighted mean fading rate ($0.9 \pm 0.3\%$ per decade) measured for five of the seven samples collected in 2012.

Thermoluminescence (TL) dating of quartz grains. Sediment samples were taken in the same manner as the IRSL samples, as were the *in situ* gamma dose rate measurements (made using an ORTEC digi-DART gamma-ray detector). Additional sediment samples were also collected for determinations of water content and beta dose rate at Macquarie University. The environmental dose rate of each sample consists of three external components, each adjusted for long-term water content ($20 \pm 5\%$): the beta dose rate (estimated from beta-counting and allowing for beta-dose attenuation), the *in situ* gamma dose rate, and the estimated cosmic-ray dose rate. An assumed internal dose rate of $0.03 \pm 0.01 \text{ Gy kyr}^{-1}$ was also included in the total dose rate. Quartz grains were separated from the sediment samples under dim red illumination and prepared using standard procedures³⁹, including mineral separations using 2.70 and 2.62 g cm^{-3} density solutions of sodium polytungstate to isolate the quartz and a 40% hydrofluoric acid etch for 45 min to remove the alpha-irradiated outer $\sim 20 \mu\text{m}$ of each grain. Aliquots composed of about 10,000 quartz grains were measured using a dual-aliquot regenerative-dose TL protocol²² to isolate the light-sensitive red emissions⁴⁹. This procedure was originally developed for application at Liang Bua² and requires two aliquots of each sample: one to estimate the D_e

associated with the heat-reset TL traps and the other to measure the total TL signal, from which the D_e associated with the light-sensitive TL traps is estimated by subtraction. Measurements were made on a Risø TL/OSL reader fitted with an Electron Tubes Ltd 9658B photomultiplier tube and Schott BG-39 and Kopp 2-63 filters designed to transmit red emissions (peak transmission in the 600–620 nm range, with minimum and maximum wavelengths of 580 and 670 nm), and cooled to -22°C to reduce the background count rate. Bleaching was performed using a halogen lamp and light guide integrated into the reader, and laboratory doses were given using a $^{90}\text{Sr}/^{90}\text{Y}$ source mounted on the reader. The quartz grains were first heated to 260°C at a heating rate of 5 K s^{-1} and then held at this temperature for 1000 s to induce an isothermal TL signal and reduce the unwanted glow from incandescence. Following ref. 22, D_e values were estimated from the 20–30 s interval of isothermal TL (which was shown to be light-sensitive) and the final 160 s was used as background. Two of the samples contained abundant quantities of quartz, so problems associated with inter-aliquot variability^{50,51} were reduced by measuring 12 replicates of each pair of aliquots (Supplementary Information section 2). As prolonged sunlight exposure is required to empty the light-sensitive TL traps, the ages obtained should be regarded as maximum estimates of the time elapsed since sediment deposition²².

Uranium-series ($^{234}\text{U}/^{230}\text{Th}$) dating of bones. Samples of bone from three specimens of *Homo floresiensis*, (LB1, LB2 and LB6), one *Homo sapiens* and eight *Stegodon florensis insularis* were analysed using laser ablation uranium-series isotope measurement analysis procedures and instruments similar to those described previously^{23,52}. Cuts were made perpendicular to the bone surface using a rotatory tool equipped with a thin (100 μm wide) diamond saw blade. The cut samples were mounted into aluminium cups, aligning the cross-sectioned surfaces with the outer rim of the sample holder to position the samples on the focal plane of the laser in the sampling cell. Sequential laser spot analyses were undertaken along 1–5 parallel tracks per sample, starting from the interior of each cross-sectioned bone (Extended Data Figs 8 and 9 and Supplementary Information section 3). Uranium and thorium isotopes were measured at the Australian National University using a Finnigan MAT Neptune multi-collector inductively-coupled plasma mass spectrometer (MC-ICP-MS) equipped with multiple Faraday cups and ion counters. Two ion counters were set to masses of 230.1 and 234.1, while the Faraday cups measured the masses 232, 235 and 238. Samples were ablated using a Lambda Physik LPFPro ArF excimer laser (193 nm) coupled to the MC-ICP-MS through a custom-designed Helex ablation cell. The analyses were made at regular spacing (typically 2–3 mm) along each track, using a laser spot size of 265 μm and a 5 Hz pulse rate. The samples were initially cleaned for 5 s and ablation pits were measured for 50 s. These measurements were bracketed by analyses of reference standards to correct for instrument drift. Semi-quantitative estimates of uranium and thorium concentrations were made from repeated measurements of the SRM NIST-610 glass standard (U: $461.5\text{ }\mu\text{g g}^{-1}$, Th: $457.2\text{ }\mu\text{g g}^{-1}$) and uranium-isotope (activity) ratios from repeated measurements of rhinoceros tooth dentine from Hexian sample 1118 (ref. 53). Apparent $^{234}\text{U}/^{230}\text{Th}$ ages were estimated for each track using a Diffusion–Adsorption–Decay (DAD) model²⁴, which uses the entire set of isotope measurements made along the track to calculate the rate of diffusion of ^{238}U and ^{234}U into the bone. Bones behave as geochemically ‘open’ systems, so the diffusion of uranium into a bone may have occurred soon after it was deposited or much later. The original isotopic signature may also be overprinted by secondary uranium uptake that is hard to recognise. As such, uranium-series ages for bones are most likely to be minimum estimates of time since deposition, with the extent of age underestimation being very difficult or impossible to evaluate²³. The modelled ages were calculated after rejecting data points associated with

detrital contamination (U/Th elemental ratios if ≤ 300) and data points at the surface of the bones where secondary overprinting was suspected. Results are tabulated in Supplementary Information section 3, with all errors given at 2σ .

Uranium-series ($^{234}\text{U}/^{230}\text{Th}$) dating of speleothems. Samples of calcite deposited as speleothems (flowstones and a 1 cm-tall stalagmite) were collected during excavation. Unlike bone, speleothems commonly behave as geochemically ‘closed’ systems, with no loss or gain of uranium after calcite crystallisation⁵⁴. The cleanest portion of each sample was selected, ground to the size of a rice grain, cleaned ultrasonically and then handpicked, avoiding pieces that appeared to be porous or contaminated. Age determinations were made at the University of Queensland using a Nu Plasma MC-ICP-MS. Uranium and thorium separation procedures, MC-ICP-MS analytical protocols, details of spike calibrations, blank and ‘memory’ assessments, and repeat measurements of standards have been described previously^{55,56}. The $^{234}\text{U}/^{230}\text{Th}$ ages were calculated using Isoplot 3.75 (ref. 57) and half-lives of 245.25 kyr (^{234}U) and 75.69 kyr (^{230}Th) (ref. 58). As most samples consist of impure calcite with some degree of detrital contamination, a correction for non-radiogenic ^{230}Th was applied to the measured $^{230}\text{Th}/^{232}\text{Th}$ activity ratio of each sample using an assumed bulk-Earth $^{230}\text{Th}/^{232}\text{Th}$ activity ratio of 0.825 (with a relative error of $\pm 50\%$ and assuming secular equilibrium in the ^{238}U – ^{234}U – ^{230}Th decay chain), as is typical of most other studies⁵⁹. This non-radiogenic ^{230}Th correction reduces the calculated ages of the samples and increases the age uncertainties by an amount dependent on the extent of detrital contamination. All ten dated samples have measured $^{230}\text{Th}/^{232}\text{Th}$ activity ratios of >20 (Supplementary Information section 4), so the detritally-corrected $^{234}\text{U}/^{230}\text{Th}$ ages are only slightly younger than the uncorrected (measured) ages.

Argon-argon ($^{40}\text{Ar}/^{39}\text{Ar}$) dating of hornblende crystals. Crystals of hornblende were obtained for the 100–150 and 150–250 μm size fractions of the T1 tephra using standard heavy liquid and magnetic separation techniques. Crystals were loaded into wells in 18 mm-diameter aluminium sample discs for neutron irradiation, along with the 1.185 million year-old Alder Creek sanidine²⁶ as the neutron fluence monitor. Neutron irradiation was carried out for 4 min in the cadmium-shielded CLICIT facility at the Oregon State University TRIGA reactor. Argon isotopic analyses of gas released from 6 hornblende aliquots during CO_2 laser step-heating, including a final fusion step (‘fuse’ in Supplementary Information section 5), were made on a fully automated, high-resolution, Nu Instruments Noblesse multi-collector noble-gas mass spectrometer, using procedures documented previously²⁵. One set of 4 experiments (Lab IDs 2598 and 2599 in Supplementary Information section 5) consisted of strong degassing of 10 mg hornblende aliquots in square pits in the laser disc, using a beam integrator lens that gives a ‘top hat’ 6 x 6 mm energy profile at the focal plane. The laser was then operated at 32 W and this high-temperature, pre-fusion step (‘D’ in Supplementary Information section 5) measured. The fusion step was performed using a conventional focus lens. In the second set of experiments, 20 mg hornblende aliquots were loaded into 5 mm-wide channels in the laser disc and a defocussed laser beam was programmed to raster in 50 traverses, each 30 mm in length and separated by 0.1 mm. Low power (< 1 W) steps were performed initially to remove loosely trapped argon. At 1 W of laser power (step ‘C’), the hornblende crystals began to glow and release significant amounts of ^{39}Ar . This and subsequent steps, including the final fusion, are reported in Supplementary Information section 5 as Lab IDs 2584-03C to -03O (fuse) and 2584-04C to -04I (fuse). Sample gas cleanup was through an all-metal extraction line, equipped with a -130°C cold trap (to remove H_2O) and two water-cooled SAES GP-50 getter pumps (to absorb reactive gases). Argon

isotopic analyses of unknowns, blanks and monitor minerals were carried out in identical fashion during a fixed period of 400 s in 14 data acquisition cycles. ^{40}Ar and ^{39}Ar were measured on the high-mass ion counter, ^{38}Ar and ^{37}Ar on the axial ion counter and ^{36}Ar on the low-mass ion counter, with baselines measured every third cycle. Measurement of the ^{40}Ar , ^{38}Ar and ^{36}Ar ion beams was carried out simultaneously, followed by sequential measurement of ^{39}Ar and ^{37}Ar . Beam switching was achieved by varying the field of the mass spectrometer magnet and with minor adjustment of the quad lenses. Data acquisition and reduction was performed using the program 'Mass Spec' (A. Deino, Berkeley Geochron. Center). Detector intercalibration and mass fractionation corrections were made using the weighted mean of a time series of measured atmospheric argon aliquots delivered from a calibrated air pipette²⁵. The accuracy of the primary air pipette measurements was verified by cross-referencing to data produced from a newly charged second air pipette. Decay and other constants, including correction factors for interference isotopes produced by nucleogenic reactions, are as reported in ref. 25. An isotope correlation (inverse isochron) plot of the data for all 28 aliquots is shown in Extended Data Fig. 3. The age determined from the inverse isochron is 85 ± 13 kyr for all 28 aliquots, or 79 ± 12 kyr (errors at 1σ) if the data point on the far right-hand side of the plot is excluded. In both cases, the $^{40}\text{Ar}/^{36}\text{Ar}$ intercept value is statistically indistinguishable from the atmospheric ratio of 298.6 ± 0.3 (ref. 60), indicating the absence of significant excess ^{40}Ar in the hornblende crystals.

Radiocarbon (^{14}C) dating of charcoal. Three charcoal samples recovered during excavation were sent to DirectAMS Radiocarbon Dating Service in Bothell, Washington (Supplementary Information section 6). Samples were pretreated using acid–base–acid (ABA) procedures and the ^{14}C content was measured using accelerator mass spectrometry⁶¹. Conventional ^{14}C ages in radiocarbon years before present (BP) were converted to calendar-year age ranges at the 68% and 95% confidence intervals using the SHCal13 calibration data set⁶² and CALIB 7.1 (<http://calib.qub.ac.uk/calib/>). One of these three samples yielded an 'old' radiocarbon age (>40 kyr BP), so we submitted the remaining charcoal to the Oxford Radiocarbon Accelerator Unit (ORAU) for a harsher cleaning protocol known as ABOx-SC^{63,64}. This pretreatment is known to improve charcoal decontamination and has been shown repeatedly to produce more reliable results for 'old' charcoal. However, the harshness of the ABOx-SC procedure often results in large material loss and sample failure, so a new preparative method (AOx-SC) has been developed and tested at the ORAU (Douka *et al.*, in preparation⁶⁵). The AOx-SC procedure does not include a NaOH step and produces identical results to ABOx-SC, but with much higher yields and reduced sample failure. For the Liang Bua sample, ~100 mg and ~50 mg of hand-picked charcoal underwent ABOx-SC and AOx-SC pretreatments, respectively. Only the AOx-treated charcoal survived the wet chemistry, yielding sufficient carbon for stepped combustion, first at 630 °C and then at 1000 °C, with the latter fraction collected for graphitisation and measurement by accelerator mass spectrometry.

References (cont'd)

31. Heinrich, K. F. J. in *Electron Probe Quantitation* (eds Heinrich K. F. J. & Newbury, D. E.), 9–18 (Plenum, 1991).
32. Jochum K. P. *et al.* MPI-DING reference glasses for in situ microanalysis: New reference values for element concentrations and isotope ratios. *Geochem. Geophys. Geosyst.* **7**, Q02008 (2006).

33. Alloway, B. V. *et al.* Correspondence between glass-FT and ^{14}C ages of silicic pyroclastic flow deposits sourced from Maninjau Caldera, west-central Sumatra. *Earth Planet. Sci. Lett.* **227**, 121–133 (2004).
34. Jacobs, Z. & Roberts, R. G. An improved single grain OSL chronology for the sedimentary deposits from Diepkloof Rockshelter, Western Cape, South Africa. *J. Archaeol. Sci.* **63**, 175–192 (2015).
35. Prescott, J. R. & Hutton, J. T. Cosmic ray contributions to dose rates for luminescence and ESR dating: large depths and long-term time variations. *Radiat. Meas.* **23**, 497–500 (1994).
36. Neudorf, C. M., Roberts, R. G. & Jacobs, Z. Sources of overdispersion in a K-rich feldspar sample from north-central India: insights from D_e , K content and IRSL age distributions for individual grains. *Radiat. Meas.* **47**, 696–702 (2012).
37. Neudorf, C. M. *Luminescence Investigations into the Time of Final Deposition of Toba Volcanic Ash and Artefact-bearing Alluvial Sediments in the Middle Son Valley, Madhya Pradesh, India*. PhD thesis, Univ. of Wollongong (2012).
38. Huntley, D. J. & Hancock, R. G. V. The Rb contents of the K-feldspars being measured in optical dating. *Anc. TL* **19**, 43–46 (2001).
39. Aitken, M. J. *An Introduction to Optical Dating* (Oxford Univ. Press, 1998).
40. Bøtter-Jensen, L., Andersen, C. E., Duller, G. A. T. & Murray, A. S. Developments in radiation, stimulation and observation facilities in luminescence measurements. *Radiat. Meas.* **37**, 535–541 (2003).
41. Roberts, R. G. *et al.* Optical dating in archaeology: thirty years in retrospect and grand challenges for the future. *J. Archaeol. Sci.* **56**, 41–60 (2015).
42. Li, B. & Li, S.-H. Luminescence dating of K-feldspar from sediments: a protocol without anomalous fading correction. *Quat. Geochronol.* **6**, 468–479 (2011).
43. Thiel, C. *et al.* Luminescence dating of the Stratzing loess profile (Austria) – testing the potential of an elevated temperature post-IR IRSL protocol. *Quat. Int.* **234**, 23–31 (2011).
44. Li, B., Roberts, R. G. & Jacobs, Z. On the dose dependency of the bleachable and non-bleachable components of IRSL from K-feldspar: improved procedures for luminescence dating of Quaternary sediments. *Quat. Geochronol.* **17**, 1–13 (2013).
45. Huntley, D. J., & Lamothe, M. Ubiquity of anomalous fading in K-feldspars and the measurement and correction for it in optical dating. *Can. J. Earth Sci.* **38**, 1093–1106 (2001).
46. Auclair, M., Lamothe, M. & Huot, S. Measurement of anomalous fading for feldspar IRSL using SAR. *Radiat. Meas.* **37**, 487–492 (2003).
47. Galbraith, R. F., Roberts, R. G., Laslett, G. M., Yoshida, H. & Olley, J. M. Optical dating of single and multiple grains of quartz from Jinmium rock shelter, northern Australia: Part 1, experimental design and statistical models. *Archaeometry* **41**, 339–364 (1999).
48. Galbraith, R. F. & Roberts, R. G. Statistical aspects of equivalent dose and error calculation and display in OSL dating: an overview and some recommendations. *Quat. Geochronol.* **11**, 1–27 (2012).
49. Franklin, A. D., Prescott, J. R. & Robertson, G. B. Comparison of blue and red TL from quartz. *Radiat. Meas.* **32**, 633–639 (2000).
50. Westaway, K. E. The red, white and blue of quartz luminescence: a comparison of D_e values derived for sediments from Australia and Indonesia using TL and OSL emissions. *Radiat. Meas.* **44**, 462–466 (2009).

51. Demeter, F. *et al.* Anatomically modern human in Southeast Asia (Laos) by 46 ka. *Proc. Natl Acad. Sci. USA* **109**, 14375–14380 (2012).
52. Eggins, S. M. *et al.* *In situ* U-series dating by laser-ablation multi-collector ICPMS: new prospects for Quaternary geochronology. *Quat. Sci. Rev.* **24**, 2523–2538 (2005).
53. Grün, R. *et al.* ESR and U-series analyses of teeth from the palaeoanthropological site of Hexian, Anhui Province, China. *J. Hum. Evol.* **34**, 555–564 (1998).
54. Hellstrom, J. & Pickering, R. Recent advances and future prospects of the U–Th and U–Pb chronometers applicable to archaeology. *J. Archaeol. Sci.* **56**, 32–40 (2015).
55. Zhou, H.-y., Zhao, J.-x., Wang, Q., Feng, Y.-x. & Tang, J. Speleothem-derived Asian summer monsoon variations in Central China, 54–46 ka. *J. Quat. Sci.* **26**, 781–790 (2011).
56. Clark, T. R. *et al.* Discerning the timing and cause of historical mortality events in modern *Porites* from the Great Barrier Reef. *Geochim. Cosmochim. Acta* **138**, 57–80 (2014).
57. Ludwig, K. R. *User's Manual for Isoplot 3.75: a Geochronological Toolkit for Microsoft Excel* (Berkeley Geochron. Center, 2012).
58. Cheng, H. *et al.* The half-lives of uranium-234 and thorium-230. *Chem. Geol.* **169**, 17–33 (2000).
59. Zhao, J.-x., Yu, K.-f. & Feng, Y.-x. High-precision ^{238}U – ^{234}U – ^{230}Th disequilibrium dating of the recent past: a review. *Quat. Geochronol.* **4**, 423–433 (2009).
60. Lee, J.-Y. *et al.* A redetermination of the isotopic abundances of atmospheric Ar. *Geochim. Cosmochim. Acta* **70**, 4507–4512 (2006).
61. Wood, R. From revolution to convention: the past, present and future of radiocarbon dating. *J. Archaeol. Sci.* **56**, 61–72 (2015).
62. Hogg, A. G. *et al.* SHCal13 Southern Hemisphere calibration, 0–50,000 years cal BP. *Radiocarbon* **55**, 1889–1903 (2013).
63. Bird, M. I. *et al.* Radiocarbon dating of “old” charcoal using a wet oxidation, stepped-combustion procedure. *Radiocarbon* **41**, 127–140 (1999).
64. Brock, F., Higham, T. F. G., Ditchfield, P. & Bronk Ramsey, C. Current pretreatment methods for AMS radiocarbon dating at the Oxford Radiocarbon Accelerator Unit (ORAU). *Radiocarbon* **52**, 103–112 (2010).
65. Douka, K. *et al.* An improved methodology (AOx-SC) for the reliable radiocarbon dating of old charcoal (in preparation).

Extended Data items

Extended Data Figure 1 | Stratigraphy of the excavated area near the eastern cave wall at eight stages of depositional history, with approximate ages indicated. Each panel (a–h) shows the remnant deposits exposed in the 2 m-wide baulks of the following Sectors (from left to right): north VII, east VII, XI and XXIII, south XXIII and XXI, west XXI, XV and XVI, and north XVI. The pedestal deposits shown in b–d were truncated by one or more phases of erosion that resulted in an erosional surface (i.e., an unconformity) that slopes steeply down towards the cave mouth (see also Supplementary video 1). The black arrows relate to the accompanying text in each panel. The maximum depth excavated was 10.75 m in Sector VII (e.g., the left two panels in h).

Extended Data Figure 2 | Deposits containing the remains of *Homo floresiensis*. These deposits (A) consist of multiple layers of fine-grained sediment interspersed with layers of weathered limestone and loose gravel, and are directly overlain by two tephras (T1 and T2). a,

South baulk of Sector XV, near the eastern cave wall. **b**, West baulk of Sector XV, also showing the unconformably overlying deposits (**B**). **c** and **d**, North and east baulks of Sector XIX, near the cave centre.

Extended Data Figure 3 | The volcanoclastic deposits at Liang Bua. **a**, Photograph of tephra T6–T8 (north baulk of Sector XVI). **b**, Photograph of tephra T1–T5 (south baulk of Sector XXI). **c**, Bivariate plot of FeO and CaO concentrations (expressed as weight %), acquired by electron microprobe analysis of glass shards from T1 ($n = 6$), T3 ($n = 4$), T5 ($n = 10$) and T7 ($n = 15$), as well as the Youngest Toba Tuff (YTT, $n = 207$, $\pm 1\sigma$) from northern Sumatra. **d**, Bivariate plot of FeO and K₂O concentrations (symbols as in **c**). **e**, Bivariate plot of SiO₂ and Na₂O + K₂O concentrations (symbols as in **c**). **f**, Isotope correlation (inverse isochron) plot for hornblende crystals from T1. The error ellipses represent individual analyses ($n = 28$). The ellipse on the far right-hand side was omitted from the $^{40}\text{Ar}/^{39}\text{Ar}$ age determination of 79 ± 12 kyr (at 1σ).

Extended Data Figure 4 | Erosional surface of the pedestal in the west baulks of Sectors XV and XVI. The dashed line marks the steeply sloping boundary between remnant deposits (**T2**, **T1** and the underlying *Homo floresiensis*-bearing sediments) that comprise part of the pedestal (**A**) and the much younger deposits (**B**) that unconformably overlie the contact. **a**, Photograph taken at an upward angle showing the sedimentary differences between the deposits above and below the erosional boundary. **b**, Illustration of the erosional surface and underlying deposits shown in **a**.

Extended Data Figure 5 | Erosional surface of the pedestal near the eastern wall of the cave. **a**, Illustration of the erosional surface and the locations of LB1, LB4, LB6 and LB8 below the boundary (see also Fig. 3). The deposits that unconformably overlie the pedestal are shown in the south and west baulks. The stippled cube outlines the photographed area (in Sector XV) shown in **b** and **c**. Both photographs taken from above, with north towards the bottom of the page.

Extended Data Figure 6 | Locations of sediment samples dated in this study and TL data for quartz grains from Liang Bua. **a**, Stratigraphy of the excavated area near the eastern cave wall (Sector baulks as in Extended Data Fig. 1) with TL samples indicated by red circles, IRSL samples by blue circles and the $^{40}\text{Ar}/^{39}\text{Ar}$ sample by a yellow square. Also shown are the TL and IRSL sample codes and the locations of hominin remains LB1 and LB6. **b**, Representative isothermal (260 °C) TL decay curves for the natural (black line) and test dose (grey line) signals from sample LB08-15-3. **c** and **d**, Regenerated TL dose-response curves for one pair of Aliquots A and B of sample LB08-15-3, respectively; the equivalent dose (D_e) is estimated by projecting the natural signal (red square) on to the dose-response curve fitted to the regenerated signals (blue diamonds). **e**, Radial plot^{47,48} of D_e values for Aliquot A ($n = 12$) of sample LB08-15-3; the grey band is centered on the weighted mean D_e calculated using the central age model. **f**, Radial plot of the corresponding D_e values for Aliquot B ($n = 12$) of the same sample. The grey band is centered on the central age model estimate, with the two high- D_e outliers omitted. The red line intersects the right-hand axis at the D_e calculated by fitting the minimum age model^{47,48} to all 12 values. **g** and **h**, Radial plots of D_e values for Aliquots A and B of sample LB12-23-1 (symbols as in **e** and **f**).

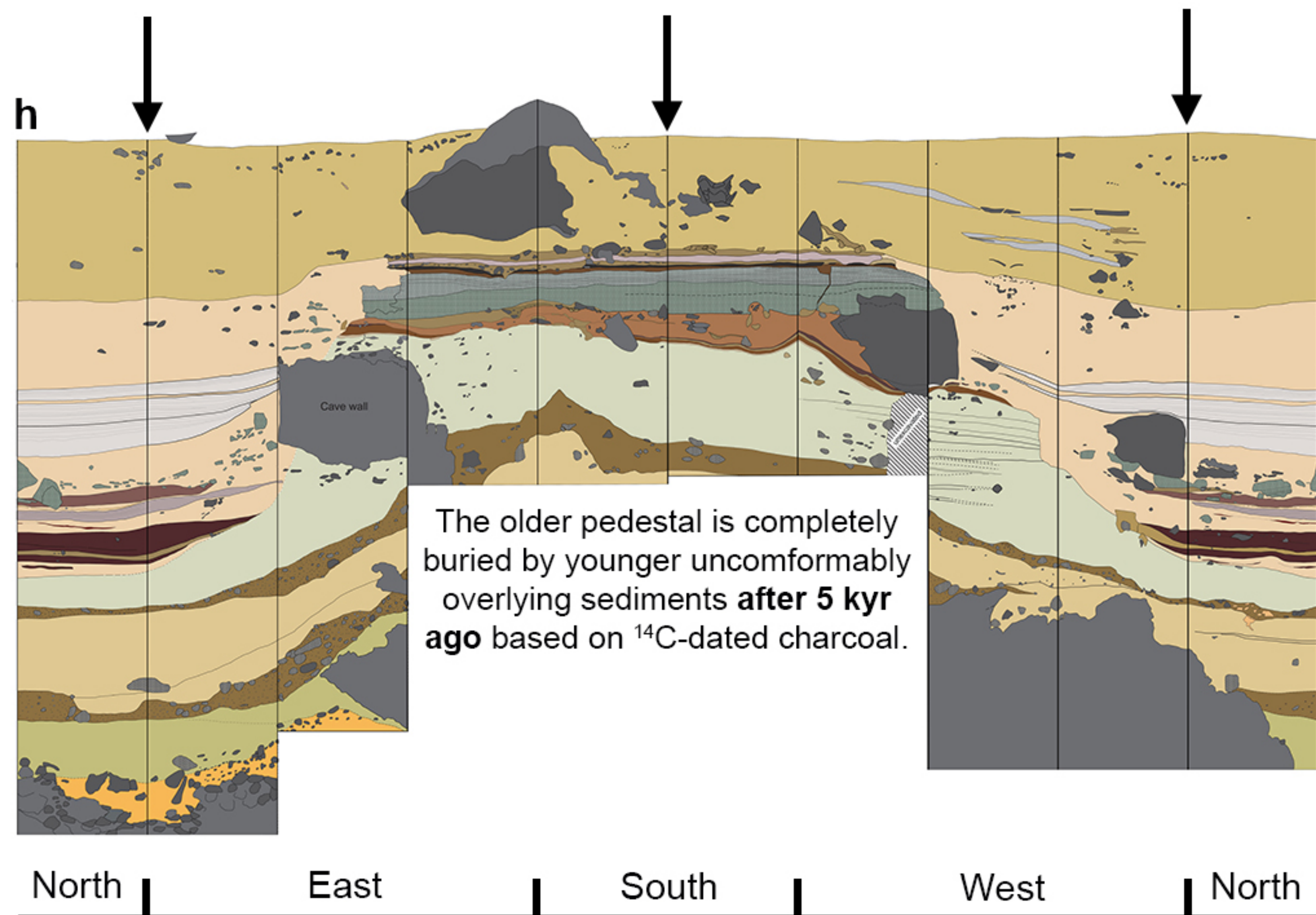
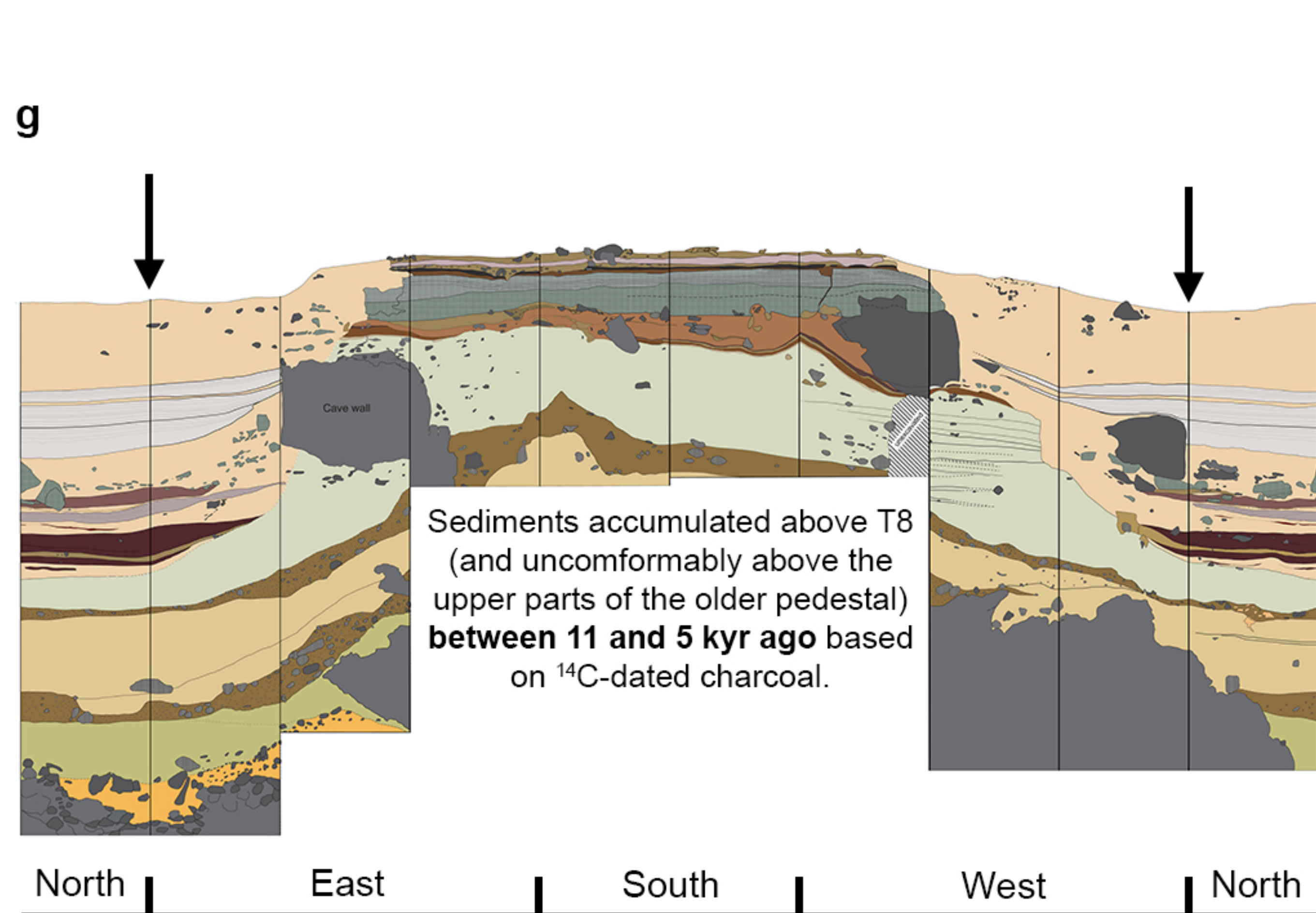
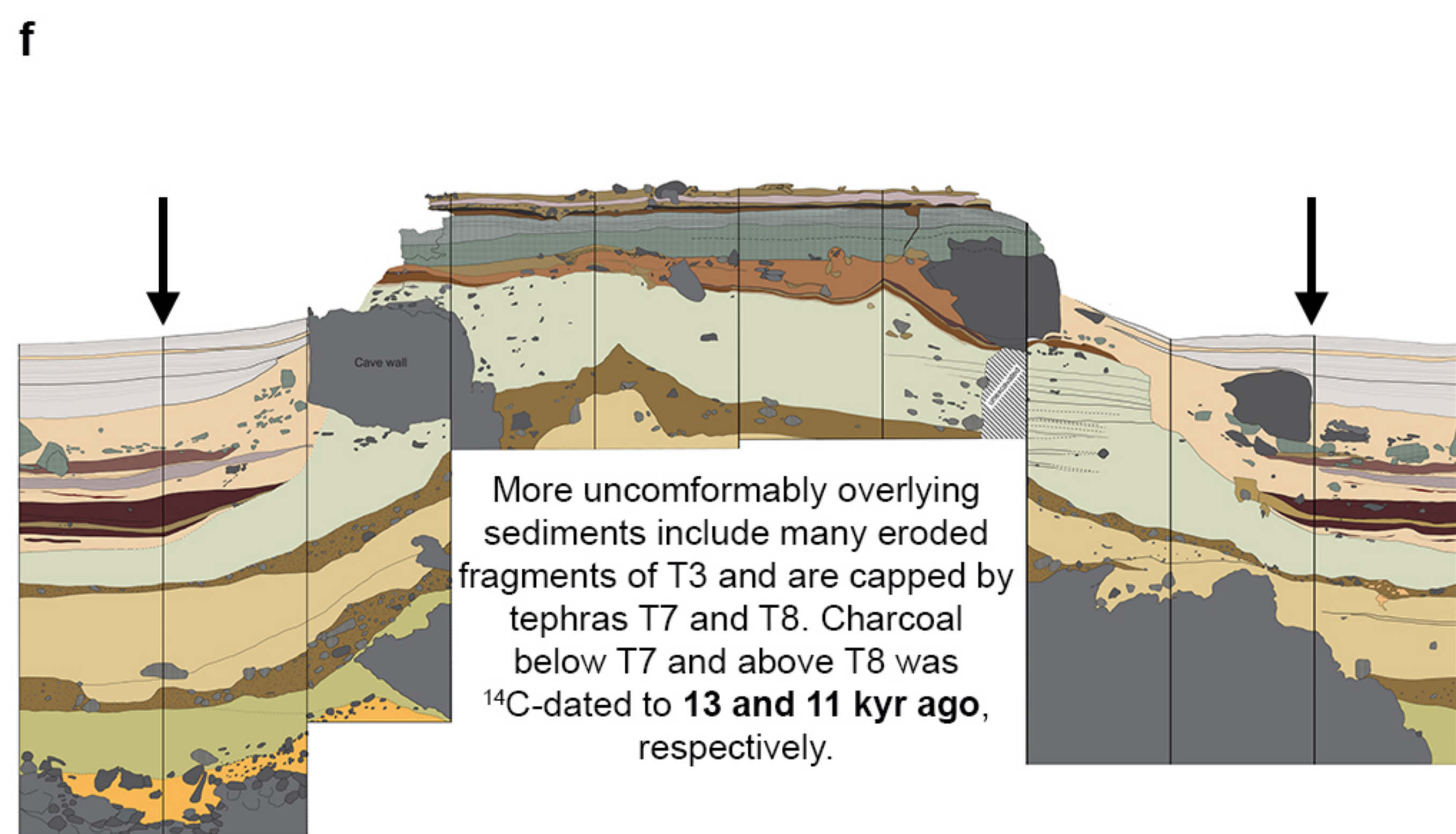
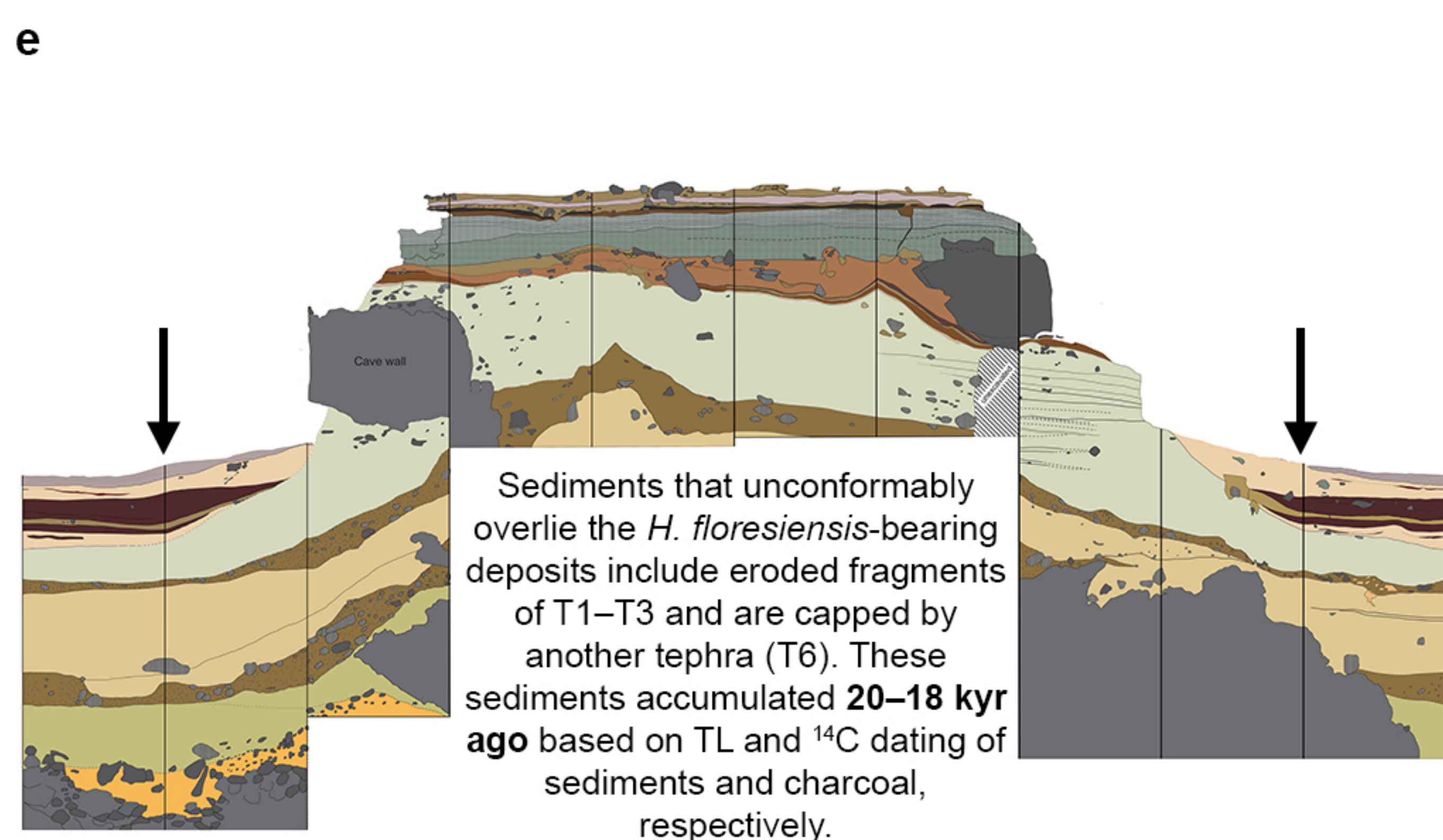
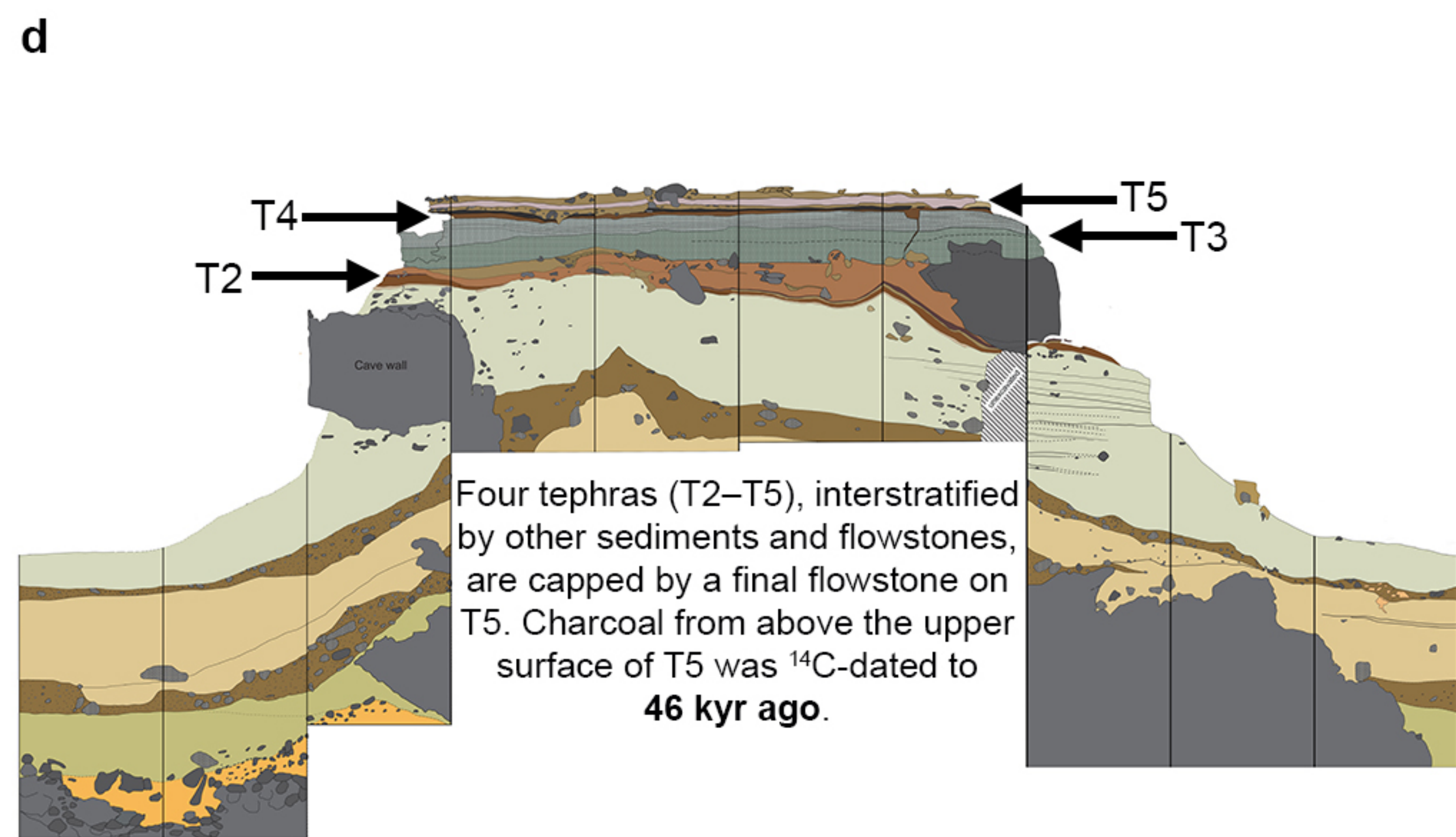
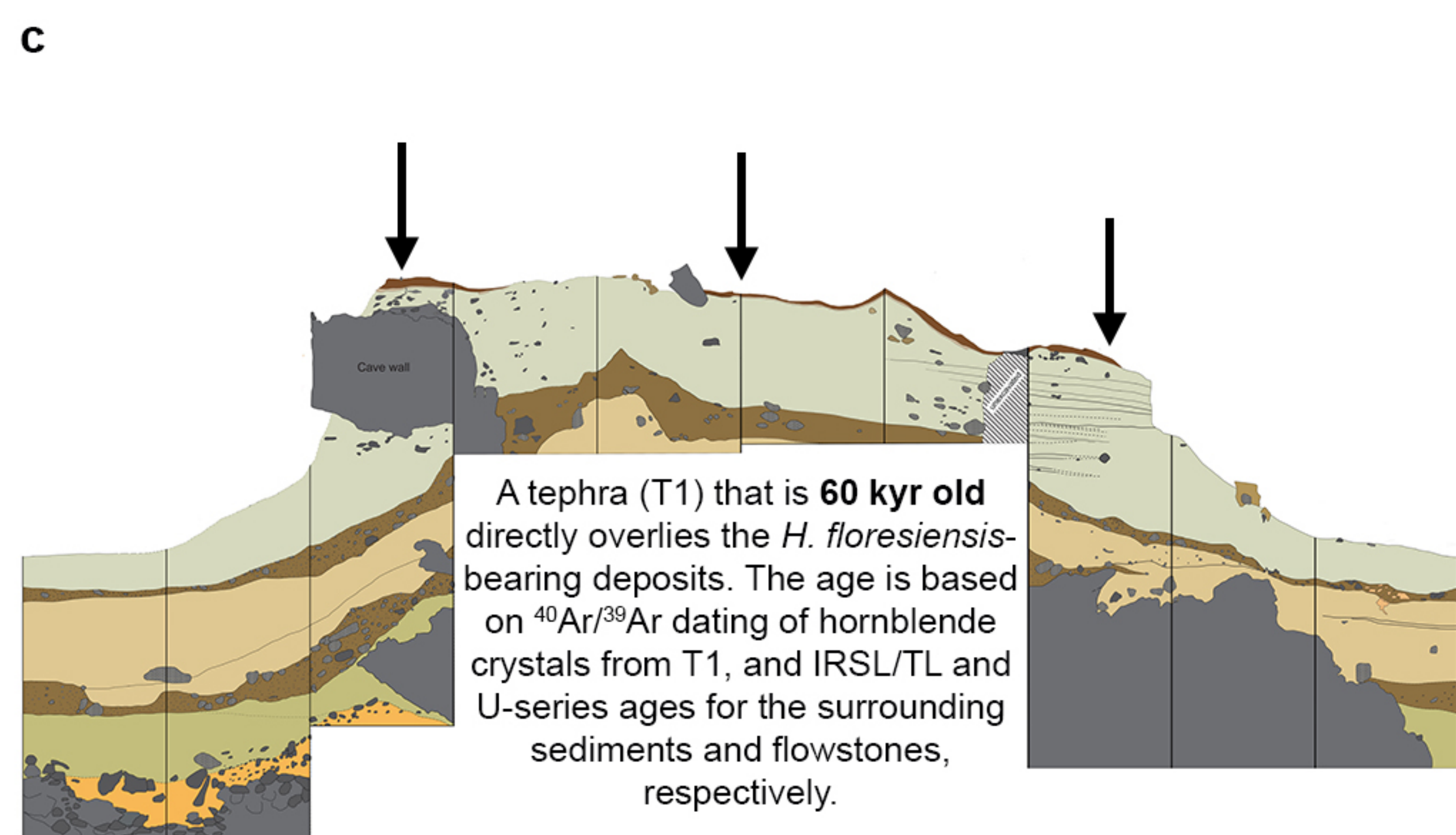
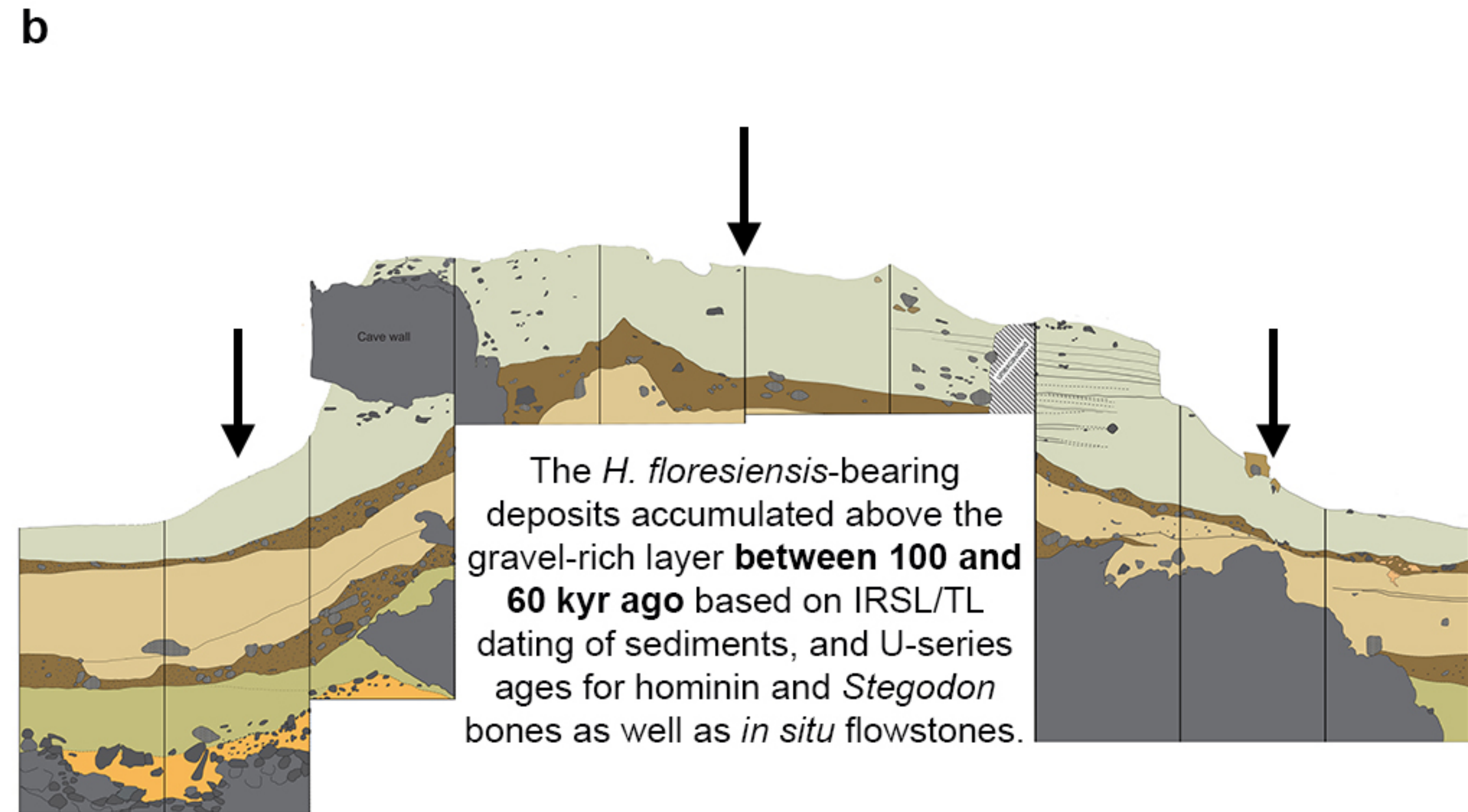
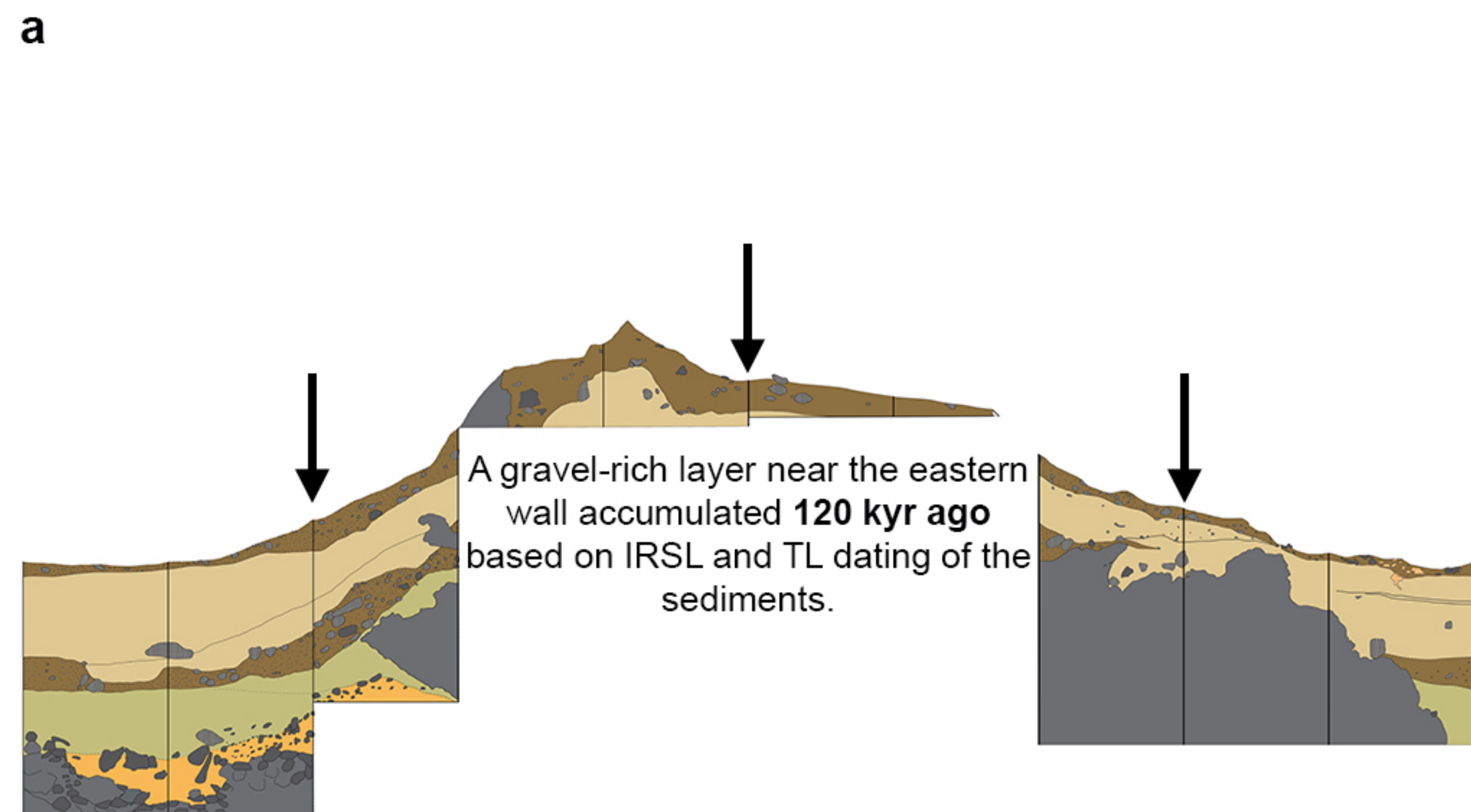
Extended Data Figure 7 | IRSL data and potassium (K) concentrations for feldspar grains from Liang Bua. **a**, Representative IRSL (50 °C) and multiple elevated temperature (100–250 °C) post-infrared IRSL (pIRIR) decay curves for a single aliquot of sample LB12-OSL1. **b**, IRSL (50 °C) and pIRIR (290 °C) decay curves for a different aliquot of LB12-OSL1. **c**, Regenerated pIRIR (290 °C) dose-response curve for the aliquot shown in **b**; the equivalent dose (D_e) is estimated by projecting the natural signal (red square) on to the dose-response curve fitted to the regenerated signals (blue diamonds). **d–j**, Radial plots of IRSL ages (corrected for residual dose and anomalous fading) for single aliquots of each sample: **d**, LB12-OSL1; **e**, LB12-OSL2; **f**, LB12-OSL3; **g**, LB12-OSL4; **h**, LB12-OSL5; **i**, LB12-OSL6; and **j**, LB12-OSL7. IRSL ages were also obtained for single grains of samples LB12-OSL3 and LB12-OSL4, and are shown as open triangles in plots **f** and **g**. The grey bands in each plot are centered on the weighted mean ages calculated using the central age model. **k** and **l**, Radial plots of IRSL ages (corrected as for **d–j**) for samples LBS7-40a and LBS7-42a, respectively; single aliquots are shown as filled circles and single grains as open triangles. The upper and lower red lines intersect the right-hand axis at the maximum and minimum single-grain ages, respectively. **m**, Distribution of pIRIR intensities from 28 individual grains of feldspar from sample LB12-OSL3 that had been given a regenerative dose of 80 Gy. The relative contribution of each grain to the total (cumulative) pIRIR light sum is plotted as a function of K concentration (measured by wavelength-dispersive X-ray spectroscopy); note the reversed scale on the x -axis. **n**, Cumulative pIRIR light sum for the same 28 grains as shown in **m**, plotted as a function of grains ranked by K concentration (which decreases from left to right).

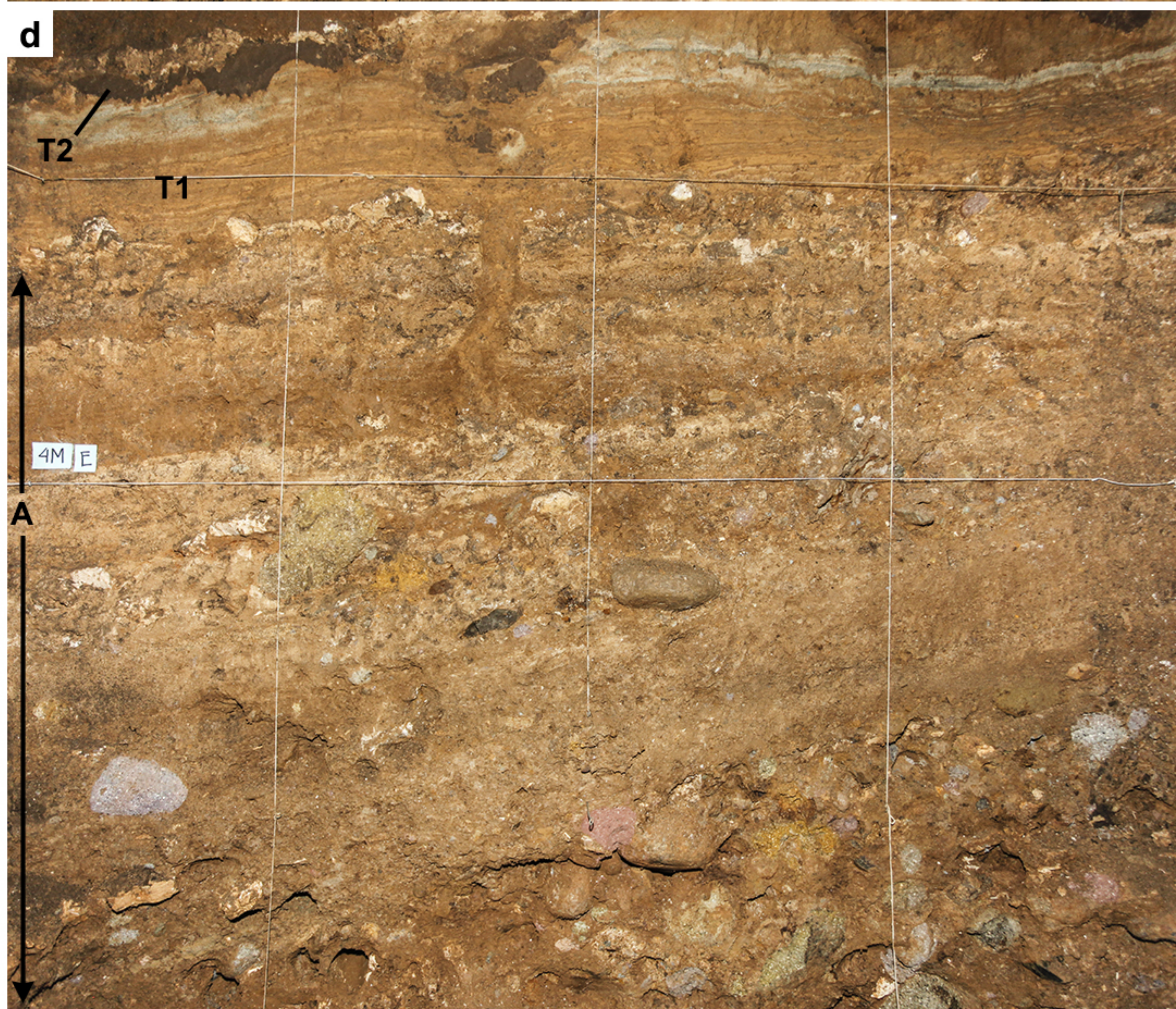
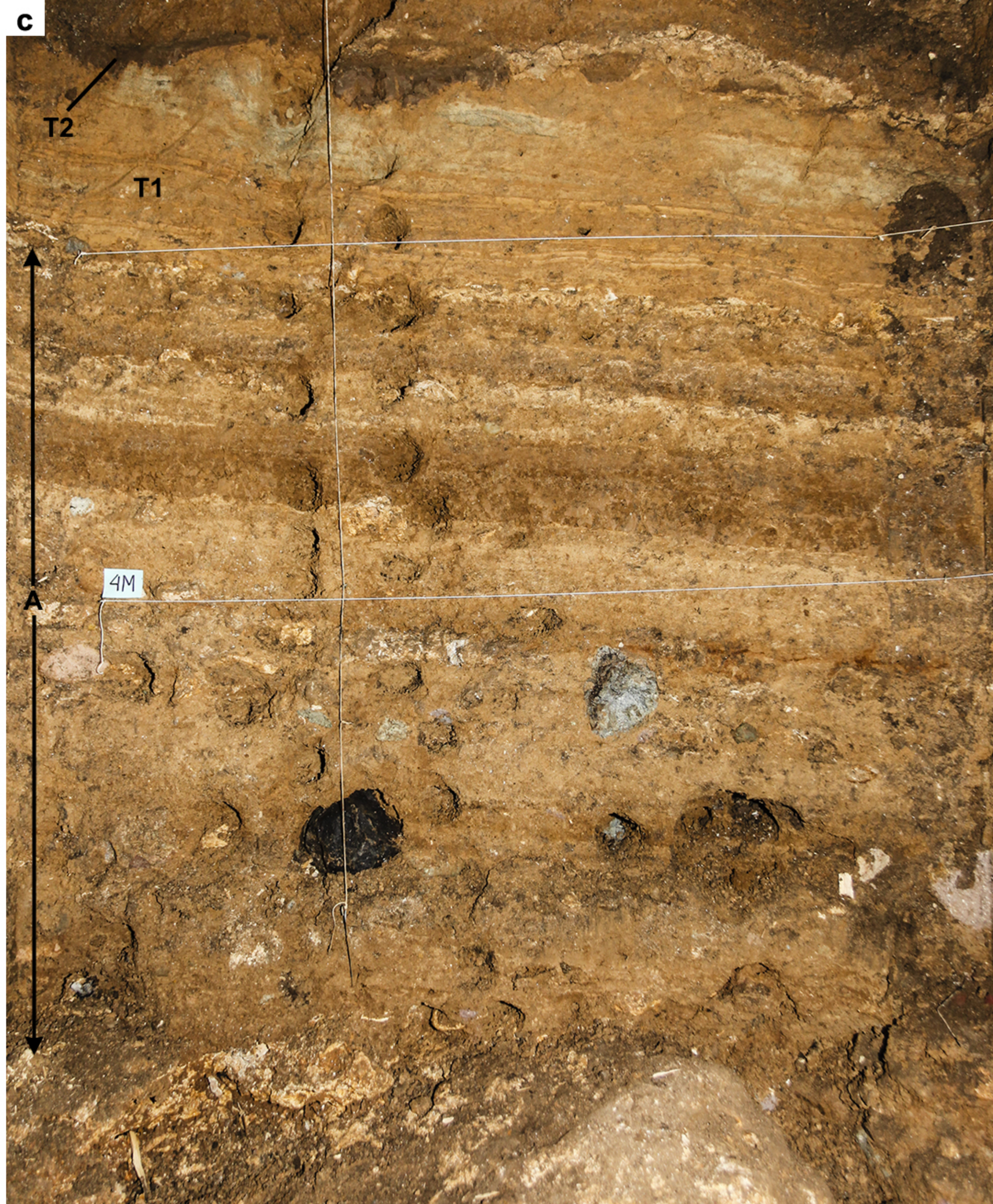
Extended Data Figure 8 | Laser-ablation uranium-series analyses of hominin bone fragments from various Sectors and spits (depth intervals), and their modelled ages. **a**, Modern human femur (132A/LB/27D/03) from Sector IV, Spit 27 (265–275 cm). **b**, *Homo floresiensis* ulna (LB1/52) from Sector XI, Spit 58A (575–585 cm). **c**, *H. floresiensis* ulna (LB2/1) from Sector IV, Spit 42D (415–425 cm). **d**, *H. floresiensis* ulna (LB6/3) from Sector XI, Spit 51 (505–515 cm). Each laser spot is 265 μ m in diameter and the age errors are at 2σ .

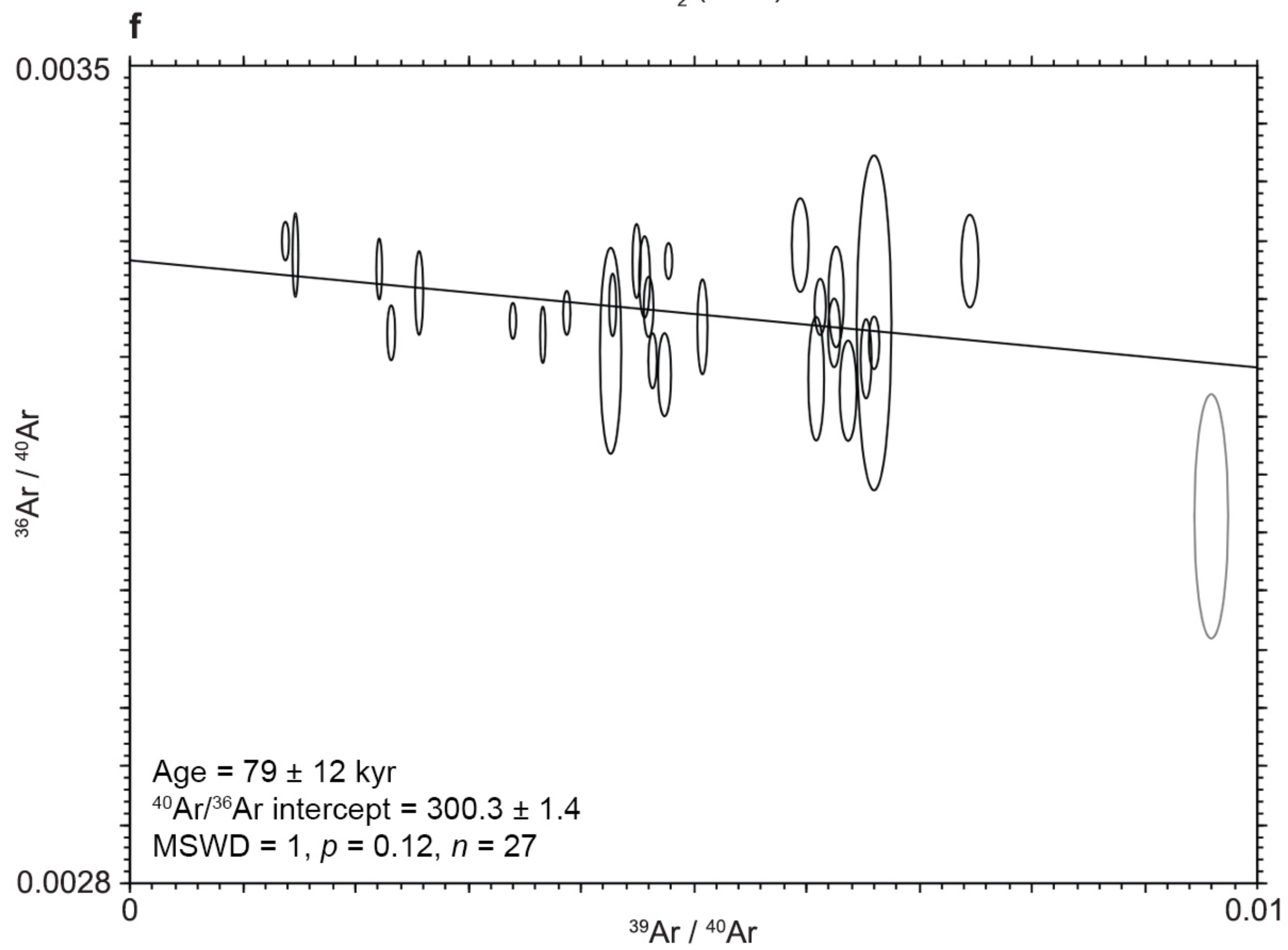
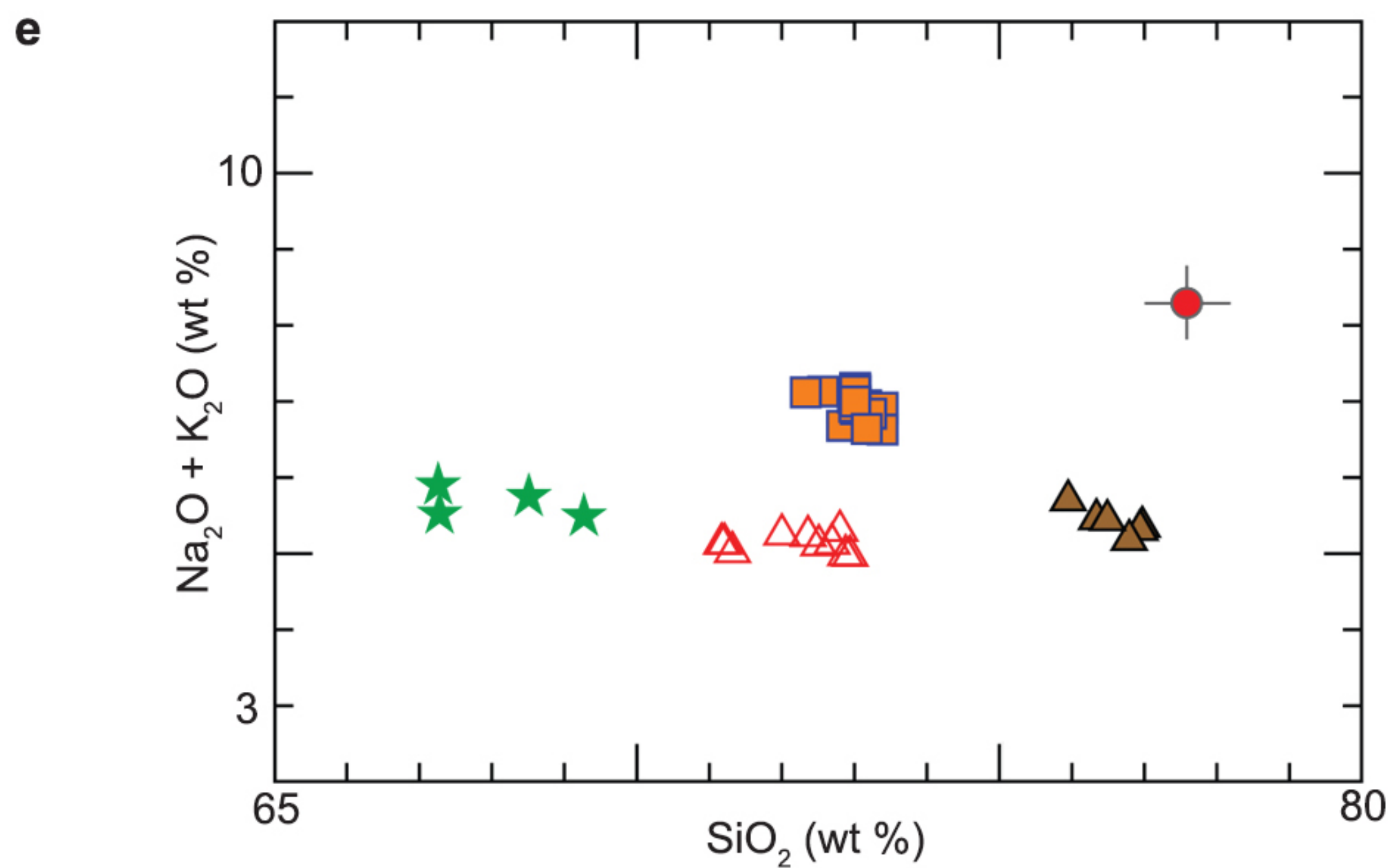
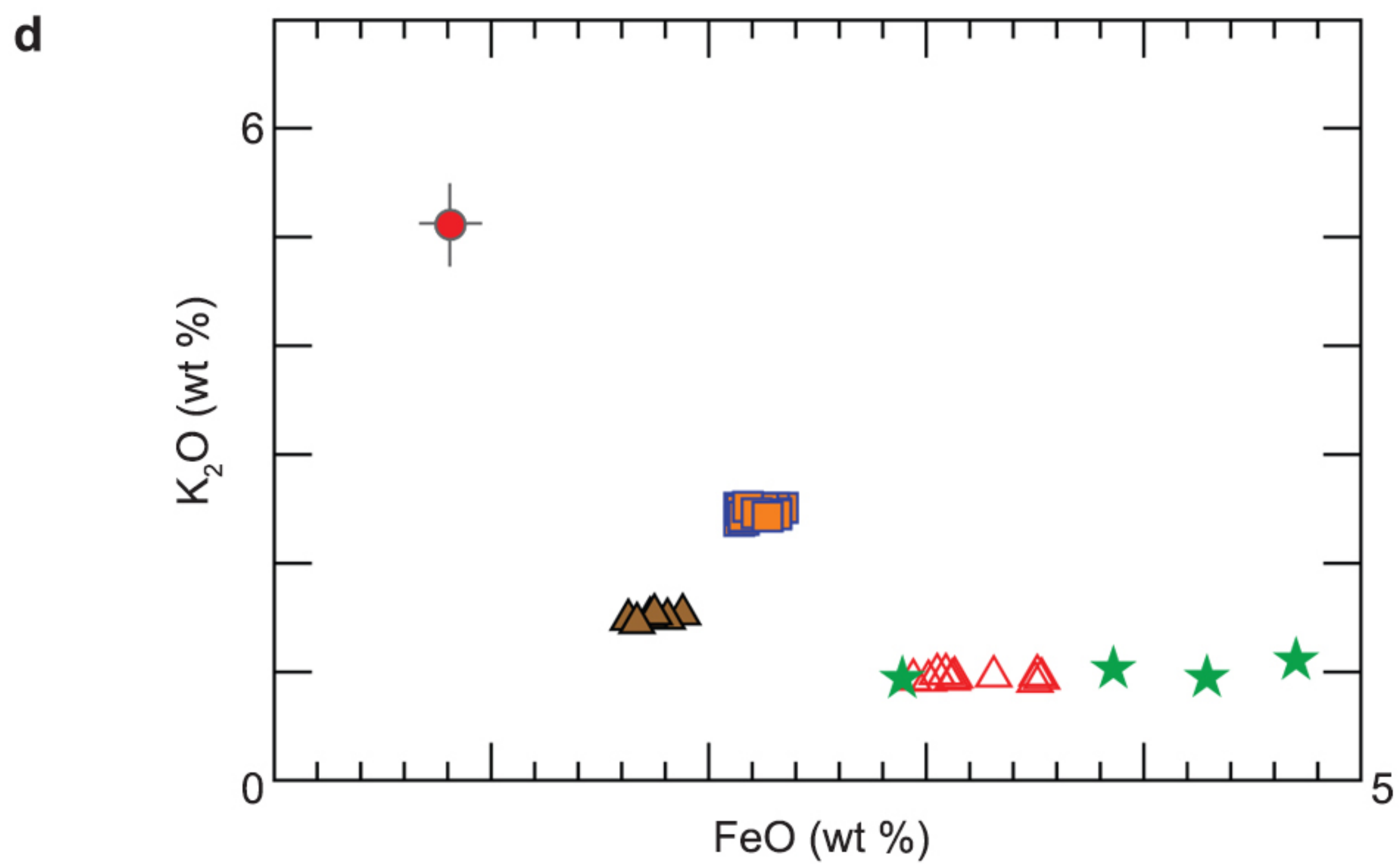
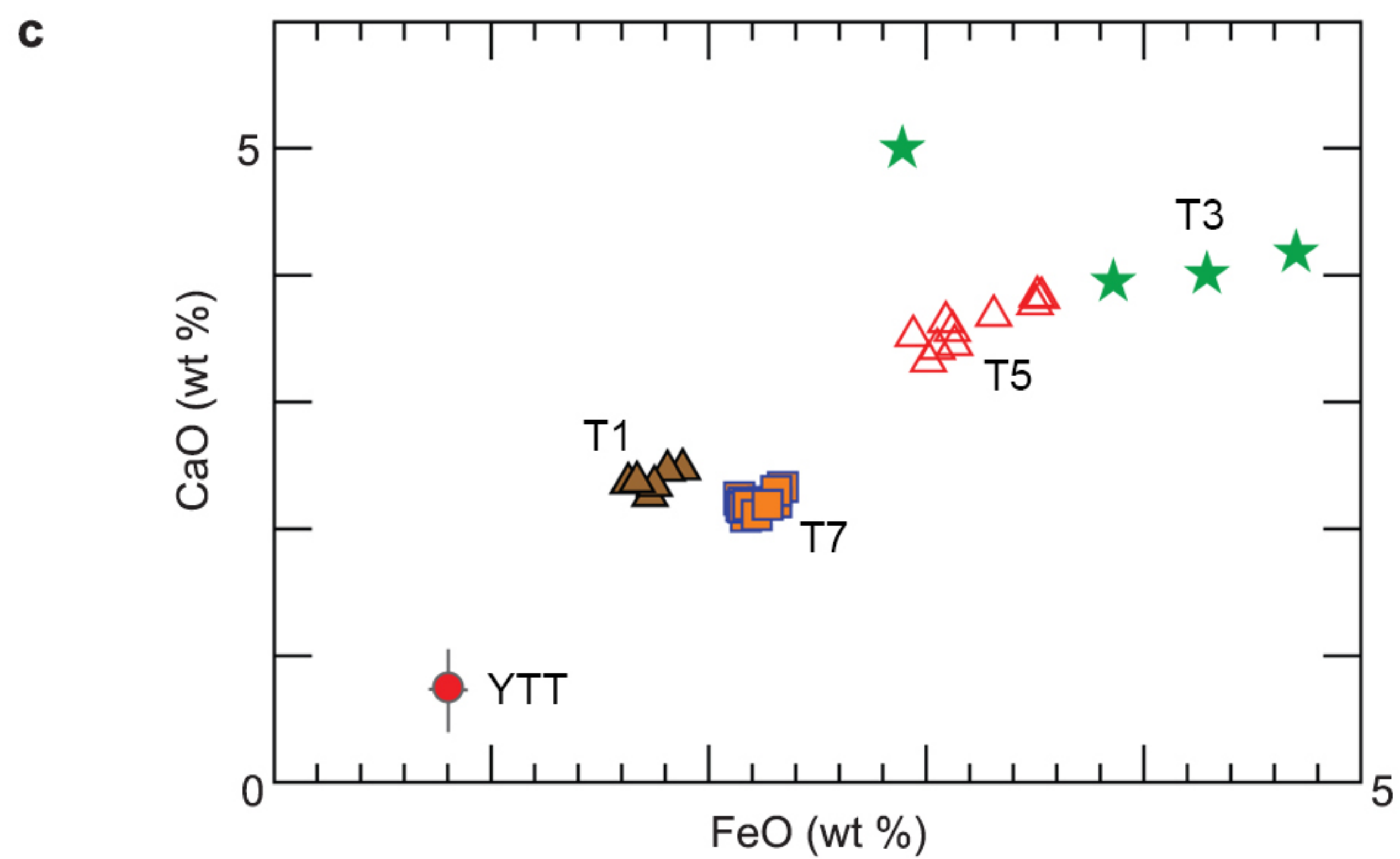
Extended Data Figure 9 | Laser-ablation uranium-series analyses of bone fragments of *Stegodon florensis insularis* from various spits (depth intervals) in Sector XI, and their modelled ages. **a**, U-s-01/LB/XI/32/04, Spit 32 (315–325 cm). **b**, U-s-02/LB/XI/45/04, Spit 45 (445–455 cm). **c**, U-s-03/LB/XI/47/04, Spit 47 (465–475 cm). **d**, U-s-04/LB/XI/49/04, Spit 49 (485–495 cm). **e**, U-s-05/LB/XI/51/04, Spit 51 (505–515 cm). **f**, U-s-06/LB/XI/52/04, Spit 52 (515–525 cm). **g**, U-s-07/LB/XI/65/04, Spit 65 (645–655 cm). **h**, U-s-08/LB/XI/65B/04, Spit 65B (645–655 cm). Each laser spot is 265 μ m in diameter and the age errors are at 2σ .

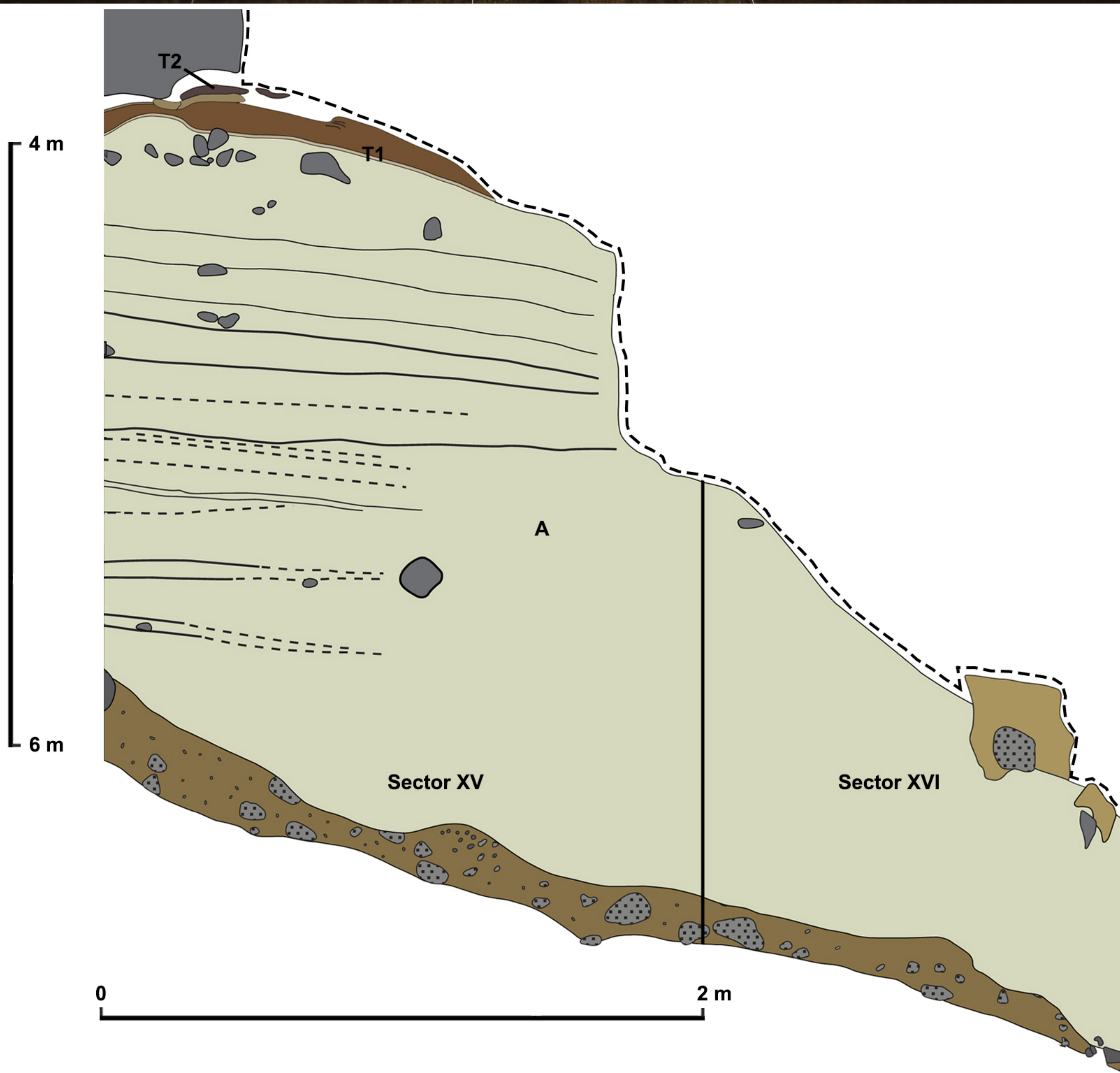
Extended Data Figure 10 | Deposits stratigraphically above the unconformity in Sector XVI and displaced slab of deposit in Sector XXII. **a**, The north baulk (~2 m wide) of Sector XVI. **b**, Excavated floors (white arrow points north) of spits 61–63 (615–635 cm depth); the field of view is ~1.6 m in width. The stippled box in **a** indicates the floor of spit 63 in **b**, where fragments of T1 (+) are visible in spit 63, and fragments of T3 (*) and T1 are concentrated in the band just above the label for spit 61. Eroded fragments (between about 1 cm and 60 cm in size) of T1, T2 and T3 have been consistently recovered from deposits unconformably overlying the erosional surface of the pedestal, indicating reworking of the pedestal deposits before ~13 kyr cal. BP. **c**, Photograph of the west baulk and parts of the south and north baulks (at left and right,

respectively) of Sector XXII showing a displaced slab of deposit that contains intact portions of the uppermost part of T3 (arrow) and the overlying layers, up to and including the flowstone (fs) that caps T5. The stratigraphic position of the slab beneath T7 and T8 indicates that it broke away from its original location, slightly to the south, and slid down the steeply sloping erosional surface prior to ~13 kyr cal. BP. Also shown are the *Homo floresiensis*-bearing deposits (**A**) and the unconformably overlying deposits (**B**), which include eroded fragments of T1 (+), T2 (#) and T3 (*). **d**, Illustration of the west baulk of Sector XXII, as shown in **c**.



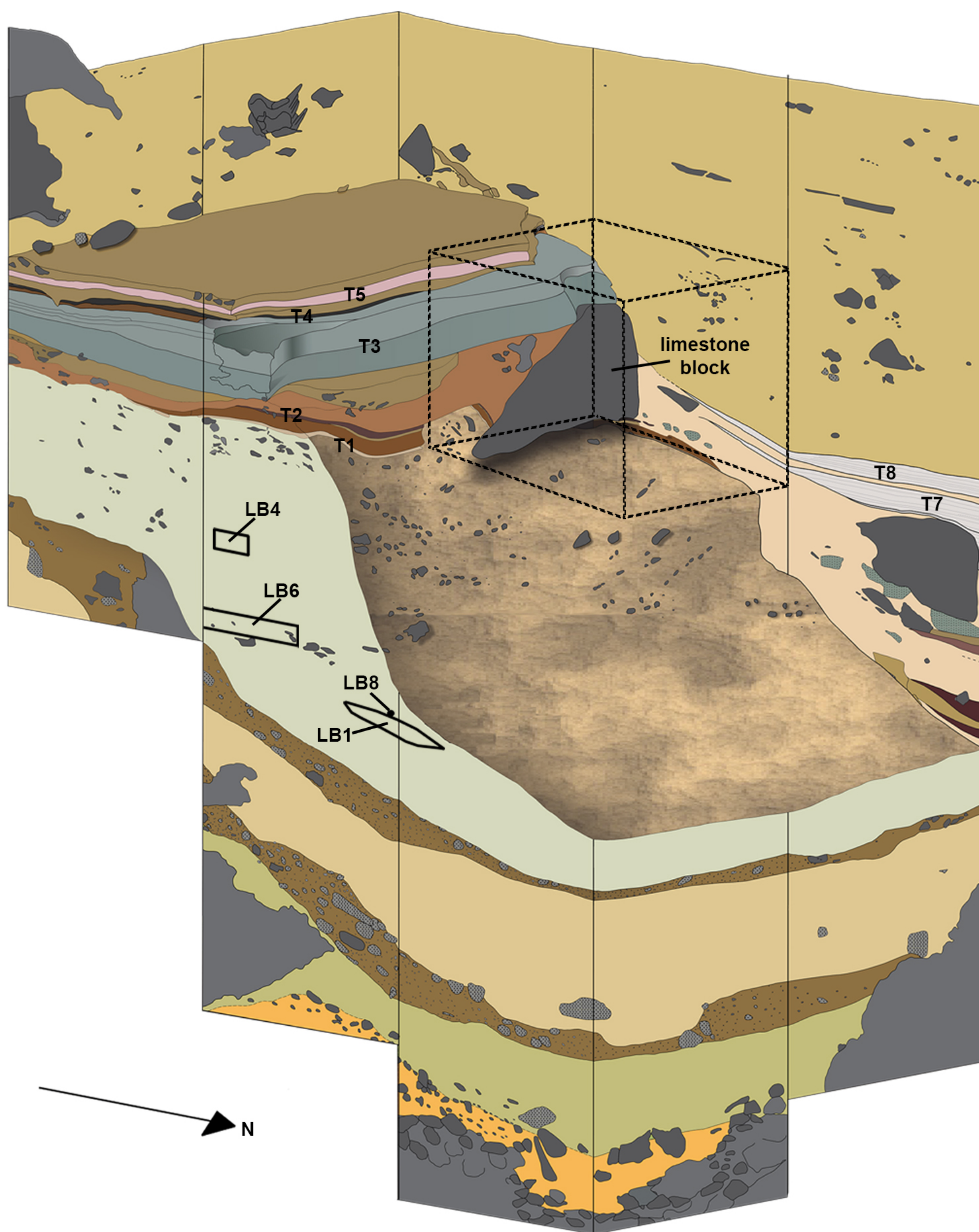




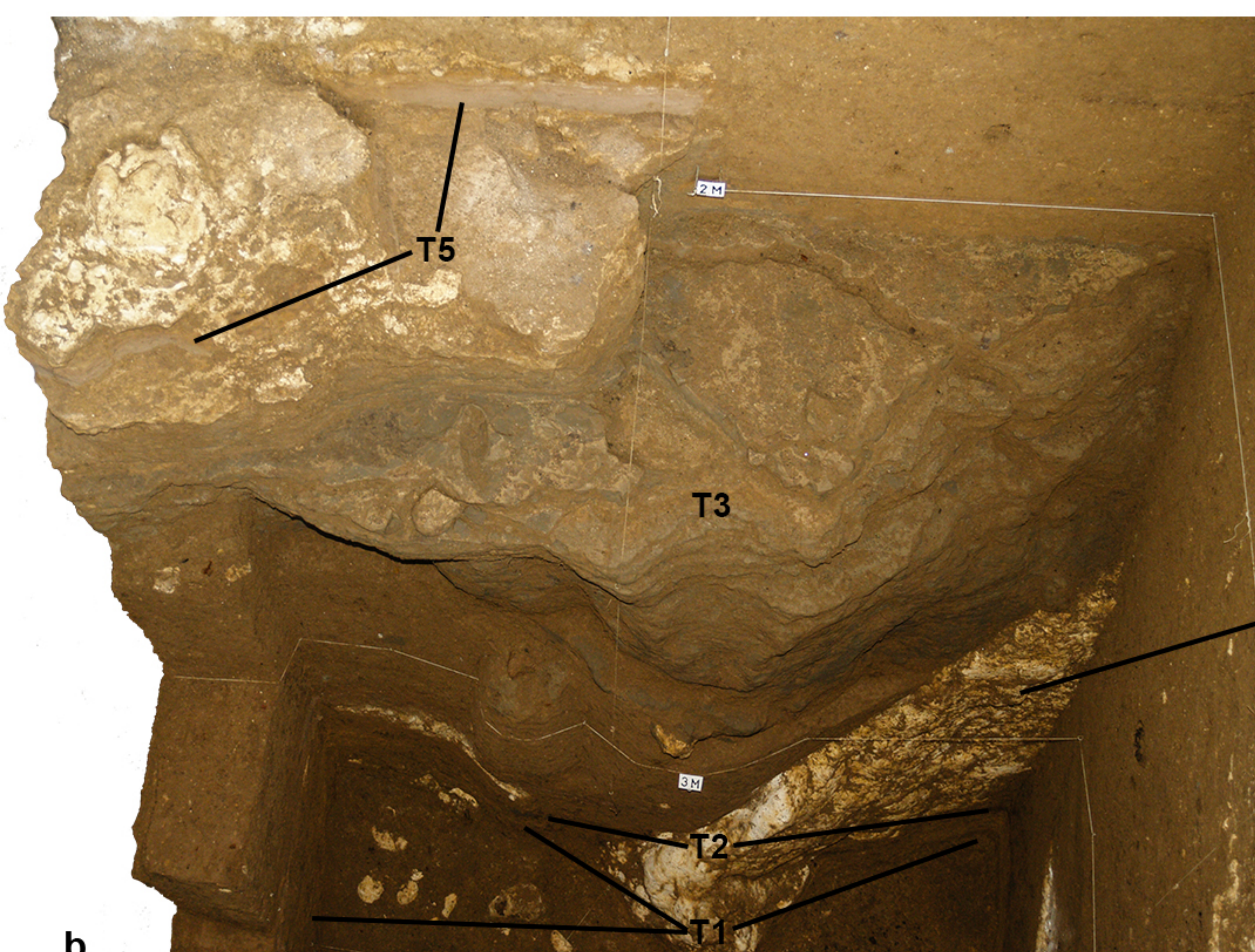


0 m

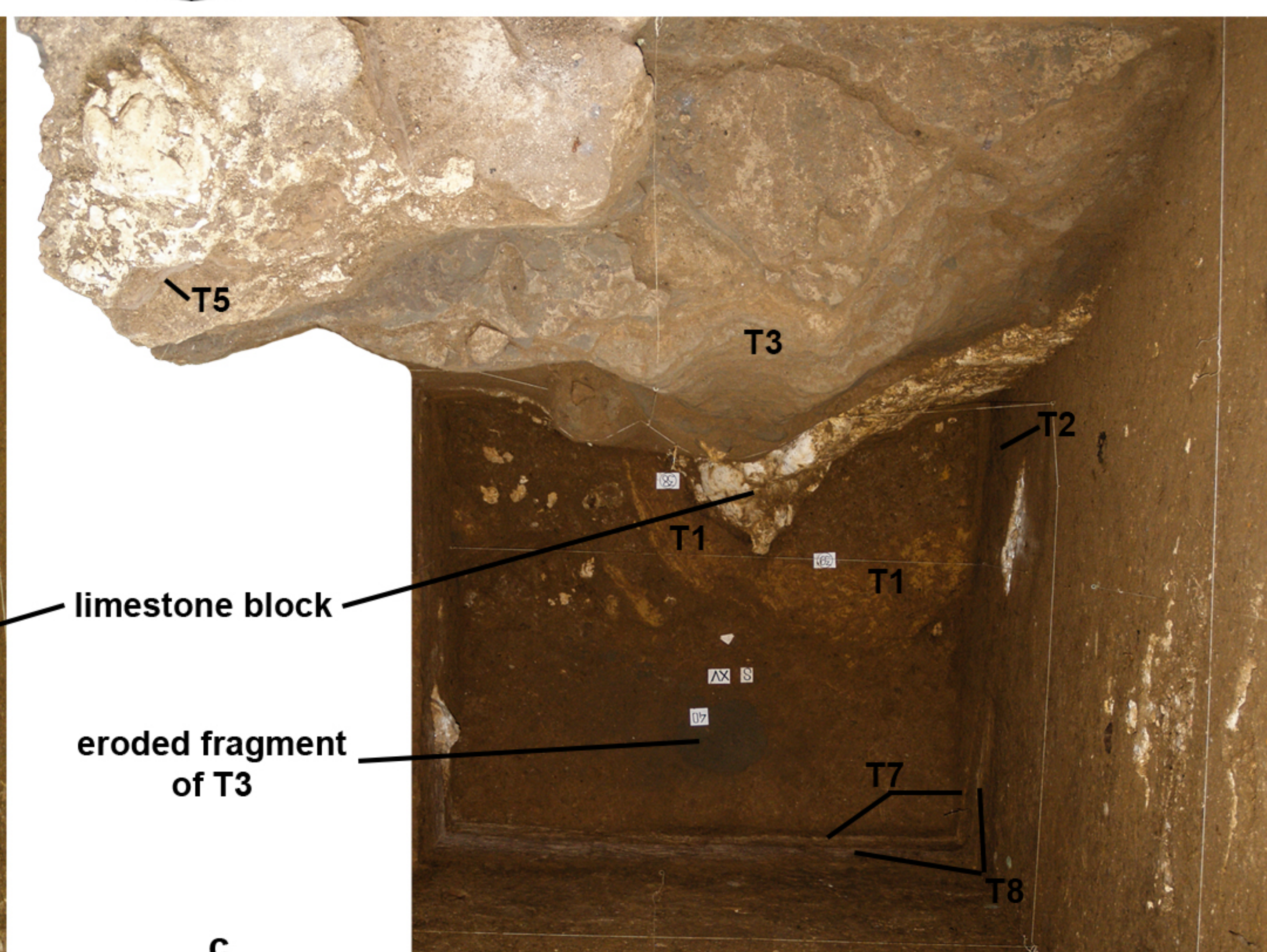
10 m



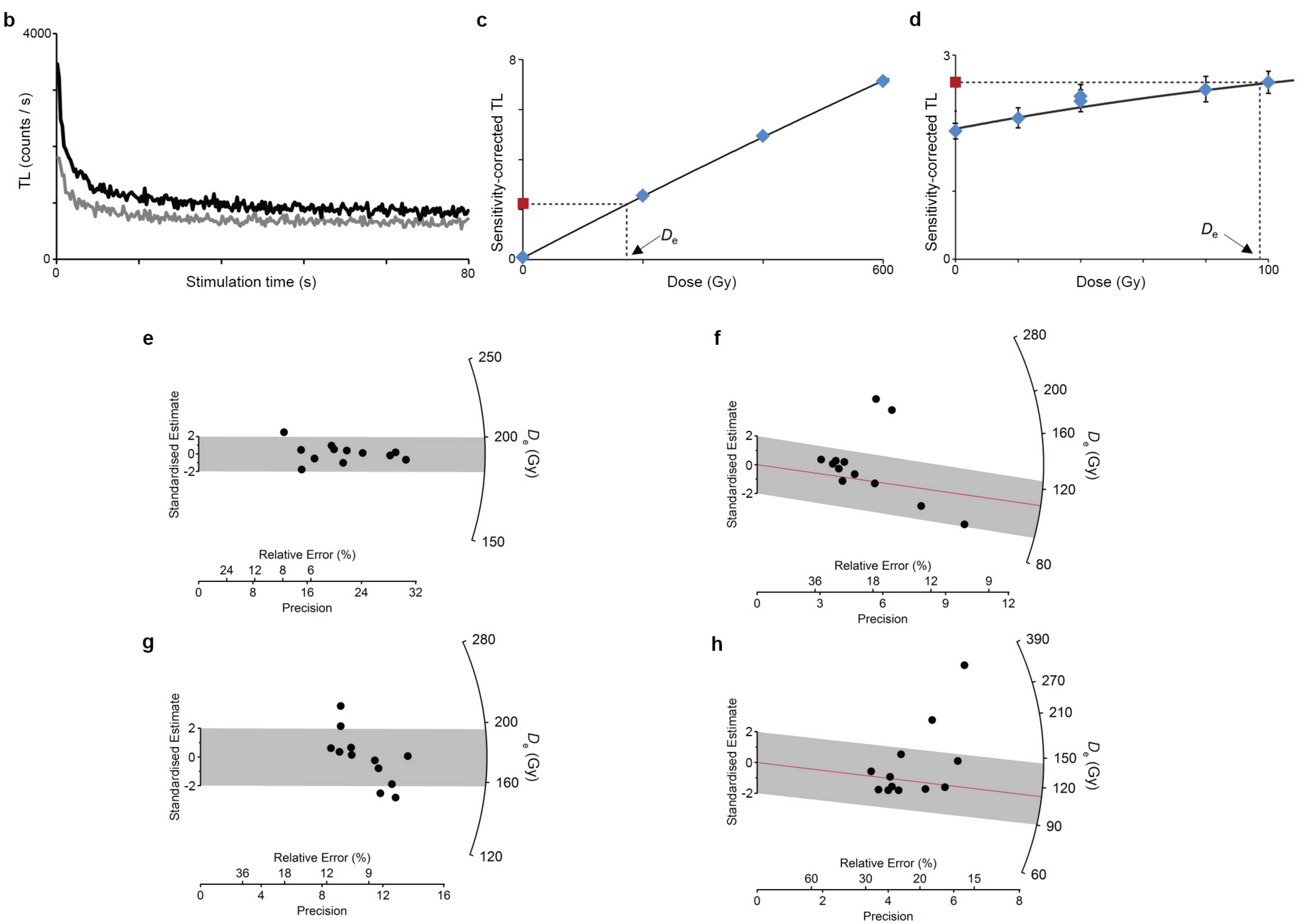
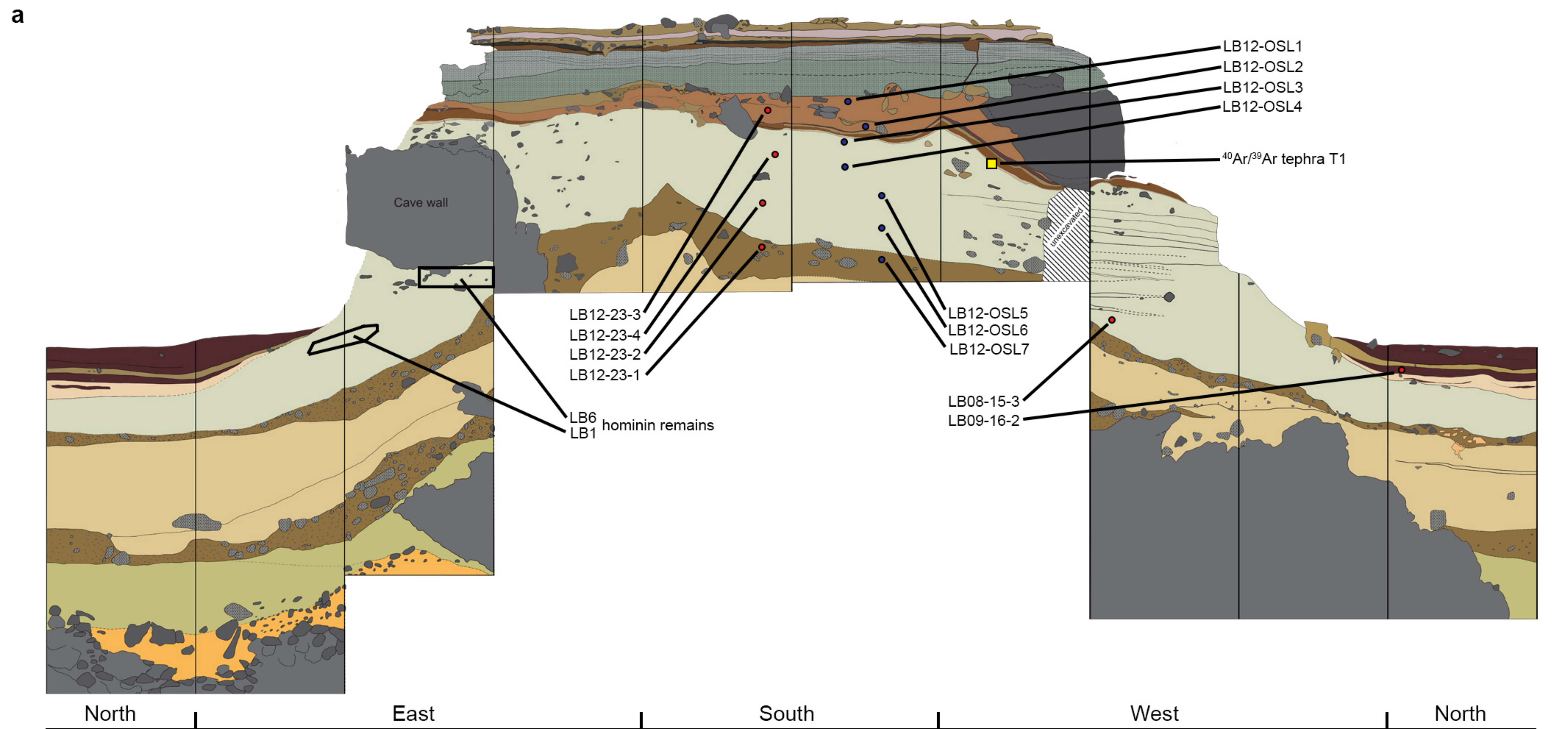
a

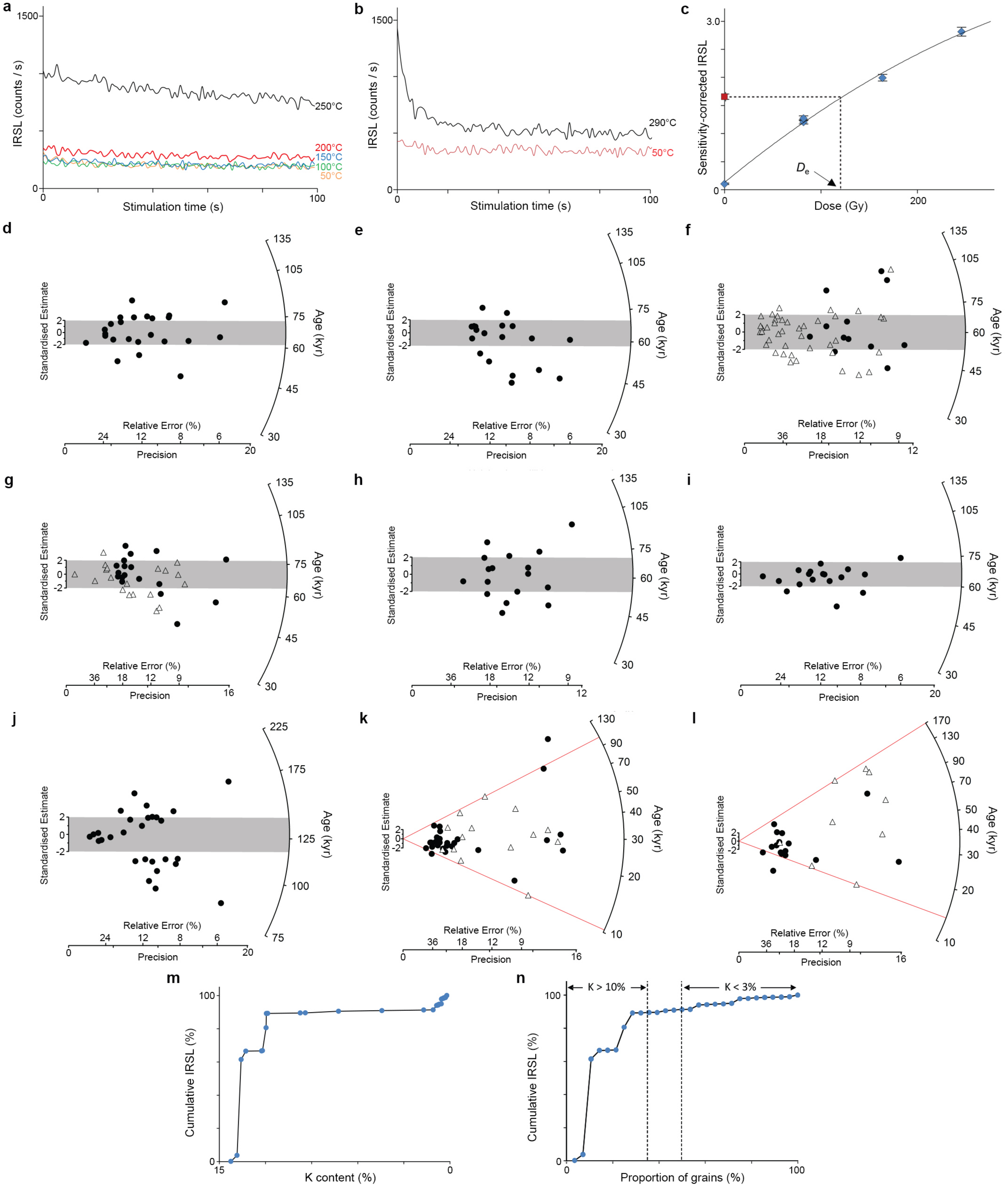


b

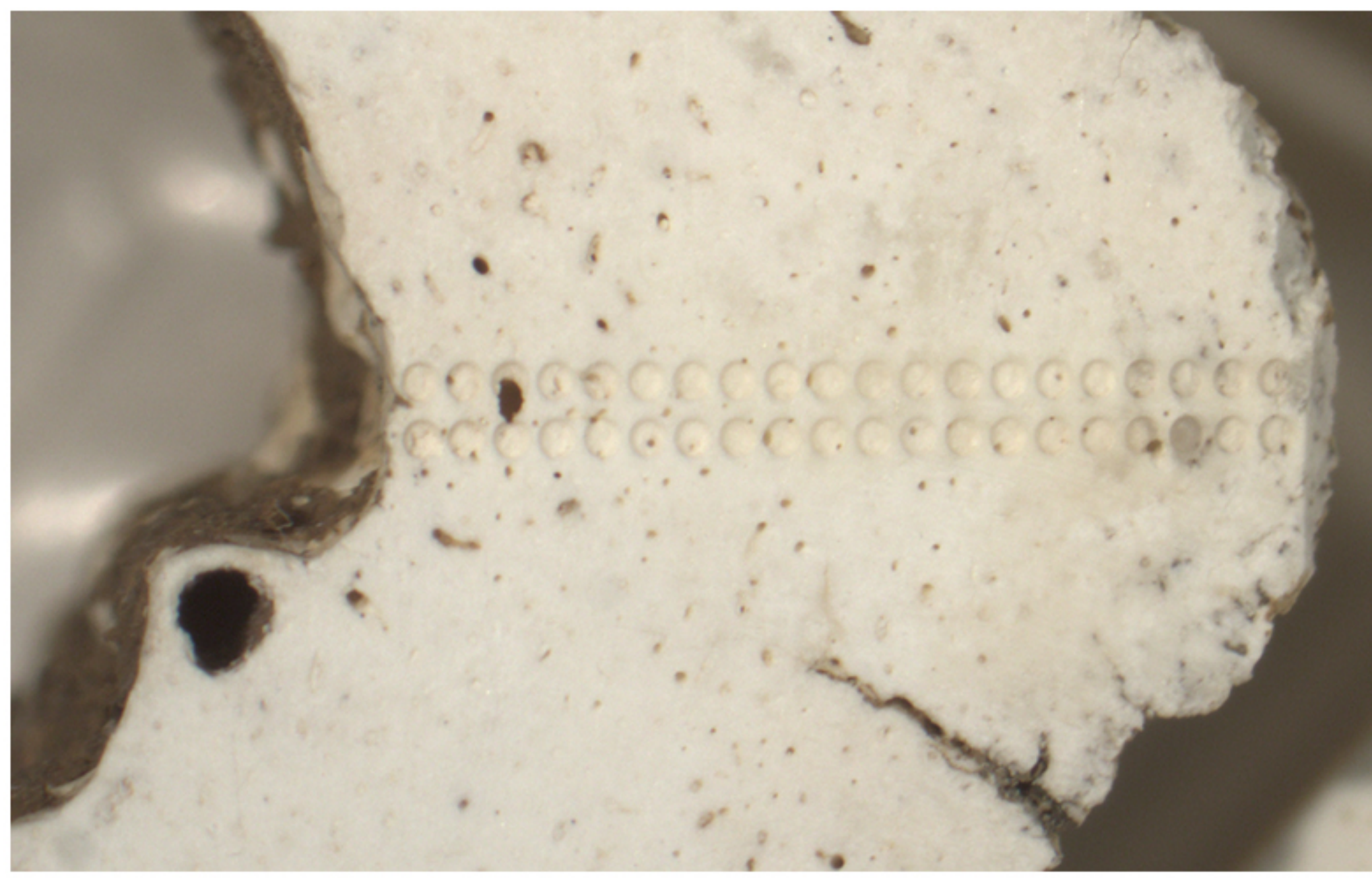
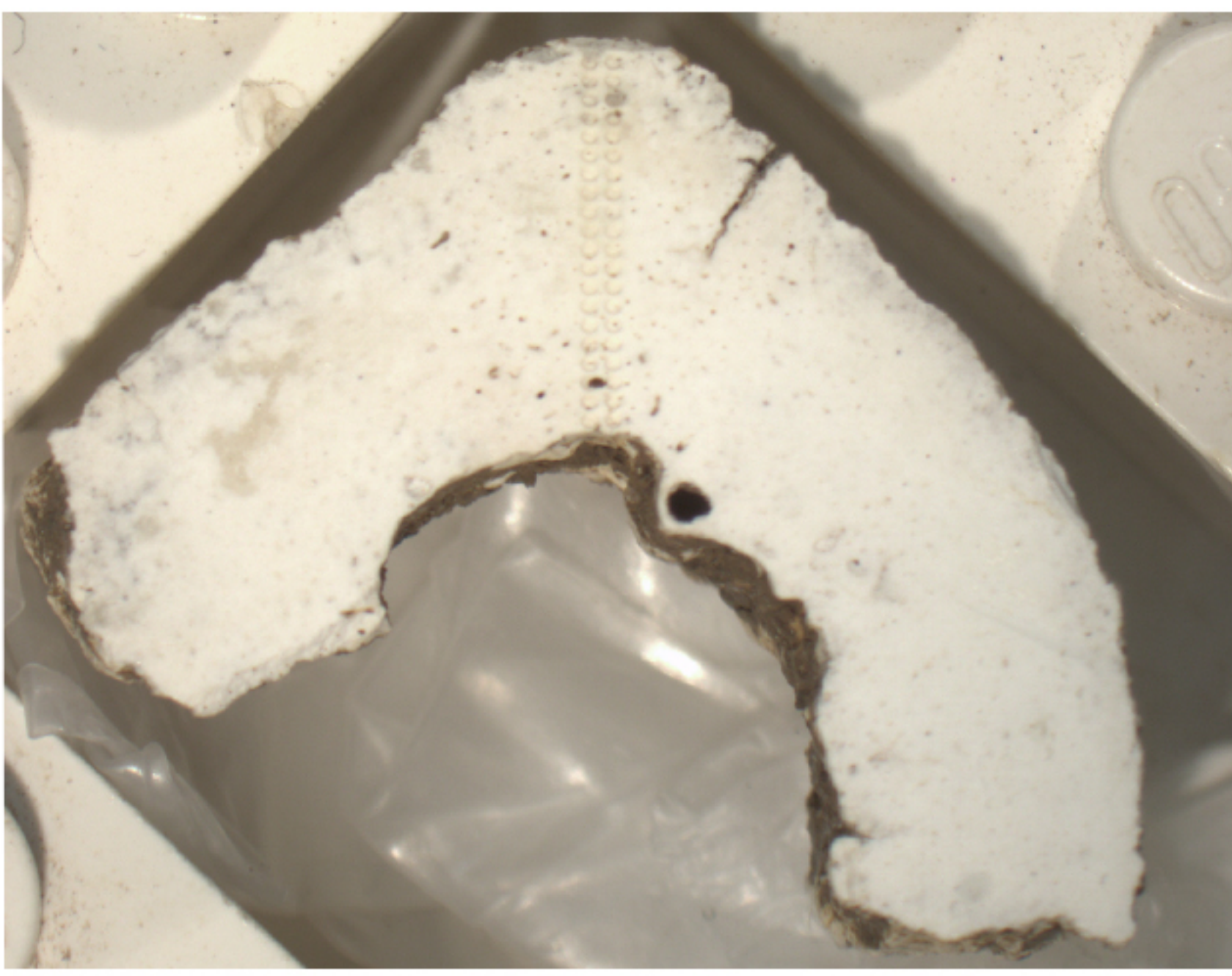


c



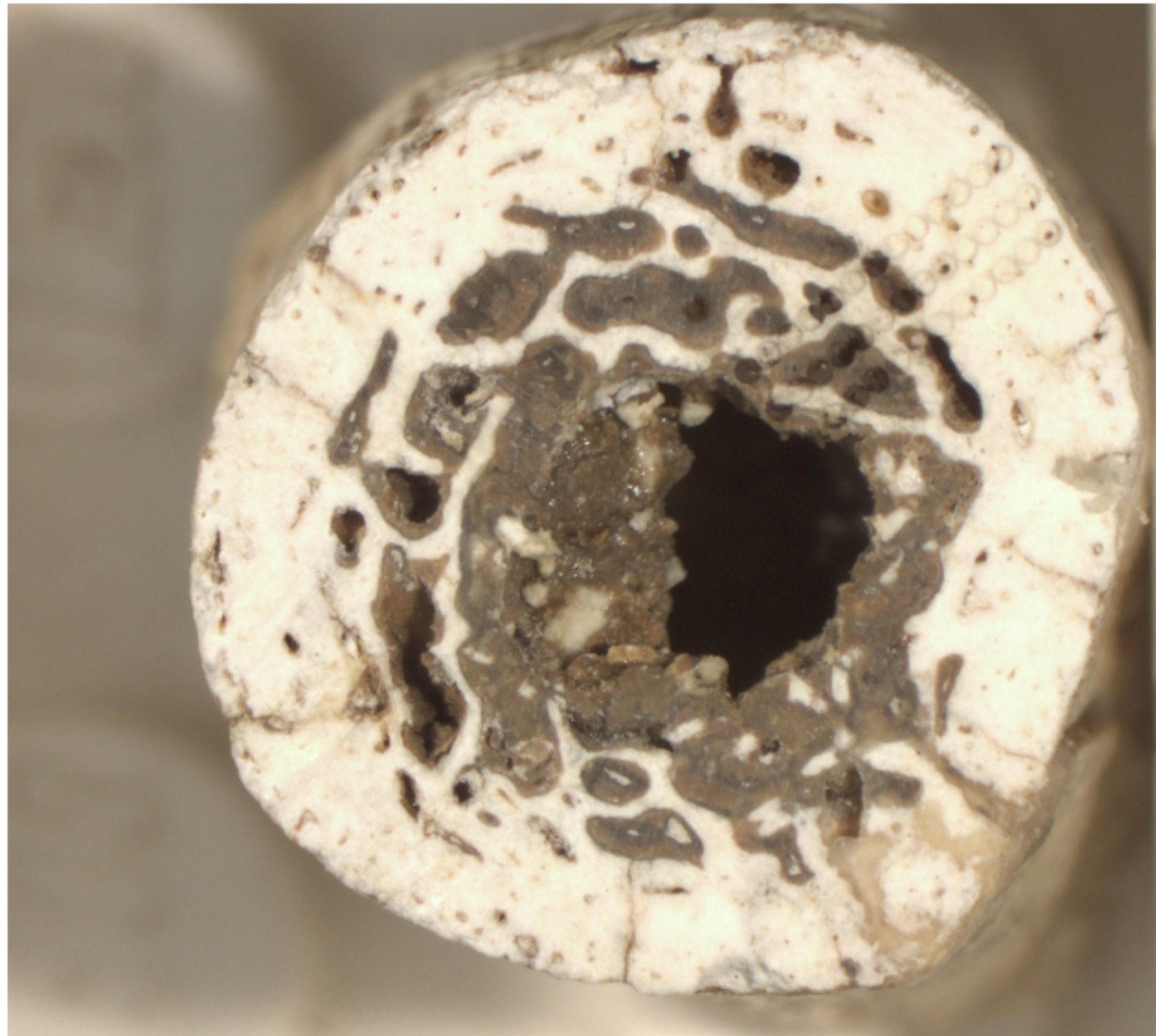


a



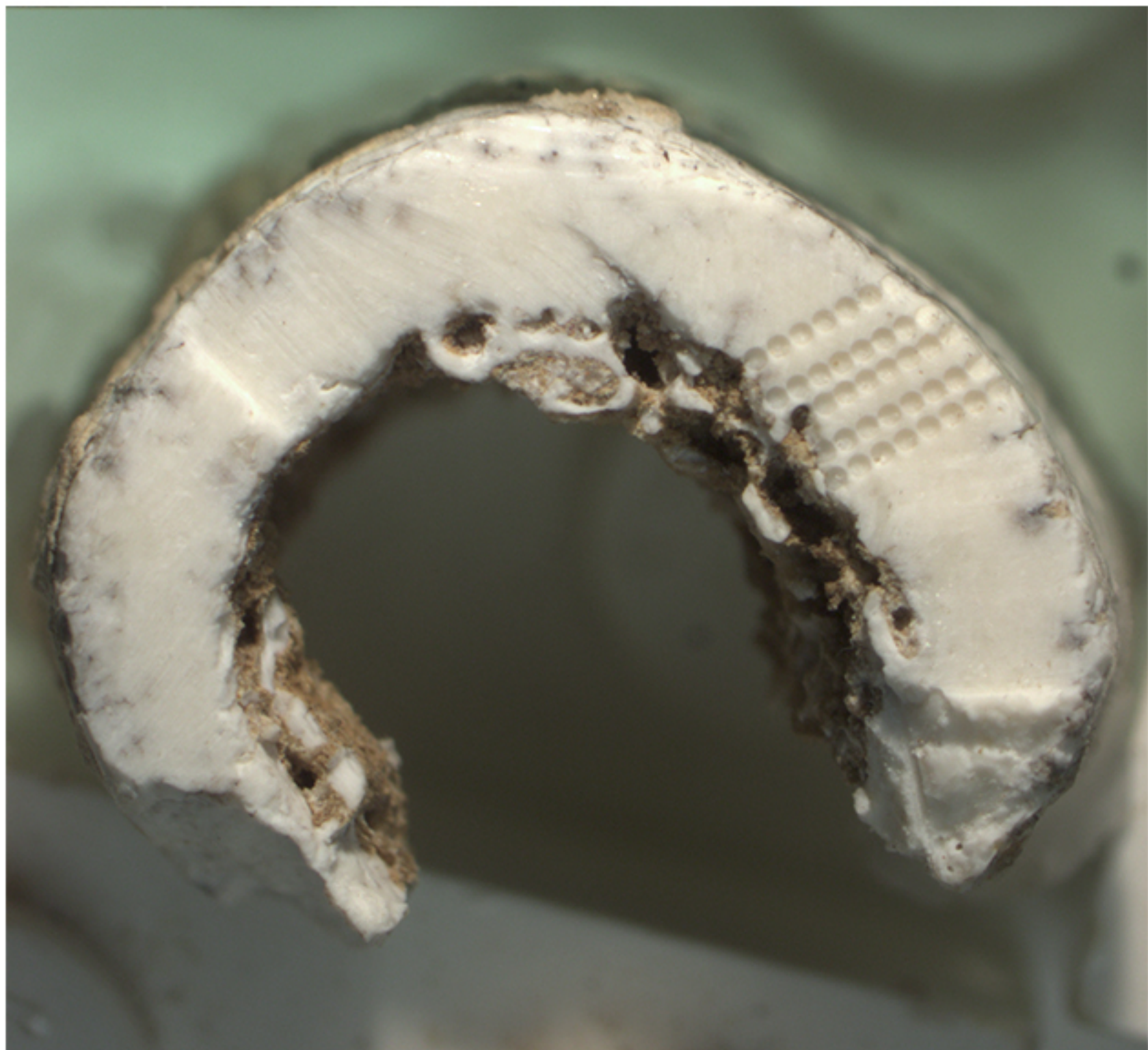
Track 1: 7.7 ± 0.5 kyr
Track 2: 7.4 ± 0.4 kyr

b



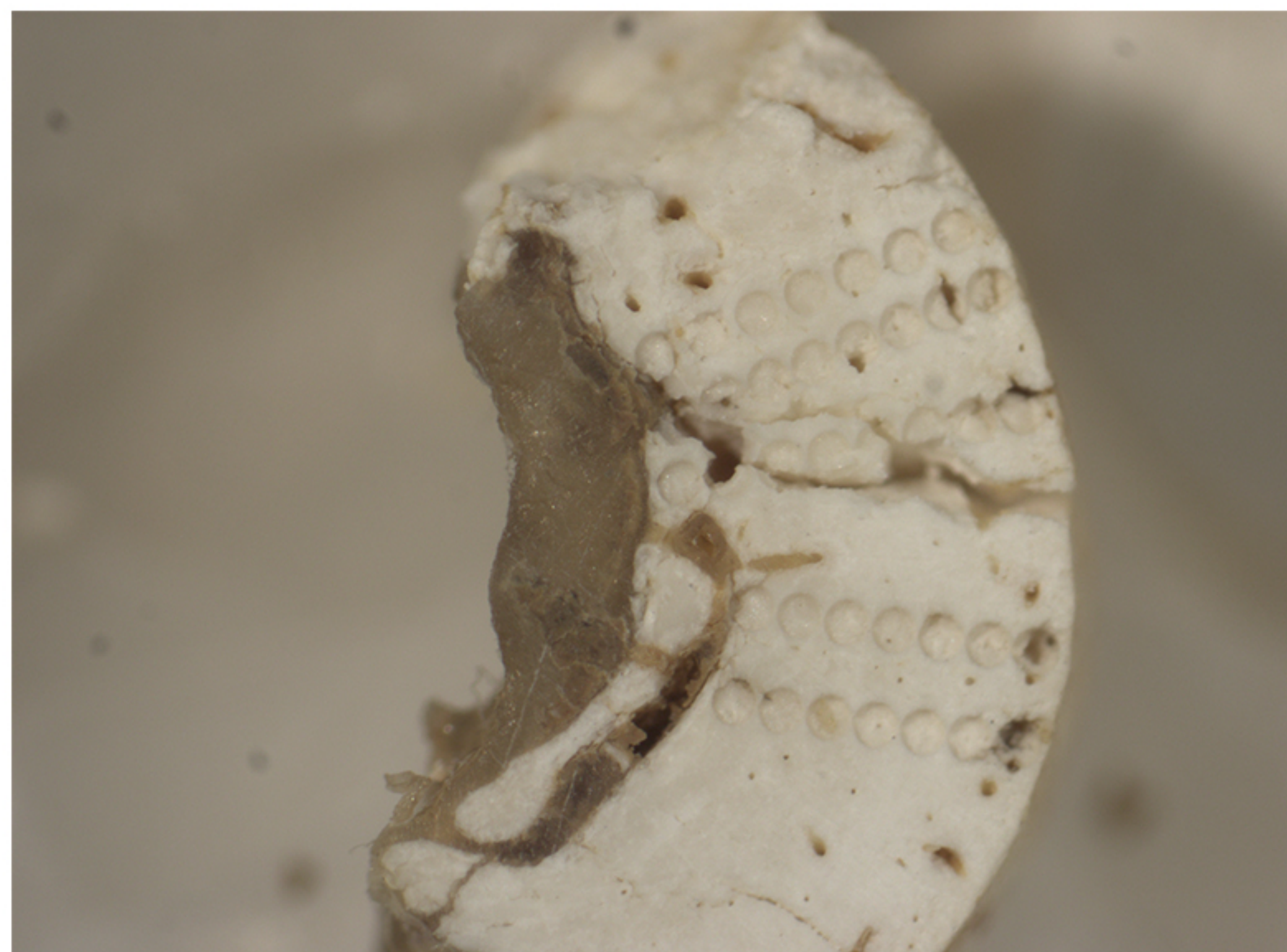
Track 1: 79.0 ± 3.7 kyr
Track 2: 71.5 ± 4.3 kyr
Track 3: 86.9 ± 7.9 kyr

c

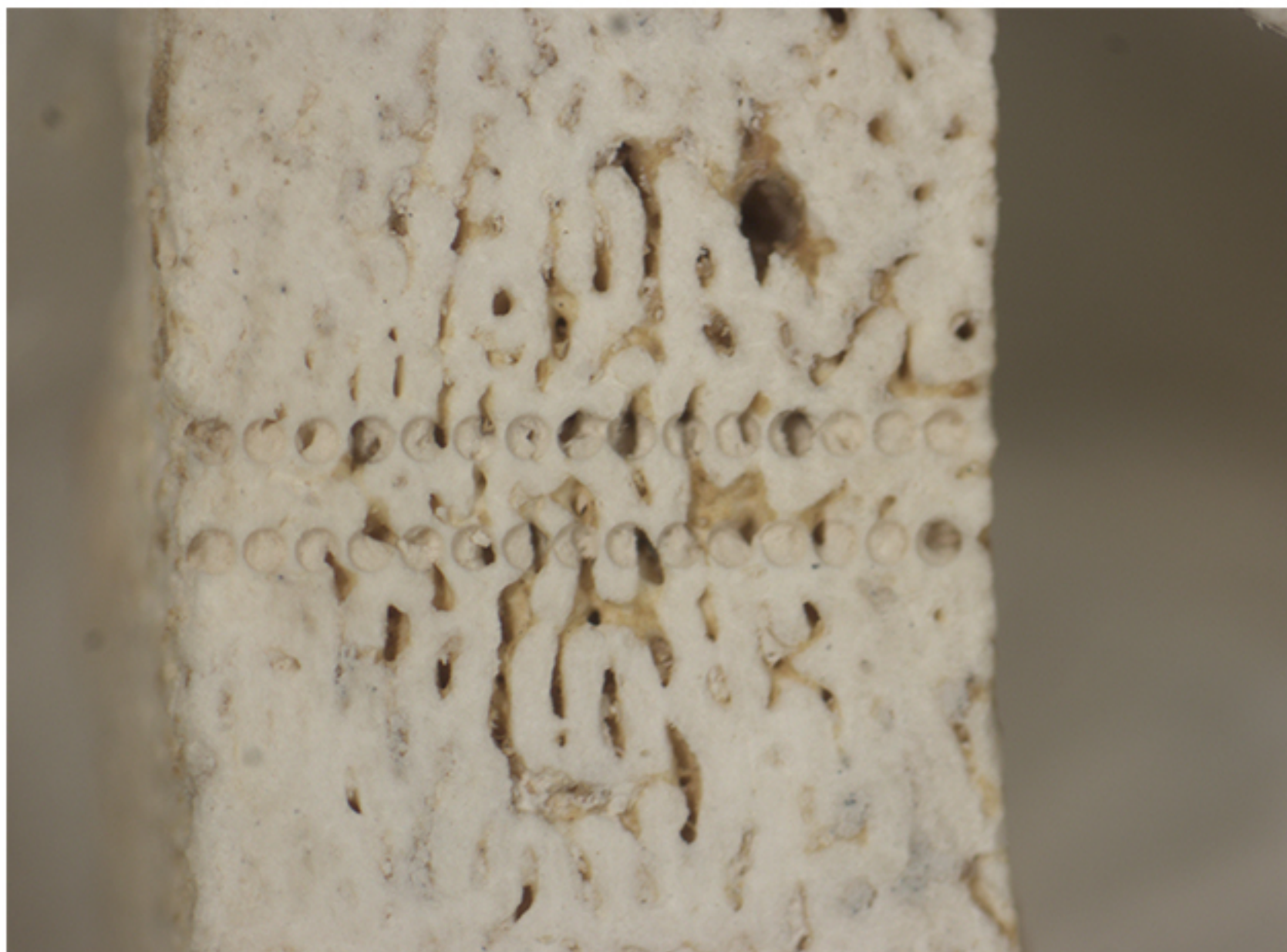


Track 5: 70.6 ± 1.7 kyr
Track 4: 69.9 ± 1.1 kyr
Track 3: 71.4 ± 1.1 kyr
Track 2: 66.7 ± 0.8 kyr
Track 1: 70.8 ± 1.2 kyr

d



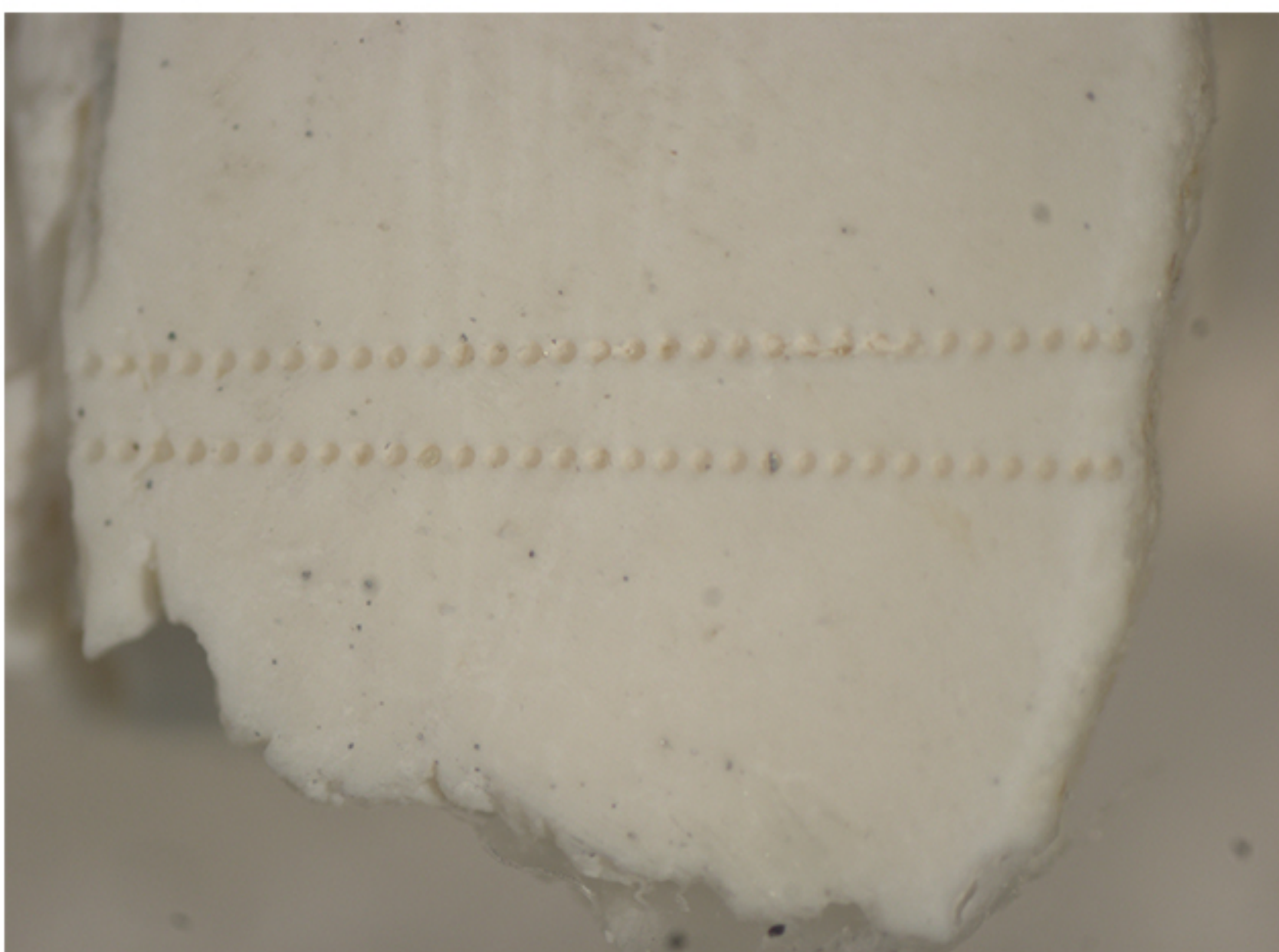
Track 1: 59.6 ± 2.3 kyr
Track 2: 54.6 ± 2.1 kyr
Track 3: 66.0 ± 4.3 kyr
Track 4: 60.4 ± 1.7 kyr
Track 5: 61.2 ± 2.3 kyr

a

Track 2: 59.9 ± 5.4 kyr
Track 1: 55.3 ± 4.2 kyr

b

Track 1: 47.4 ± 2.3 kyr
Track 2: 45.1 ± 2.6 kyr

c

Track 2: 47.2 ± 0.8 kyr
Track 1: 53.1 ± 1.2 kyr

d

Track 1: 73.7 ± 5.1 kyr
Track 2: 67.0 ± 2.4 kyr

e

Track 1: 40.5 ± 2.0 kyr

f

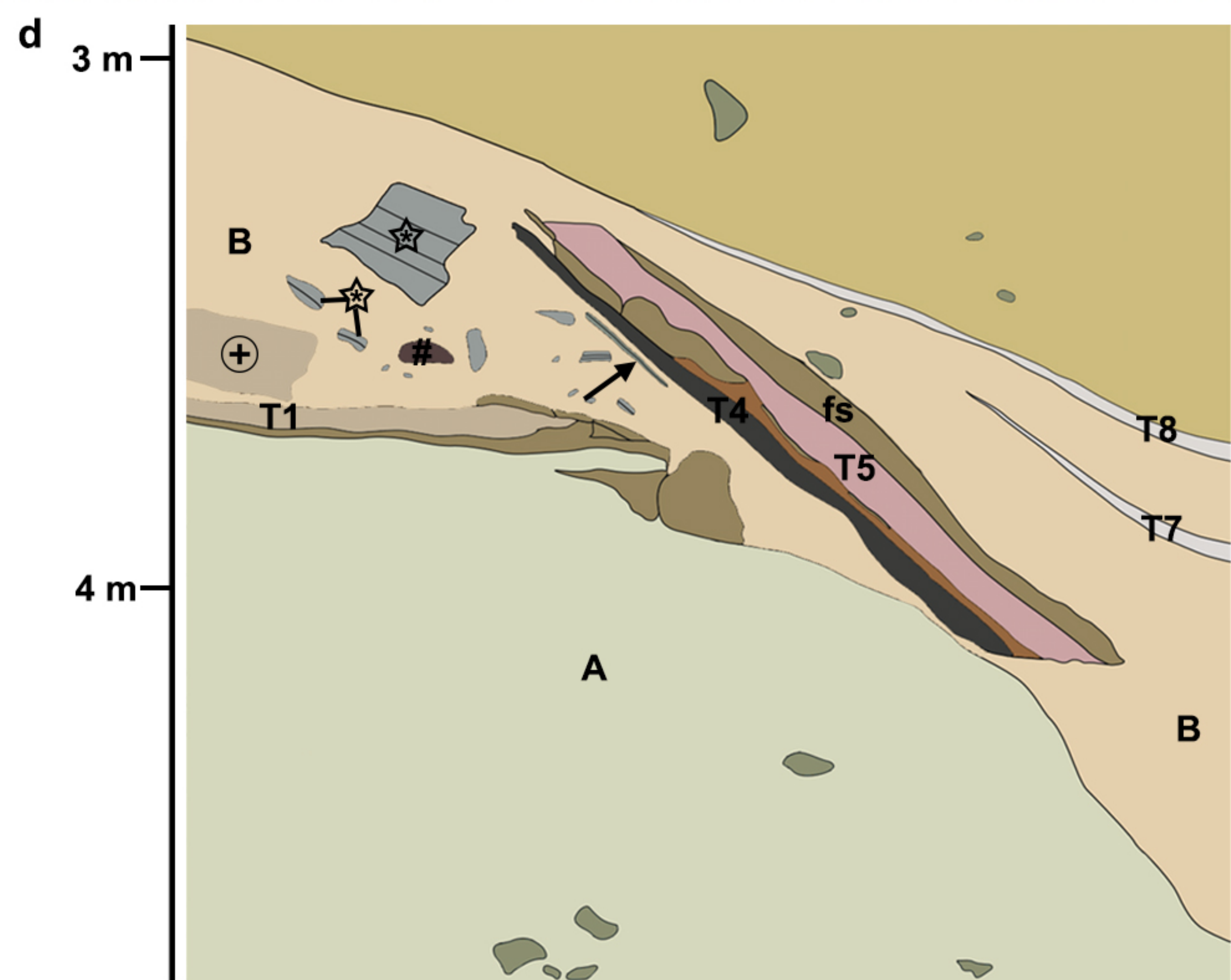
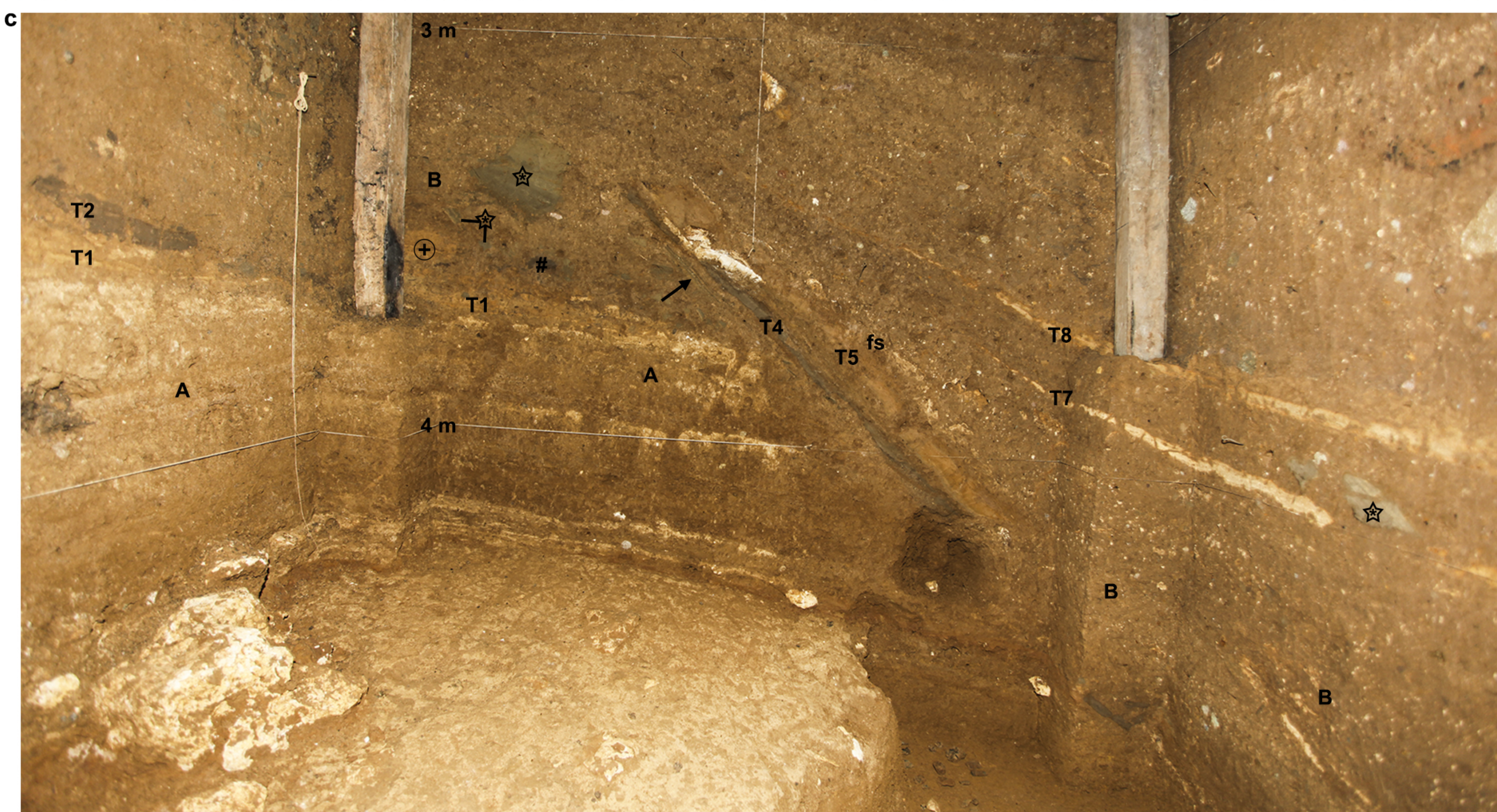
Track 2: 80.6 ± 11.3 kyr
Track 1: 78.8 ± 7.0 kyr

g

Track 2: 49.0 ± 1.5 kyr
Track 1: 49.8 ± 1.9 kyr

h

Track 1: 54.8 ± 2.3 kyr
Track 2: 51.0 ± 2.0 kyr



Supplementary Information

SI section 1:

Supplementary Discussion | Tephra deposits at Liang Bua

Supplementary Table 1 | Major element composition of glass shards at Liang Bua

SI section 2:

Supplementary Discussion | Luminescence dating of feldspar and quartz grains

Supplementary Table 2 | Dose rate data for IRSL and TL samples

Supplementary Table 3 | Equivalent doses and ages for IRSL and TL samples

SI section 3:

Supplementary Table 4 | Laser-ablation uranium-series dating of hominin bones

Supplementary Table 5 | Laser-ablation uranium-series dating of *Stegodon* bones

SI section 4:

Supplementary Table 6 | Uranium-series dating of speleothems

SI section 5:

Supplementary Table 7 | $^{40}\text{Ar}/^{39}\text{Ar}$ dating of tephra T1

SI section 6:

Supplementary Table 8 | Radiocarbon (^{14}C) dating of charcoal

SI video 1: animated summary of the stratigraphy and chronology of the Liang Bua depositional sequence.

SUPPLEMENTARY INFORMATION section 1

Supplementary Discussion | Tephra deposits at Liang Bua

Eight centimetre- to decimetre-thick layers of volcanoclastic origin occur within stratified deposits at Liang Bua (T1–T8). All volcanic layers exhibit localised post-depositional reworking, but some exhibit bedding and sorting characteristics consistent with primary deposition within Liang Bua.

T1, T7 and T8 consist of well-sorted, vitric-rich, fine sandy- to silty-textured tephric material of regional rhyolitic origin, based on major element composition of glass shards from T1 and T7 (Extended Data Fig. 3c–e and Supplementary Table 1). These three tephras were deposited in Liang Bua through a combination of primary accumulation via the cave mouth and secondary aeolian and/or rain-generated run-off processes that deposited material more deeply in the recesses of the cave. All three of these rhyolitic tephras are likely related to regional eruptive events, but they cannot at this stage be matched precisely with known inter-regional tephra marker beds (such as the ~74 kyr Youngest Toba Tuff²⁵) or regionally distributed rhyolitic tephra identified within, and adjacent to, the So'a Basin in central Flores (B.V.A., unpublished data). While the wider geographic distributions and eruptive sources of T1, T7 and T8 have yet to be determined, there remains the potential for intra- and inter-regional correlations as more tephra-bearing deposits are recognised in the region and their chemical compositions are characterised.

T2, T4, T5 and T6 consist of massive to crudely normal stratified, compacted layers of moderately sorted dark grey to pink fine to very fine ash, and are all likely related to local volcanism. These four tephras are considered to represent finely comminuted (milled) ash elutriated from, and forced into, the recesses of Liang Bua by the passage of block-and-ash flows that extended down the adjacent Wae Racang river valley. The headwaters of the Wae Racang catchment are located in a volcanic range ~14 km south of Liang Bua, near Ruteng. This volcanic range is of late Quaternary age and comprises multiple, coalesced lava domes and craters flanked by conspicuous volcanoclastic fan remnants. Some lava domes are still active today, such as Gunung Namparnos. These volcanoclastic fans have a complex architecture comprising numerous, but as yet undated, block-and-ash flow deposits. Such deposits have been identified in quarries on the flanks of Poco Likang at the tributary headwaters of the Wae Racang. Decimeter-thick sequences of coarse-grained block-and-ash flow debris have been located in side tributaries of the Wae Racang, less than 4 km upstream from Liang Bua. They exhibit extensively brecciated clasts that indicate *en masse* emplacement with percussion and associated pulverisation of constituent clasts.

T3 represents a water-supported mass flow deposit that flooded into Liang Bua from the adjacent Wae Racang river valley, most likely related to local volcanism. It is situated consistently between about 2.0 and 2.8 m depth from the eastern wall (e.g., Sector XXIII) to the cave centre (e.g., Sector XIX), and consists of three subunits. The lowermost subunit (~25–30 cm thick) is a moderately sorted, faintly bedded, upward fining, grey lithic coarse sand containing well-rounded pumiceous coarse ash and very fine lapilli with conspicuous mud rip-up clasts. The middle subunit (~15–25 cm thick) is characterised by medium to coarse sands that are severely disrupted by liquefaction/dewatering structures. The uppermost subunit (~20–30 cm thick) is characterised by millimetre- to centimetre-thick normal graded sand and silt laminations. Both subunits were deposited in quick succession, given the lack of evidence for a significant hiatus between depositional events, such as soil development or bioturbation. The sedimentological characteristics of T3 indicate its initial emplacement as a water-supported mass flow (hyperconcentrated) event (subunit 1), which subsequently consolidated and dewatered (subunit 2). Given the absence of associated debris from the cave ceiling, it seems unlikely that the liquefaction structures in subunit 2 resulted from syn- or

post-depositional volcanically and/or tectonically induced seismicity. The uppermost part of T3 (subunit 3) indicates an interval of water ponding with periodic intra-cave (rain-induced) inflow and localised redeposition. At this stage, it is unclear whether the initial emplacement of T3 represents a syn-eruptive event associated with the downstream lateral transformation of a block-and-ash flow event, or a post-eruptive event associated with flooding of the Wae Racang. The pervasive occurrence of T3 within the excavated cave deposits suggests that the level of the Wae Racang valley floor, relative to the cave entrance, was more elevated in the past than at the present day and has subsequently been down-cut. Evidence of this fluvial down-cutting is indicated by terrace remnants occupying valley margins⁷.

Supplementary Table 1 | Major element composition of glass shards at Liang Bua

Electron microprobe analysis of volcanic glass shards from tephritic (T1, T5 and T7) and water-supported mass flow deposits (T3) preserved at Liang Bua. The major element composition of the Youngest Toba Tuff is also listed³³. The ATHO-G glass standard³² was used as a calibration monitor for all runs. The data were normalised to 100% (by weight) anhydrous; the totals and standard deviations shown are for the original analyses, with the difference from 100% considered as H₂O content. FeO represents total iron. Bivariate plots of individual analyses are displayed in Extended Data Fig. 3c (FeO and CaO), 3d (FeO and K₂O) and 3e (SiO₂ and Na₂O + K₂O).

Sector	Sample	SiO ₂	Al ₂ O ₃	TiO ₂	FeO	MgO	MnO	CaO	Na ₂ O	K ₂ O	Total	<i>n</i>
XVI	T7	73.01	14.54	0.4	2.22	0.75	0.12	2.2	4.47	2.47	97.7	15
		0.28	0.16	0.02	0.07	0.03	0.02	0.06	0.18	0.04	1.65	
XXI	T5	72.19	14.37	0.49	3.22	1.23	0.12	3.6	4.18	0.95	100.04	10
		0.71	0.26	0.03	0.22	0.15	0.03	0.18	0.12	0.02	1.46	
XXI	T3	68.08	16.22	0.34	3.94	1.49	0.16	4.29	4.66	1.01	97.48	4
		0.99	1.07	0.06	0.78	0.61	0.04	0.49	0.27	0.08	0.61	
XXI	T1	76.58	13.09	0.28	1.75	0.57	0.07	2.38	3.91	1.5	96.61	6
		0.4	0.11	0.02	0.09	0.04	0.01	0.08	0.17	0.03	0.65	
Youngest Toba Tuff	YTT	77.57	12.18	0.08	0.8	0.06	0.06	0.76	3.2	5.09	97.9	207
		0.45	0.23	0.05	0.14	0.03	0.03	0.11	0.36	0.4	1.21	
Glass standard	ATHO-G	75.60	12.20	0.23	3.27	0.09	0.11	1.70	3.75	2.64	99.59	49
		0.37	0.11	0.02	0.09	0.01	0.03	0.03	0.30	0.04	0.60	

SUPPLEMENTARY INFORMATION section 2

Supplementary Discussion | Luminescence dating of feldspar and quartz grains

Infrared stimulated luminescence (IRSL)

To test the suitability of the post-infrared IRSL (pIRIR) 290 °C regenerative-dose procedure for the Liang Bua samples, routine tests⁴¹ were made for ‘recuperation’ (the signal intensity after giving the sample a zero regenerative dose, relative to the intensity of the natural sample), ‘recycling’ (the signal reproducibility for a duplicate regenerative dose) and the ‘residual dose’ remaining after an extended bleach in a solar simulator.

The extent of recuperation and the recycling ratio are obtained for each aliquot or grain during construction of the dose-response curve for D_e estimation. We rejected aliquots (and individual grains of samples LBS7-40a and -42a) with recuperation values of more than 10% and/or recycling ratios that differed from unity by more than 10%. The elevated-temperature pIRIR traps are incompletely bleached by sunlight, even after prolonged exposure, which can result in significant residual doses at the time of sediment deposition^{21,41–44}. To estimate the extent of any residual dose, we exposed 3–6 natural aliquots of samples LB12-OSL1 to -OSL7 to a solar simulator for 4 hr (duration chosen on the basis of bleaching tests on other samples^{21,42,44}) and measured the remnant doses using the pIRIR (290 °C) procedure. The mean residual dose is less than 8 Gy in all cases (Supplementary Table 3), with a weighted mean of 6.5 ± 0.5 Gy. The pIRIR signals were too dim to use the intensity-subtraction procedure for residual dose correction⁴⁴, but the dose-subtraction approach (in which the residual dose of each sample is subtracted from its measured D_e) should be satisfactory as the residual doses are small relative to the D_e values. We used the latter procedure to calculate the IRSL ages.

A ‘dose recovery’ test⁴⁷ was also conducted on sample LB12-OSL3, to check that a known (given) dose could be accurately recovered using the same measurement conditions as those used to estimate the D_e values (and residual doses) for the natural samples. Eight natural aliquots were bleached in a solar simulator for 4 hr and then given a laboratory beta dose of 123 Gy as a surrogate natural dose, which was measured using the pIRIR (290 °C) procedure. The resulting ratio of measured (recovered) dose to given dose is statistically consistent with unity (0.98 ± 0.04), after subtracting the residual dose for this sample, validating the suitability of these experimental conditions.

Anomalous fading tests were made on five samples using a single-aliquot measurement procedure similar to that described previously⁴⁶, but with the pIRIR (290 °C) experimental conditions used in this study. The rate of fading of the sensitivity-corrected pIRIR (290 °C) signal is measured as a function of storage time at room temperature, where a ‘decade’ is a factor of ten in time since laboratory irradiation. The measured fading rates range from -0.7 to 1.2% per decade (but with uncertainties that overlap at 1σ) for storage times of up to 4 days (~ 2.4 decades). The weighted mean fading rate for these five samples is $0.9 \pm 0.3\%$ per decade, which we used to correct each of the measured ages to obtain the final, fading-corrected ages⁴⁵ (Supplementary Table 3). The ages are insensitive to assumptions about past water content, increasing (or decreasing) by $\sim 0.5\%$ for each 1% increase (or decrease) in water content.

IRSL ages can be sensitive, however, to assumptions about the internal K content, especially in contexts where the external dose rate is comparatively low. Our sample preparation procedures are designed to separate K-rich feldspar grains, and we used X-ray diffraction to confirm the predominance of high-K feldspars (orthoclase, microcline and sanidine, in order of relative abundance). To obtain a direct measure of the K concentration, we conducted energy- and wavelength-dispersive X-ray spectroscopy (EDS and WDS,

respectively) analyses of 28 grains from LB12-OSL3 that yielded detectable pIRIR signals during single-grain measurements. For each grain, 4–7 spots were sampled for EDS analysis using beam diameters ranging from a few μm to a few tens of μm , and 3–5 spots were measured for WDS analysis using an electron beam size of $\sim 6\ \mu\text{m}$. Spots were located on relatively flat grain surfaces with an homogeneous appearance, and measurements were made using the instruments, procedures and reference standards described in refs 36 and 37. The EDS and WDS analyses produced consistent results, which showed that 15 grains ($\sim 54\%$ of the total) had K concentrations of less than 3% and that 9 grains ($\sim 32\%$ of the total) had K contents higher than 10%. Most of the high-K grains yielded much brighter pIRIR signals than did the low-K grains. The 5 brightest grains each had K concentrations of more than 10% and, together, accounted for $\sim 90\%$ of the total pIRIR signal emitted by all 28 grains (Extended Data Fig. 7m, n). A mean K concentration of 11.9% is obtained by weighting the K content of individual grains by their corresponding pIRIR sensitivities. Based on these results, we adopted a K concentration of $12 \pm 1\%$ to estimate the internal dose rates for all our samples, with the uncertainty sufficient to capture the likely range of variation in mean K content at 2σ .

The fading-corrected ages for individual aliquots and grains are displayed as radial plots^{47,48} in Extended Data Fig. 7d–l. For all samples, the spread among these age estimates is larger than can be explained by measurement error alone, as indicated by over-dispersion⁴⁸ (OD) values of approximately 17–43% for samples LB12-OSL1 to -OSL7, $\sim 60\%$ for LBS7-40a and $\sim 80\%$ for LBS7-42a. The OD may be due to a number of factors, such as the use of a multi-sample average fading rate for all aliquots and an average value for residual dose correction for each sample, as well as between-grain differences in the extent of bleaching before deposition and spatial variations in dose rate after burial⁴¹.

To explore the potential effect of incomplete bleaching on the single-aliquot ages, we measured 4500 and 2000 individual feldspar grains from samples LB12-OSL3 and -OSL4, respectively. Only 41 and 19 of these grains (fewer than 1% of the total measured) yielded detectable pIRIR signals (i.e., initial counts more than 3 times the background intensity), which indicates that the pIRIR signal from each aliquot (composed of a few hundred grains) is dominated by the light emitted by one or a few grains only. The distributions of fading-corrected, single-grain ages are indistinguishable from those of the single aliquots (Extended Data Fig. 7f and 6g) and yield statistically consistent D_e and OD values (Supplementary Table 3). Given the lack of evidence for incomplete bleaching, we combined the single-aliquot and single-grain data sets to estimate the burial ages of these two samples.

To allow for the observed extent of OD, whatever the sources, we used the central age model (CAM) to determine the weighted mean ages and 1σ uncertainties listed in Supplementary Table 3. The CAM does not assume that the age estimates are statistically consistent (i.e., within measurement error of a common value), but takes into account the additional source of random variation over and above that due solely to measurement error^{47,48}. Most of the single-aliquot ages (and single-grain ages for LB12-OSL3 and -OSL4) are scattered around the CAM values, but sample LB12-OSL7 shows a possible bifurcation of ages into two discrete populations (Extended Data Fig. 7j). One population is centered on ~ 80 kyr and the other on ~ 180 kyr, representing about 45% and 55% of aliquots, respectively. This sample was collected from the gravel-rich layer underlying the basal *Homo floresiensis*-bearing deposits and we cannot at present discount the possibility that it consists of mixed-age grains; the same note of caution applies to TL sample LB12-23-1, which was collected from the same layer and dated using multi-grain methods. Single-grain IRSL dating may help resolve this issue.

Of the 2000 and 1800 individual grains measured for samples LBS7-40a and -42a, respectively, only 14 (0.7%) and 9 (0.5%) grains gave detectable pIRIR signals. The ages of

these grains are scattered widely between ~10 and ~170 kyr and the same pattern is observed in the age distribution for the single aliquots (Extended Data Fig. 7k, l), presumably because (as with LB12-OSL3 and -OSL4) less than 1% of the few hundred grains on each aliquot are responsible for the emitted pIRIR signal. The OD values for the single grains and aliquots of these two samples are, accordingly, much larger than those of LB12-OSL1 to -OSL7. These results support our contention that LBS7-40a and -42a include a mixture of grains from different stratigraphic units on either side of the previously unrecognised unconformity. The finite mixture model⁴⁸ can be used to estimate the ages of discrete grain populations, such as mixtures of two or three separate components, but it is applicable only to single-grain data sets and there are too few grains of LBS7-40a and -42a to fit this model reliably.

We can discern no clear evidence for discrete populations in the age distributions of samples LBS7-40a and -42a, but around two-thirds of the single-grain and single-aliquot ages for LBS7-40a appear to form a cluster at ~30 kyr. The fading-corrected CAM age for these data is 30 ± 4 kyr, and the corresponding age for the LBS7-42a data is 36 ± 9 kyr. Neither of these ‘pooled mean’ ages should be considered reliable estimates of burial age for LB1, but we note that they are similar to the maximum ages of 38 ± 8 kyr (LBS7-40a) and 35 ± 4 kyr (LBS7-42a) obtained in the original Liang Bua study^{2,7} using the light-sensitive TL emissions from aliquots consisting of ~5000 grains of quartz. For a sample composed of mixed-age grains that are measured simultaneously, the ages will represent some kind of average, with the exact value dependent on the relative proportion of grains of different ages and their luminescence intensities. The similarity of the original TL ages and pooled mean IRSL ages for LBS7-40a and -42a is consistent, therefore, with these two samples containing grains from both sides of the unconformity.

Thermoluminescence (TL)

The dual-aliquot (DA) procedure employed in this study was developed originally for TL dating of the cave sediments at Liang Bua using the heat-induced red/orange emissions from volcanically derived quartz grains^{2,22}. A minimum of two aliquots (Aliquots A and B) are needed to estimate the D_e associated with the light-sensitive TL traps, each typically composed of several thousand quartz grains. Aliquot A is used to determine the D_e for the heat-reset TL traps and Aliquot B is used to measure the total TL signal, from which the D_e associated with the light-sensitive TL traps is obtained by subtraction. The resulting ages should conservatively be viewed as maximum estimates of the time of sediment deposition, because several hours of sunlight exposure are required to significantly deplete the light-sensitive TL traps, and not all grains on each aliquot are likely to have been fully bleached prior to burial²².

Liang Bua samples are commonly deficient in quartz and four of the samples in this study (LB09-16-2, LB12-23-2, -3 and -4) yielded enough grains to make only two aliquots of ~10,000 grains. Two of the samples (LB08-15-3 and LB12-23-1), however, contained sufficient quantities of quartz to make 12 replicates of both Aliquots A and B, enabling an assessment of between-aliquot differences in the extent of pre-depositional bleaching and its effect on D_e estimation. For both samples, Aliquot A showed little variation in D_e among the 12 aliquots, with OD values of 0% for LB08-15-3 and $13 \pm 4\%$ for LB12-23-1. We attribute this to the grains being uniformly heated during a volcanic event or situated in the proximity of volcanically heated materials. The CAM was used to determine the weighted mean D_e value for the heat-reset signal.

By contrast, the D_e values for the 12 aliquots of Aliquot B were over-dispersed to a much greater extent ($34 \pm 10\%$ for LB08-15-3 and $40 \pm 11\%$ for LB12-23-1), owing to the presence to two outlying values in each distribution (Extended Data Fig. 6f, h). These anomalously high- D_e values are identified as statistical outliers on the basis of having

normalised median absolute deviations greater than 1.5 (ref. 25) and are hypothesised to arise from incomplete bleaching of some of the constituent grains when last transported. We adopted two approaches to estimate the burial ages of these two samples. First, we removed the two D_e outliers in each of the distributions, which reduced the OD values to $8 \pm 10\%$ (LB08-15-3) and 0% (LB12-23-1), and then calculated the weighted mean using the CAM. We also applied the minimum age model (MAM)^{47,48} to all 12 D_e values in each distribution, as an alternative method of estimating the D_e associated with the population of most fully-bleached grains. Before running the MAM, we added a relative error of 20% to each of the D_e measurement errors, as an estimate of the inherent over-dispersion⁴⁸. This value was chosen on the basis of the OD values obtained for three samples (12 aliquots each) of modern hillslope and river channel sediment collected in the vicinity of Liang Bua (weighted mean of $20 \pm 1\%$), and 12 aliquots of sample LB12-23-1 that had been bleached for 4 hr using a sunlamp ($19 \pm 1\%$). For both samples, the MAM D_e values for Aliquot B are statistically indistinguishable from the corresponding CAM D_e values: 110 ± 13 Gy for LB08-15-3 and 112 ± 14 Gy for LB12-23-1, resulting in MAM ages of 91 ± 11 and 111 ± 15 kyr, respectively. Given the consistency between the MAM and CAM D_e estimates (the latter obtained after rejecting the high- D_e outliers) and the greater precision of the latter, the burial ages listed in Supplementary Table 3 for these two samples are those obtained using the CAM. This analysis suggests that the TL ages obtained for the other four samples, using only two aliquots of each, should provide reliable estimates of maximum age.

The *terminus post quem* caveat could be regarded as overcautious, given the overall consistency of the TL ages with the IRSL chronology and a variety of independent chronometers (ref. 7 and this study). The IRSL ages are typically measured with higher precision than the TL ages, due to the indirect (subtraction) method of isolating the light-sensitive TL signal, and the pIRIR traps are also bleached more rapidly than the TL traps. Consequently, the good agreement between the two luminescence-based chronologies implies that the quartz and feldspar grains were bleached sufficiently to empty the light-sensitive TL and pIRIR traps to the same low level, and that both signals should yield ages that closely approximate the time of deposition of sediments at Liang Bua.

Supplementary Table 2 | Dose rate data for IRSL and TL samples

	Sample code	Sector / depth (cm)	Grain size (μm)	Mineral / procedure ^a	Field water content (%) ^b	External dose rate (Gy/kyr) ^c			Internal dose rate (Gy/kyr) ^c	Total dose rate (Gy/kyr) ^c
						Beta	Gamma	Cosmic		
IRSL samples	LB12-OSL1	XXI / 280	90–212	feldspar / SA	26	0.41 \pm 0.03	0.32 \pm 0.02	0.06	0.63	1.41 \pm 0.15
	LB12-OSL2	XXI / 310	90–212	feldspar / SA	35	0.44 \pm 0.03	0.32 \pm 0.02	0.06	0.63	1.45 \pm 0.15
	LB12-OSL3	XXI / 329	180–212	feldspar / SA & SG	34	0.40 \pm 0.03	0.32 \pm 0.02	0.06	0.80	1.57 \pm 0.11
	LB12-OSL4	XXI / 372	180–212	feldspar / SA & SG	35	0.45 \pm 0.04	0.37 \pm 0.02	0.06	0.80	1.68 \pm 0.11
	LB12-OSL5	XXI / 410	180–212	feldspar / SA	35	0.47 \pm 0.04	0.38 \pm 0.02	0.06	0.80	1.71 \pm 0.11
	LB12-OSL6	XXI / 450	90–212	feldspar / SA	34	0.42 \pm 0.03	0.36 \pm 0.02	0.06	0.63	1.47 \pm 0.15
	LB12-OSL7	XXI / 495	90–212	feldspar / SA	26	0.39 \pm 0.03	0.33 \pm 0.02	0.05	0.63	1.40 \pm 0.15
	LBS7-40a	VII / 485–490	90–212 180–212	feldspar / SA feldspar / SG	11 11	0.80 \pm 0.05 0.79 \pm 0.04	0.94 \pm 0.05 0.94 \pm 0.05	0.05 0.05	0.63 0.80	2.42 \pm 0.16 2.58 \pm 0.12
	LBS7-42a	VII / 593–598	90–212 180–212	feldspar / SA feldspar / SG	8 8	0.90 \pm 0.05 0.88 \pm 0.05	1.13 \pm 0.06 1.13 \pm 0.06	0.05 0.05	0.63 0.80	2.71 \pm 0.17 2.86 \pm 0.13
TL samples	LB08-15-3	XV / 573	90–125	quartz / DA	36	0.41 \pm 0.04	0.72 \pm 0.02	0.05	0.03	1.21 \pm 0.05
	LB09-16-2	XVI / 640	90–125	quartz / DA	33	0.75 \pm 0.03	0.94 \pm 0.01	0.05	0.03	1.77 \pm 0.04
	LB12-23-3	XXIII / 295	90–125	quartz / DA	36	0.42 \pm 0.03	0.30 \pm 0.01	0.06	0.03	0.81 \pm 0.04
	LB12-23-4	XXIII / 347	90–125	quartz / DA	38	0.45 \pm 0.03	0.37 \pm 0.01	0.06	0.03	0.91 \pm 0.04
	LB12-23-2	XXIII / 410	90–125	quartz / DA	39	0.57 \pm 0.03	0.38 \pm 0.01	0.06	0.03	1.04 \pm 0.04
	LB12-23-1	XXIII / 490	90–125	quartz / DA	39	0.57 \pm 0.03	0.36 \pm 0.01	0.05	0.03	1.01 \pm 0.04

^a Procedure depends on the method of equivalent dose (D_e) determination. Potassium-rich feldspar grains were measured as single aliquots (**SA**) and/or as single grains (**SG**), while quartz grains were analysed using a dual-aliquot (**DA**) procedure.

^b Water content at time of sample collection. The dose rates (and ages in Supplementary Table 3) are calculated for a water content of $20 \pm 5\%$ (as explained in Methods). For the quartz samples, the calculated total dose rates increase (or decrease) by $\sim 1\%$ for each 1% decrease (or increase) in water content, while the effect is about half as much for the feldspar samples.

^c All uncertainties expressed at 1σ . The cosmic-ray dose rate has a relative uncertainty of 10%, the internal dose rate of quartz has an uncertainty of ± 0.01 Gy/kyr, and the relative uncertainties on the internal dose rates of the feldspar samples are 13% and 23% for grain sizes of 180–212 and 90–212 μm , respectively. The latter uncertainties include those associated with the assumed Rb content of $400 \pm 100 \mu\text{g g}^{-1}$ and the pIRIR signal-weighted K concentration of $12 \pm 1\%$ that we determined from measurements on individual grains of LB12-OSL3 (see Supplementary Discussion). It also accounts for variation in grain diameter within each of the selected size ranges, which we assumed to be Gaussian, giving mean grain sizes of 196 ± 8 and $151 \pm 31 \mu\text{m}$ for the 180–212 and 90–212 μm fractions, respectively, with uncertainties that span the full size range at 2σ .

Supplementary Table 3 | Equivalent doses and ages for IRSL and TL samples

	Sample code	Sector / depth (cm)	Procedure, signal ^a	Residual dose (Gy)	Equivalent dose (Gy) ^b	Over-dispersion (%) ^c	Fading rate (% per decade)	Age (kyr) ^d	
								Fading-uncorrected	Fading-corrected
IRSL samples	LB12-OSL1	XXI / 280	SA, pIRIR	4.9 ± 2.0	87 ± 8 (24)	33 ± 6	1.0 ± 0.3	62 ± 9	67 ± 9
	LB12-OSL2	XXI / 310	SA, pIRIR	7.6 ± 1.4	86 ± 14 (19)	29 ± 5	0.5 ± 0.6	59 ± 11	64 ± 13
	LB12-OSL3	XXI / 329	SA, pIRIR SG, pIRIR	5.3 ± 2.3	96 ± 11 (12) 84 ± 8 (41)	37 ± 9 43 ± 7	1.2 ± 1.4	56 ± 6	60 ± 6
	LB12-OSL4	XXI / 372	SA, pIRIR SG, pIRIR	7.8 ± 2.2	117 ± 9 (18) 100 ± 8 (19)	28 ± 6 26 ± 6		64 ± 6	70 ± 7
	LB12-OSL5	XXI / 410	SA, pIRIR	5.2 ± 1.3	98 ± 9 (17)	34 ± 7		57 ± 6	62 ± 7
	LB12-OSL6	XXI / 450	SA, pIRIR	5.4 ± 3.0	89 ± 5 (18)	17 ± 4	0.7 ± 0.9	60 ± 7	66 ± 8
	LB12-OSL7	XXI / 495	SA, pIRIR	7.0 ± 0.8	164 ± 12 (28)	33 ± 5	-0.7 ± 1.2	117 ± 15	128 ± 17
	LBS7-40a	VII / 485–490	SA, pIRIR SG, pIRIR		64 ± 8 (28) 78 ± 14 (14)	60 ± 9 64 ± 13		28 ± 3	30 ± 4
	LBS7-42a	VII / 593–598	SA, pIRIR SG, pIRIR		68 ± 13 (16) 144 ± 42 (9)	75 ± 14 88 ± 21		33 ± 8	36 ± 9
TL samples	LB08-15-3	XV / 573	DA, heat DA, light		191 ± 5 (12) 108 ± 7 (10)	0 8 ± 10		158 ± 8 89 ± 7	
	LB09-16-2	XVI / 640	DA, heat DA, light		134 ± 11 (1) 40 ± 13 (1)			76 ± 6 23 ± 7	
	LB12-23-3	XXIII / 295	DA, heat DA, light		246 ± 19 (1) 48 ± 10 (1)			304 ± 28 59 ± 13	
	LB12-23-4	XXIII / 347	DA, heat DA, light		273 ± 15 (1) 66 ± 18 (1)			300 ± 21 73 ± 20	
	LB12-23-2	XXIII / 410	DA, heat DA, light		292 ± 16 (1) 72 ± 17 (1)			281 ± 19 69 ± 17	
	LB12-23-1	XXIII / 490	DA, heat DA, light		176 ± 9 (12) 114 ± 8 (10)	13 ± 4 0		174 ± 11 113 ± 9	

^a Measurement procedure used to estimate the equivalent dose (D_e): single-aliquot (SA), single-grain (SG) and dual-aliquot (DA) regenerative-dose procedures. Luminescence signal used for dating: **pIRIR**, post-infrared IRSL (290 °C); **heat**, heat-reset TL; **light**, light-sensitive TL.

^b Weighted mean ± 1σ uncertainty, calculated using the central age model for all samples. Two high- D_e outliers were rejected from both the LB08-15-3 and LB12-23-1 data sets prior to running the model (see Supplementary Discussion). The numbers of aliquots or grains used for D_e determination are enclosed in parentheses, and a systematic error of 2% was added (in quadrature) to the propagated random errors to allow for any bias associated with calibration of the laboratory beta sources. The D_e values for samples LB12-OSL1 to -OSL7 are corrected for the measured residual doses in the adjacent (left-hand) column.

^c Over-dispersion (OD) value ± 1σ uncertainty, calculated using the central age model. The OD represents the spread in D_e values remaining after taking measurement uncertainties into account⁴⁸. The OD would be zero if 95% of the individual D_e values in each sample were consistent with a common D_e value at 2σ.

^d Calculated as the central age model D_e divided by the total dose rate (see Supplementary Table 2), with the uncertainty expressed at 1σ. The weighted mean of the 5 measured fading rates ($0.9 ± 0.3\%$) was used to correct the IRSL ages for anomalous fading. The most reliable estimates of depositional age are highlighted in **bold**: the fading-corrected IRSL ages and the TL ages obtained from the light-sensitive signal. The IRSL ages for LB12-OSL3 and -OSL4 are based on the results from both the SA and SG measurements. The ages listed for samples LBS7-40a and -42a are included for comparison with those reported in ref. 2, but they are not considered reliable estimates of burial time for LB1 (see Supplementary Discussion). To determine the weighted mean age for different samples, each age was weighted by the inverse square of its standard error, which included only random sources of error; the total systematic error was added in quadrature afterwards.

SUPPLEMENTARY INFORMATION section 3

Supplementary Table 4 | Laser-ablation uranium-series dating of hominin bones

Laser-ablation uranium-series isotope analyses and dating results for bones of 1 modern human (132A/LB/IV/27D/03) and 3 specimens of *Homo floresiensis* (LB1/52, LB2/1 and LB6/3). All errors are at 2σ . Data are listed for every spot measured along each of 2–5 tracks across each cut section of bone (see Extended Data Fig. 8 for photos of each sample). All tracks are from the interior to the exterior of the bones. Ages cannot be calculated for spot measurements with $^{230}\text{Th}/^{234}\text{U}$ ratios much greater than 1 and are accordingly left blank. Analyses with U/Th ratios of ≤ 300 (marked in red) and data points suspected of being affected by uranium leaching or secondary overprinting (marked in blue) were also not used to calculate the DAD model ages (shown in bold).

	132A/LB/ IV/27D/03	U (ppm)	Th (ppb)	U/Th	$^{230}\text{Th}/^{238}\text{U}$	$^{230}\text{Th}/^{238}\text{U}$ error	$^{234}\text{U}/^{238}\text{U}$	$^{234}\text{U}/^{238}\text{U}$ error	Age (kyr)	Age error
Track 1	1	18.0	14	1296	0.0606	0.0023	1.2729	0.0048	5.3	0.2
	2	11.7	13	928	0.0668	0.0024	1.2654	0.0061	5.9	0.2
	3	13.7	80	172	0.0927	0.0029	1.2728	0.0103	8.2	0.3
	4	18.2	16	1174	0.0614	0.0020	1.2660	0.0032	5.4	0.2
	5	19.3	15	1274	0.0666	0.0018	1.2652	0.0045	5.9	0.2
	6	23.0	3	7335	0.0655	0.0013	1.2657	0.0045	5.8	0.1
	7	25.1	9	2915	0.0658	0.0019	1.2677	0.0034	5.8	0.2
	8	26.1	3	9386	0.0664	0.0016	1.2538	0.0086	5.9	0.1
	9	24.4	4	5952	0.0683	0.0016	1.2673	0.0036	6.0	0.2
	10	26.6	6	4426	0.0698	0.0015	1.2651	0.0030	6.2	0.1
	11	33.4	3	12267	0.0642	0.0014	1.2730	0.0064	5.6	0.1
	12	27.2	1	18156	0.0707	0.0015	1.2579	0.0080	6.3	0.1
	13	27.4	3	8353	0.0700	0.0014	1.2688	0.0034	6.2	0.1
	14	26.8	2	13479	0.0719	0.0015	1.2660	0.0035	6.4	0.1
	15	25.5	14	1786	0.0758	0.0011	1.2668	0.0048	6.7	0.1
	16	22.4	2	12938	0.0795	0.0019	1.2613	0.0057	7.1	0.2
	17	22.8	2	9959	0.0765	0.0017	1.2631	0.0034	6.8	0.2
	18	25.1	3	7967	0.0887	0.0017	1.2692	0.0047	7.9	0.2
	19	24.5	5	5288	0.0851	0.0015	1.2727	0.0031	7.5	0.1
	20	23.7	11	2255	0.0837	0.0014	1.2693	0.0060	7.4	0.1
							DAD fit		7.7	0.5
Track 2	1	12.3	3	3844	0.0643	0.0037	1.2720	0.0141	5.7	0.3
	2	12.7	3	4349	0.0619	0.0028	1.2777	0.0067	5.4	0.3
	3	12.5	8	1598	0.0679	0.0026	1.2753	0.0084	6.0	0.2
	4	14.2	1	13855	0.0695	0.0033	1.2768	0.0072	6.1	0.3
	5	19.8	11	1825	0.0595	0.0020	1.2764	0.0060	5.2	0.2
	6	18.0	16	1116	0.0648	0.0030	1.2732	0.0109	5.7	0.3
	7	20.0	17	1195	0.0713	0.0026	1.2740	0.0050	6.3	0.2
	8	27.2	1	20592	0.0686	0.0019	1.2787	0.0042	6.0	0.2
	9	26.7	14	1857	0.0688	0.0021	1.2719	0.0141	6.1	0.2
	10	32.3	3	12082	0.0667	0.0024	1.2981	0.0151	5.7	0.2
	11	33.9	2	20865	0.0696	0.0025	1.2729	0.0028	6.1	0.2
	12	37.7	10	3922	0.0619	0.0017	1.2787	0.0090	5.4	0.2
	13	30.7	1	29412	0.0670	0.0025	1.2732	0.0076	5.9	0.2
	14	25.2	7	3499	0.0680	0.0032	1.2802	0.0130	5.9	0.3
	15	28.9	13	2301	0.0783	0.0025	1.2720	0.0074	6.9	0.2
	16	29.0	7	3918	0.0805	0.0020	1.2769	0.0063	7.1	0.2
	17	27.5	9	2950	0.0773	0.0032	1.2807	0.0057	6.8	0.3
	18	30.1	1	20878	0.0671	0.0031	1.2763	0.0037	5.9	0.3
	19	19.6	2	11341	0.0913	0.0044	1.2734	0.0061	8.1	0.4
	20	14.8	4	3458	0.0870	0.0051	1.2759	0.0106	7.7	0.5
							DAD fit		7.4	0.5

[illegible]

LB2/1		U (ppm)	Th (ppb)	U/Th	²³⁰ Th/ ²³⁸ U	²³⁰ Th/ ²³⁸ U error	²³⁴ U/ ²³⁸ U	²³⁴ U/ ²³⁸ U error	Age (kyr)	Age error
Track 1	1	56.8	28	2034	0.4436	0.0128	1.3253	0.0040	43.7	1.5
	2	58.6	4	13659	0.5979	0.0061	1.3142	0.0022	64.4	0.9
	3	43.8	2	19335	0.6080	0.0042	1.3104	0.0037	66.1	0.7
	4	57.7	2	32616	0.6198	0.0038	1.3129	0.0019	67.7	0.6
	5	58.8	1	61464	0.6147	0.0032	1.3136	0.0023	66.9	0.5
	6	57.3	2	37009	0.6224	0.0032	1.3063	0.0027	68.6	0.5
	7	51.6	5	11222	0.6060	0.0046	1.3086	0.0037	66.0	0.7
	8	52.8	15	3584	0.6424	0.0059	1.3125	0.0028	71.1	0.9
							DAD fit	70.8	1.2	
Track 2	1	44.0	29	1501	0.5963	0.0082	1.3208	0.0041	63.7	1.2
	2	46.8	4	12391	0.6121	0.0126	1.3177	0.0069	66.2	1.9
	3	48.9	2	30015	0.6058	0.0056	1.3276	0.0056	64.6	0.9
	4	55.4	1	42103	0.6126	0.0035	1.3141	0.0048	66.6	0.6
	5	52.4	1	76115	0.5955	0.0040	1.3213	0.0037	63.6	0.6
	6	50.2	1	46785	0.5770	0.0112	1.3215	0.0077	61.0	1.6
	7	42.4	2	20440	0.5976	0.0208	1.3249	0.0078	63.7	3.0
	8	50.1	12	4166	0.5880	0.0127	1.3142	0.0037	63.0	1.8
							DAD fit	66.7	0.8	
Track 3	1	28.0	584	48	0.5664	0.0101	1.3099	0.0029	60.3	1.4
	2	55.5	3	18645	0.6343	0.0025	1.3180	0.0064	69.5	0.6
	3	52.1	1	47357	0.6125	0.0046	1.3177	0.0034	66.3	0.7
	4	54.7	1	42271	0.6338	0.0042	1.3154	0.0021	69.6	0.7
	5	57.7	2	33613	0.6366	0.0042	1.3168	0.0024	69.9	0.6
	6	55.7	1	43911	0.6248	0.0034	1.3145	0.0058	68.3	0.7
	7	54.4	3	16019	0.6167	0.0035	1.3098	0.0026	67.5	0.5
	8	57.7	19	3108	0.6265	0.0086	1.3098	0.0020	68.9	1.3
							DAD fit	71.4	1.1	
Track 4	1	56.1	16	3585	0.6021	0.0078	1.3152	0.0017	65.0	1.1
	2	54.5	6	8981	0.6355	0.0033	1.3195	0.0021	69.5	0.5
	3	52.4	1	52352	0.6214	0.0039	1.3241	0.0021	67.1	0.6
	4	54.8	1	58980	0.6349	0.0042	1.3199	0.0039	69.4	0.7
	5	54.7	1	53718	0.6211	0.0042	1.3219	0.0060	67.2	0.8
	6	52.4	1	36824	0.6073	0.0094	1.3135	0.0046	65.8	1.4
	7	54.2	3	18437	0.6182	0.0037	1.3144	0.0043	67.3	0.6
	8	54.9	15	3671	0.6422	0.0079	1.3117	0.0028	71.1	1.2
							DAD fit	69.9	1.1	
Track 5	1	50.3	25	2044	0.5895	0.0052	1.3150	0.0019	63.2	0.8
	2	49.9	3	19862	0.6229	0.0040	1.3172	0.0039	67.8	0.7
	3	54.2	1	68895	0.6288	0.0050	1.3176	0.0021	68.7	0.8
	4	52.0	2	33547	0.6457	0.0035	1.3177	0.0022	71.2	0.6
	5	55.0	1	36695	0.6170	0.0052	1.3079	0.0084	67.7	1.0
	6	44.9	6	7561	0.6189	0.0043	1.3122	0.0028	67.6	0.7
	7	43.0	12	3513	0.5607	0.0029	1.3103	0.0023	59.5	0.4
							DAD fit	70.6	1.7	

[illegible]

Laser-ablation uranium-series isotope analyses and dating results for bones of 8 specimens of *Stegodon florensis insularis* from Sector XI. All errors are at 2σ . Data are listed for every spot measured along each pair of tracks (or a single track in the case of U-s-05/LB/XI/51/04) across each cut section of bone (see Extended Data Fig. 9 for photos of each sample). All tracks are from the interior to the exterior of the bones. Analyses with U/Th ratios of ≤ 300 (marked in red) and data points suspected of being affected by uranium leaching or secondary overprinting (marked in blue) were not used to calculate the DAD model ages (shown in bold).

U-s-01/ LB/XI/ 32/04		U (ppm)	Th (ppb)	U/Th	²³⁰ Th/ ²³⁸ U	²³⁰ Th/ ²³⁸ U error	²³⁴ U/ ²³⁸ U	²³⁴ U/ ²³⁸ U error	Age (kyr)	Age error
Track 1	1	15.8	53	300	0.4651	0.0106	1.3113	0.0032	46.9	1.3
	2	32.4	30	1096	0.3940	0.0105	1.3101	0.0029	38.5	1.2
	3	20.2	33	606	0.4049	0.0060	1.3056	0.0050	39.9	0.7
	4	19.1	101	189	0.3534	0.0096	1.3132	0.0044	33.8	1.1
	5	26.2	37	708	0.3975	0.0093	1.3145	0.0023	38.7	1.1
	6	24.0	44	539	0.3828	0.0084	1.3107	0.0030	37.2	1.0
	7	23.0	25	920	0.3778	0.0096	1.3188	0.0042	36.3	1.1
	8	22.6	105	215	0.4147	0.0080	1.3071	0.0050	41.0	1.0
	9	11.1	287	39	0.5390	0.0109	1.3100	0.0049	56.5	1.5
	10	18.7	145	129	0.4338	0.0055	1.3058	0.0053	43.3	0.7
	11	24.1	88	273	0.5041	0.0079	1.3140	0.0042	51.7	1.0
	12	14.1	147	96	0.5111	0.0093	1.3168	0.0064	52.5	1.3
	13	24.9	15	1708	0.4459	0.0086	1.3155	0.0048	44.4	1.1
	14	22.3	8	2904	0.4673	0.0056	1.3165	0.0051	47.0	0.7
	15	17.6	5	3237	0.5320	0.0087	1.3193	0.0076	55.1	1.2
							DAD fit	55.3	4.2	
Track 2	1	20.0	22	893	0.4869	0.0142	1.3122	0.0042	49.6	1.8
	2	26.3	11	2341	0.4978	0.0078	1.3098	0.0024	51.1	1.0
	3	18.5	29	632	0.4792	0.0065	1.3045	0.0089	49.0	0.9
	4	21.1	58	362	0.5030	0.0066	1.3126	0.0031	51.7	0.9
	5	20.4	30	683	0.4063	0.0079	1.3116	0.0043	39.8	0.9
	6	19.8	72	275	0.5081	0.0090	1.3123	0.0039	52.3	1.2
	7	15.7	43	367	0.4203	0.0060	1.3144	0.0041	41.4	0.7
	8	20.1	95	212	0.4701	0.0051	1.3130	0.0031	47.5	0.7
	9	20.6	44	467	0.4614	0.0119	1.3142	0.0022	46.3	1.5
	10	22.4	32	690	0.4326	0.0056	1.3088	0.0042	43.1	0.7
	11	21.2	35	599	0.5303	0.0089	1.3169	0.0030	55.0	1.2
	12	29.0	5	6182	0.5366	0.0086	1.3065	0.0042	56.4	1.2
	13	22.8	26	874	0.5194	0.0085	1.3163	0.0030	53.6	1.1
	14	28.4	14	1975	0.5030	0.0074	1.3149	0.0028	51.5	1.0
	15	16.0	69	232	0.5603	0.0089	1.3188	0.0091	58.9	1.3
							DAD fit	59.9	5.4	

[illegible]

U-s-03/										
LB/XI/		U	Th			²³⁰ Th/ ²³⁸ U		²³⁴ U/ ²³⁸ U		
47/04		(ppm)	(ppb)	U/Th	²³⁰ Th/ ²³⁸ U	error	²³⁴ U/ ²³⁸ U	error	Age (kyr)	Age error
Track 1	1	51.3	2	28803	0.5151	0.0052	1.3146	0.0045	53.1	0.7
	2	29.6	0	78573	0.4758	0.0083	1.3033	0.0056	48.6	1.1
	3	39.4	1	40100	0.4671	0.0084	1.3119	0.0048	47.2	1.1
	4	47.2	2	25712	0.4962	0.0065	1.3035	0.0055	51.3	0.9
	5	49.2	2	26874	0.4673	0.0053	1.3122	0.0059	47.2	0.7
	6	52.6	2	33220	0.4674	0.0070	1.3102	0.0069	47.3	0.9
	7	51.0	2	31615	0.4655	0.0065	1.3050	0.0050	47.3	0.8
	8	46.1	2	26241	0.4619	0.0071	1.3074	0.0054	46.7	0.9
	9	52.6	2	25865	0.4641	0.0075	1.3005	0.0057	47.3	1.0
	10	49.9	1	81937	0.4770	0.0080	1.3050	0.0062	48.7	1.1
	11	45.3	2	25137	0.4612	0.0067	1.3087	0.0049	46.6	0.9
	12	52.4	1	39472	0.4796	0.0055	1.2985	0.0051	49.4	0.7
	13	52.5	3	18738	0.4784	0.0068	1.3093	0.0060	48.7	0.9
	14	49.0	3	14640	0.4749	0.0069	1.3084	0.0041	48.3	0.9
	15	43.6	2	20111	0.4471	0.0066	1.3038	0.0044	45.1	0.8
	16	52.1	3	20331	0.4570	0.0067	1.3070	0.0046	46.1	0.9
	17	48.7	2	22504	0.4395	0.0070	1.3031	0.0060	44.2	0.9
	18	47.9	3	18745	0.4398	0.0095	1.3028	0.0045	44.2	1.2
	19	49.4	3	14532	0.4459	0.0076	1.3060	0.0044	44.8	0.9
	20	49.1	6	8806	0.4304	0.0061	1.3002	0.0053	43.2	0.8
	21	51.9	2	27387	0.4519	0.0084	1.3036	0.0038	45.7	1.1
	22	51.6	3	16077	0.4370	0.0061	1.3059	0.0036	43.7	0.8
	23	49.4	4	13888	0.4371	0.0079	1.3077	0.0048	43.7	1.0
	24	44.6	16	2832	0.4252	0.0071	1.3011	0.0042	42.5	0.9
	25	47.0	3	15608	0.4246	0.0085	1.3083	0.0035	42.1	1.0
	26	46.6	2	22928	0.4176	0.0084	1.3012	0.0050	41.6	1.0
	27	45.0	3	16195	0.4183	0.0077	1.3022	0.0050	41.6	0.9
	28	41.4	2	21478	0.4057	0.0079	1.3092	0.0061	39.9	1.0
	29	30.7	4	8211	0.3942	0.0093	1.3056	0.0055	38.7	1.1
	30	34.7	14	2535	0.4458	0.0069	1.3064	0.0053	44.8	0.9
							DAD fit	53.1	1.2	
Track 2	1	48.3	3	14397	0.4711	0.0073	1.3055	0.0070	48.0	1.0
	2	36.8	0	167199	0.4830	0.0107	1.3057	0.0049	49.4	1.4
	3	36.4	2	16574	0.4657	0.0060	1.3088	0.0065	47.1	0.8
	4	47.3	2	29534	0.4833	0.0074	1.3141	0.0045	49.1	1.0
	5	48.3	3	17594	0.4721	0.0082	1.3036	0.0080	48.2	1.1
	6	49.4	2	26285	0.4722	0.0080	1.3132	0.0058	47.7	1.0
	7	50.6	1	43024	0.4668	0.0066	1.3060	0.0053	47.4	0.9
	8	52.0	2	29515	0.4675	0.0076	1.3105	0.0051	47.3	1.0
	9	52.1	1	46480	0.4634	0.0088	1.3097	0.0044	46.8	1.1
	10	49.3	0	126916	0.4627	0.0081	1.3071	0.0041	46.8	1.0
	11	50.4	1	98336	0.4483	0.0069	1.3066	0.0043	45.1	0.9
	12	42.3	0	151291	0.4691	0.0064	1.3084	0.0064	47.6	0.9
	13	51.3	1	48537	0.4751	0.0063	1.3100	0.0047	48.2	0.8
	14	48.1	0	114019	0.4431	0.0075	1.2985	0.0044	44.8	0.9
	15	46.9	1	72792	0.4492	0.0079	1.3050	0.0052	45.3	1.0
	16	38.4	1	64732	0.4678	0.0097	1.3083	0.0052	47.4	1.2
	17	40.7	2	24935	0.4618	0.0097	1.3048	0.0047	46.8	1.2
	18	41.1	0	85723	0.4484	0.0058	1.3036	0.0036	45.2	0.7
	19	46.9	1	50405	0.4448	0.0063	1.3061	0.0049	44.7	0.8
	20	43.0	2	21432	0.4380	0.0081	1.3086	0.0043	43.7	1.0
	21	37.9	1	45244	0.4105	0.0093	1.3032	0.0052	40.7	1.1
	22	39.9	1	33496	0.4136	0.0078	1.3027	0.0039	41.1	0.9
	23	39.4	1	35193	0.4499	0.0097	1.3046	0.0038	45.4	1.2
	24	37.7	1	29133	0.3899	0.0085	1.3028	0.0046	38.3	1.0
	25	40.1	1	28917	0.4187	0.0111	1.3080	0.0055	41.4	1.3
	26	40.5	1	43624	0.4225	0.0081	1.2992	0.0044	42.3	1.0
	27	42.3	1	62104	0.4236	0.0080	1.3039	0.0043	42.2	1.0
	28	41.0	0	118676	0.4146	0.0084	1.3014	0.0039	41.2	1.0
	29	34.9	1	46063	0.4164	0.0072	1.3061	0.0047	41.3	0.9
	30	28.5	2	15935	0.4208	0.0092	1.3071	0.0053	41.7	1.1
							DAD fit	47.2	0.8	

[illegible]

U-s-05/										
LB/XI/	U	Th	U/Th	$^{230}\text{Th}/^{238}\text{U}$	$^{230}\text{Th}/^{238}\text{U}$	$^{234}\text{U}/^{238}\text{U}$	$^{234}\text{U}/^{238}\text{U}$	Age	Age	
51/04	(ppm)	(ppb)			error		error	(kyr)	error	
Track 1	1	10.6	29	362	0.2563	0.0153	1.3090	0.0071	23.6	1.6
	2	16.6	15	1116	0.2362	0.0107	1.3053	0.0040	21.6	1.1
	3	12.7	2	5700	0.3257	0.0057	1.2993	0.0063	31.2	0.7
	4	16.1	3	4946	0.2481	0.0111	1.3045	0.0036	22.8	1.1
	5	15.5	26	601	0.2529	0.0106	1.3069	0.0040	23.3	1.1
	6	15.7	4	3985	0.3181	0.0050	1.2988	0.0048	30.3	0.6
	7	14.7	7	1996	0.3107	0.0089	1.3084	0.0051	29.3	1.0
	8	17.5	2	9304	0.2776	0.0084	1.3041	0.0044	25.9	0.9
	9	13.0	9	1473	0.2866	0.0085	1.2941	0.0046	27.1	0.9
	10	15.6	12	1289	0.3372	0.0061	1.3068	0.0059	32.2	0.7
	11	17.4	10	1725	0.2838	0.0119	1.3092	0.0039	26.4	1.3
	12	19.2	10	1852	0.2501	0.0067	1.3026	0.0050	23.1	0.7
	13	22.2	21	1075	0.2992	0.0061	1.3087	0.0036	28.1	0.7
	14	24.8	5	5132	0.3174	0.0077	1.3121	0.0052	29.9	0.8
	15	27.1	5	5557	0.2993	0.0063	1.2981	0.0034	28.3	0.7
	16	22.9	4	5267	0.2891	0.0080	1.3051	0.0043	27.1	0.9
	17	25.5	5	4678	0.2934	0.0106	1.3014	0.0032	27.6	1.1
	18	20.6	3	7717	0.3044	0.0073	1.3007	0.0032	28.8	0.8
	19	26.1	4	6320	0.2955	0.0053	1.3027	0.0038	27.8	0.6
	20	27.0	38	718	0.2542	0.0095	1.3060	0.0034	23.4	1.0
	21	23.5	16	1464	0.3302	0.0047	1.3040	0.0045	31.5	0.5
	22	18.7	2	9223	0.3161	0.0064	1.3030	0.0039	30.0	0.7
	23	27.8	4	6383	0.3313	0.0089	1.2972	0.0075	31.8	1.0
	24	27.4	1	24869	0.3398	0.0074	1.3060	0.0058	32.5	0.8
	25	23.4	2	10011	0.3201	0.0075	1.3125	0.0029	30.2	0.8
	26	22.9	4	5924	0.3102	0.0071	1.3073	0.0044	29.3	0.8
	27	25.0	4	5810	0.3656	0.0072	1.3060	0.0033	35.4	0.8
	28	25.1	2	13842	0.3522	0.0069	1.3144	0.0063	33.6	0.8
	29	28.1	6	5061	0.3796	0.0057	1.3043	0.0026	37.0	0.7
	30	31.6	2	18569	0.3558	0.0061	1.2964	0.0029	34.6	0.7
	31	33.4	2	13657	0.3804	0.0063	1.2982	0.0030	37.3	0.7
	32	24.6	4	5487	0.4057	0.0057	1.3003	0.0031	40.2	0.7
	33	21.7	1	15988	0.4248	0.0067	1.3123	0.0032	42.0	0.8
	34	19.3	5	3785	0.4739	0.0078	1.3087	0.0050	48.2	1.0
	35	16.4	22	747	0.4838	0.0066	1.3144	0.0030	49.1	0.8
	DAD fit							40.5	2.0	

U-s/06/ LB/XI/ 52/04		U (ppm)	Th (ppb)	U/Th	²³⁰ Th/ ²³⁸ U	²³⁰ Th/ ²³⁸ U error	²³⁴ U/ ²³⁸ U	²³⁴ U/ ²³⁸ U error	Age (kyr)	Age error
Track 1	1	17.8	428	42	0.3424	0.0261	1.3750	0.0375	30.8	2.9
	2	37.2	203	183	0.3864	0.0132	1.3157	0.0127	37.4	1.6
	3	19.0	97	197	0.5532	0.0174	1.3359	0.0077	56.9	2.4
	4	15.4	120	129	0.5137	0.0103	1.3312	0.0085	52.1	1.4
	5	37.2	39	947	0.4522	0.0132	1.3299	0.0023	44.5	1.6
	6	32.9	47	700	0.5287	0.0112	1.3351	0.0089	53.8	1.5
	7	24.2	18	1375	0.5731	0.0106	1.3366	0.0048	59.5	1.5
	8	24.9	19	1276	0.5431	0.0109	1.3316	0.0034	55.8	1.5
	9	32.6	13	2444	0.5359	0.0081	1.3193	0.0026	55.6	1.1
	10	31.4	7	4729	0.6162	0.0078	1.3211	0.0033	66.6	1.2
	11	37.9	9	4063	0.6353	0.0067	1.3203	0.0023	69.4	1.0
	12	38.4	7	5296	0.6814	0.0075	1.3166	0.0026	76.8	1.2
							DAD fit	78.8	7.0	
Track 2	1	5.8	297	20	0.7719	0.0330	1.3271	0.0096	90.9	6.0
	2	13.4	378	35	0.7177	0.0173	1.3381	0.0064	80.7	2.9
	3	13.5	337	40	0.5213	0.0372	1.3283	0.0072	53.2	4.9
	4	17.5	18	955	0.4624	0.0066	1.3333	0.0066	45.6	0.8
	5	18.5	19	990	0.5751	0.0112	1.3303	0.0056	60.2	1.6
	6	24.0	7	3589	0.5599	0.0070	1.3308	0.0051	58.1	1.0
	7	24.6	56	439	0.6296	0.0115	1.3262	0.0056	68.1	1.7
	8	28.1	7	4125	0.5823	0.0081	1.3226	0.0080	61.7	1.2
	9	30.2	10	3003	0.6209	0.0145	1.3202	0.0083	67.3	2.2
	10	37.6	10	3719	0.6635	0.0089	1.3205	0.0029	73.7	1.4
							DAD fit	80.6	11.3	

[illegible]

U-s-08/ LB/XI/ 65B/04		U (ppm)	Th (ppb)	U/Th	²³⁰ Th/ ²³⁸ U	²³⁰ Th/ ²³⁸ U error	²³⁴ U/ ²³⁸ U	²³⁴ U/ ²³⁸ U error	Age (kyr)	Age error
Track 1	1	44.0	55	802	0.3554	0.0103	1.3627	0.0036	32.5	1.1
	2	48.7	19	2602	0.3879	0.0065	1.3579	0.0035	36.2	0.7
	3	43.1	71	603	0.3531	0.0058	1.3624	0.0082	32.3	0.7
	4	40.6	107	381	0.2907	0.0063	1.3566	0.0029	26.0	0.6
	5	50.0	61	822	0.3843	0.0083	1.3561	0.0022	35.8	0.9
	6	58.5	16	3728	0.4014	0.0040	1.3505	0.0055	37.9	0.5
	7	54.2	18	3066	0.4198	0.0039	1.3521	0.0037	39.9	0.5
	8	52.1	19	2729	0.4387	0.0049	1.3562	0.0016	41.9	0.6
	9	44.7	31	1447	0.4331	0.0061	1.3515	0.0042	41.4	0.7
	10	61.6	9	6483	0.4104	0.0066	1.3562	0.0020	38.7	0.7
	11	60.5	19	3257	0.4259	0.0054	1.3505	0.0022	40.6	0.6
	12	59.7	12	5126	0.3901	0.0041	1.3551	0.0019	36.5	0.4
	13	66.5	9	7433	0.4184	0.0041	1.3543	0.0016	39.7	0.5
	14	61.0	8	7303	0.4409	0.0038	1.3541	0.0044	42.2	0.5
	15	68.4	5	13381	0.4512	0.0027	1.3555	0.0024	43.4	0.3
	16	83.1	12	7219	0.4997	0.0032	1.3570	0.0038	49.1	0.4
	17	73.2	10	7518	0.5112	0.0039	1.3632	0.0050	50.1	0.5
	18	61.5	8	7553	0.5096	0.0040	1.3688	0.0067	49.7	0.6
	19	56.4	13	4370	0.4802	0.0041	1.3602	0.0019	46.6	0.5
	20	57.2	21	2686	0.5229	0.0034	1.3651	0.0021	51.5	0.4
							DAD fit	54.8	2.3	
Track 2	1	40.5	12	3374	0.4512	0.0068	1.3746	0.0100	42.6	0.9
	2	35.1	29	1221	0.4044	0.0033	1.3668	0.0031	37.7	0.4
	3	38.1	35	1104	0.3912	0.0082	1.3604	0.0030	36.4	0.9
	4	39.2	54	728	0.4111	0.0090	1.3823	0.0183	37.9	1.2
	5	55.7	24	2324	0.4005	0.0068	1.3663	0.0061	37.3	0.8
	6	49.5	31	1582	0.4027	0.0058	1.3685	0.0110	37.4	0.7
	7	47.2	15	3206	0.3870	0.0040	1.3656	0.0046	35.8	0.5
	8	45.3	32	1409	0.4372	0.0084	1.3620	0.0024	41.5	1.0
	9	50.9	3	14646	0.4262	0.0031	1.3667	0.0037	40.1	0.4
	10	56.6	10	5705	0.4402	0.0052	1.3631	0.0058	41.8	0.6
	11	62.6	11	5934	0.4199	0.0077	1.3489	0.0139	40.0	1.0
	12	60.7	9	6996	0.4358	0.0060	1.3547	0.0028	41.6	0.7
	13	54.7	17	3309	0.4594	0.0069	1.3693	0.0039	43.8	0.8
	14	59.3	23	2596	0.4874	0.0062	1.3638	0.0027	47.3	0.8
	15	64.2	5	12101	0.4770	0.0055	1.3650	0.0031	46.0	0.7
	16	61.8	7	8973	0.4872	0.0043	1.3690	0.0044	47.0	0.5
	17	67.5	34	1989	0.4866	0.0079	1.3684	0.0032	47.0	0.9
	18	76.9	9	8702	0.4949	0.0049	1.3651	0.0035	48.1	0.6
	19	64.5	10	6575	0.4893	0.0087	1.3580	0.0095	47.7	1.1
	20	66.0	28	2355	0.4681	0.0045	1.3639	0.0070	45.0	0.6
							DAD fit	51.0	2.0	

SUPPLEMENTARY INFORMATION section 4

Supplementary Table 6 | Uranium-series dating of speleothems

Uranium (^{238}U , ^{234}U) and thorium (^{232}Th , ^{230}Th) isotopic analyses and $^{230}\text{Th}/^{234}\text{U}$ ages for *in situ* calcitic flowstones and a small stalagmite (LB/S.XXI 10-01 and -01R). The corrected ages listed in the far right-hand column are considered the most accurate. All uncertainties are expressed at 2σ .

Sample code ^a	Sector / depth (cm)	U (ppm)	^{232}Th (ppb)	$^{230}\text{Th}/^{232}\text{Th}$	$^{230}\text{Th}/^{238}\text{U}$	$^{234}\text{U}/^{238}\text{U}$	Uncorrected age (kyr)	Corrected initial $^{234}\text{U}/^{238}\text{U}$	Corrected age (kyr)
LB07-SXII-F1	XII / 245–255	0.05210 ± 0.00010	1.102 ± 0.007	54.77 ± 0.44	0.382 ± 0.002	1.033 ± 0.002	50.2 ± 0.4	1.038 ± 0.003	49.6 ± 0.5
LB-S.XXI 5 #08	XXI / 255–260	0.09635 ± 0.00004	0.053 ± 0.001	2250 ± 14	0.404 ± 0.001	1.026 ± 0.001	54.6 ± 0.2	1.030 ± 0.001	54.6 ± 0.2
LB-S.XXI 8-T #09	XXI / 255–260	0.08685 ± 0.00003	0.830 ± 0.001	128.16 ± 0.55	0.404 ± 0.002	1.023 ± 0.001	54.7 ± 0.3	1.027 ± 0.001	54.4 ± 0.3
LB-S.XXI 8-B #10	XXI / 255–260	0.08339 ± 0.00003	0.407 ± 0.001	252.41 ± 0.94	0.406 ± 0.001	1.028 ± 0.001	54.7 ± 0.3	1.033 ± 0.001	54.6 ± 0.3
LB/S.XXI 10-01R	XXI / tip of stalagmite	0.28140 ± 0.00013	7.335 ± 0.014	53.57 ± 0.23	0.460 ± 0.002	1.027 ± 0.002	64.7 ± 0.4	1.033 ± 0.003	64.0 ± 0.5
LB/S.XXI 10-01	XXI / top of stalagmite	0.33919 ± 0.00016	1.049 ± 0.005	459.1 ± 2.6	0.468 ± 0.002	1.027 ± 0.001	66.2 ± 0.3	1.033 ± 0.001	66.1 ± 0.3
LB07-SXII-F4	XII / 482	0.27760 ± 0.00020	6.288 ± 0.032	57.78 ± 0.38	0.431 ± 0.002	1.031 ± 0.002	58.9 ± 0.4	1.037 ± 0.002	58.3 ± 0.5
LB09-SXVII-F1	XVII / 583	0.10263 ± 0.00013	2.609 ± 0.008	64.23 ± 0.48	0.538 ± 0.003	1.017 ± 0.002	81.5 ± 0.7	1.022 ± 0.003	80.8 ± 0.8
LB09-SXVII-F2	XVII / 565	0.12253 ± 0.00016	1.043 ± 0.005	175.6 ± 1.6	0.492 ± 0.003	1.023 ± 0.002	71.1 ± 0.6	1.028 ± 0.003	70.8 ± 0.6
LB09-SXVII-F3	XVII / 568	0.10027 ± 0.00010	4.189 ± 0.001	36.89 ± 0.14	0.507 ± 0.002	1.022 ± 0.002	74.4 ± 0.5	1.027 ± 0.002	73.2 ± 0.8

^a Sample LB/S.XXI 10-01R is the very tip (~0.03 g) of a 1 cm-tall stalagmite, and sample LB/S.XXI 10-01 is a larger portion (~0.12 g) of the top section of the same stalagmite.

SUPPLEMENTARY INFORMATION section 5

Supplementary Table 7 | $^{40}\text{Ar}/^{39}\text{Ar}$ dating of tephra T1

Laser step-heating experiments on hornblende crystals of 100–150 μm (Lab ID 2598) and 150–250 μm (Lab IDs 2584 and 2599) size fractions. All uncertainties are expressed at 1σ .

Lab ID ^a	Relative argon isotopic abundances (V)					Ca/K	% ⁴⁰ Ar* ^b	Age (kyr)
	⁴⁰ Ar	³⁹ Ar	³⁸ Ar	³⁷ Ar	³⁶ Ar			
QL-OSU-28B; J = 0.0000170 ± 0.000000097								
2584-03C	3.256E-03	4.837E-06	2.157E-06	7.360E-05	1.090E-05	29.82 ± 0.69	0.36 ± 1.07	77 ± 226
	± 1.6E-06	± 7.8E-08	± 4.9E-08	± 1.2E-06	± 1.2E-07			
2584-03D	4.573E-03	1.080E-05	3.197E-06	2.494E-04	1.500E-05	45.13 ± 0.60	2.36 ± 0.71	314 ± 95
	± 1.7E-06	± 1.0E-07	± 5.7E-08	± 2.3E-06	± 1.1E-07			
2584-03E	5.543E-03	2.070E-05	4.066E-06	5.540E-04	1.830E-05	52.47 ± 0.48	2.42 ± 0.74	205 ± 62
	± 2.5E-06	± 1.3E-07	± 6.1E-08	± 3.6E-06	± 1.4E-07			
2584-03F	7.297E-03	2.890E-05	5.583E-06	8.154E-04	2.420E-05	55.28 ± 0.47	1.88 ± 0.60	151 ± 48
	± 2.6E-06	± 1.7E-07	± 6.8E-08	± 4.9E-06	± 1.5E-07			
2584-03G	4.800E-03	2.280E-05	3.760E-06	6.673E-04	1.580E-05	57.47 ± 0.49	3.09 ± 0.73	207 ± 49
	± 2.0E-06	± 1.4E-07	± 5.6E-08	± 3.8E-06	± 1.2E-07			
2584-03H	2.187E-03	1.330E-05	1.901E-06	4.025E-04	7.423E-06	59.23 ± 0.71	0.13 ± 1.21	7 ± 63
	± 1.3E-06	± 1.3E-07	± 4.1E-08	± 2.7E-06	± 8.9E-08			
2584-03I	3.933E-03	2.040E-05	2.982E-06	6.073E-04	1.300E-05	58.26 ± 0.56	2.22 ± 1.24	136 ± 76
	± 1.9E-06	± 1.4E-07	± 5.5E-08	± 3.9E-06	± 1.6E-07			
2584-03J	1.389E-03	8.639E-06	1.193E-06	2.607E-04	4.556E-06	59.15 ± 0.84	3.57 ± 1.63	182 ± 83
	± 1.2E-06	± 9.7E-08	± 4.1E-08	± 2.3E-06	± 7.6E-08			
2584-03K	8.464E-04	3.697E-06	7.691E-07	1.186E-04	2.786E-06	62.86 ± 1.59	2.84 ± 2.66	207 ± 194
	± 1.2E-06	± 7.6E-08	± 3.8E-08	± 1.7E-06	± 7.5E-08			
2584-03L	2.774E-03	1.300E-05	2.184E-06	4.164E-04	9.315E-06	62.94 ± 0.76	0.95 ± 1.07	64 ± 73
	± 1.5E-06	± 1.2E-07	± 4.9E-08	± 3.1E-06	± 9.9E-08			
2584-03M	6.797E-04	6.673E-06	6.179E-07	2.026E-04	2.170E-06	59.52 ± 1.03	7.04 ± 3.13	228 ± 101
	± 1.0E-06	± 9.0E-08	± 3.5E-08	± 2.2E-06	± 7.1E-08			
2584-03N	5.103E-04	3.462E-06	4.225E-07	1.253E-04	1.706E-06	70.91 ± 1.75	2.12 ± 4.31	100 ± 203
	± 9.5E-07	± 7.3E-08	± 3.5E-08	± 1.6E-06	± 7.4E-08			
2584-03O fuse	2.763E-03	7.273E-06	2.101E-06	2.499E-04	9.193E-06	67.34 ± 1.07	1.36 ± 1.10	164 ± 133
	± 1.6E-06	± 8.9E-08	± 5.2E-08	± 2.5E-06	± 1.0E-07			
2584-04C	7.293E-03	1.030E-05	5.065E-06	1.397E-04	2.450E-05	26.63 ± 0.43	0.05 ± 0.54	11 ± 119
	± 2.5E-06	± 1.1E-07	± 7.1E-08	± 1.6E-06	± 1.3E-07			
2584-04D	9.496E-03	3.300E-05	7.086E-06	8.757E-04	3.140E-05	52.05 ± 0.42	2.06 ± 0.48	188 ± 44
	± 2.9E-06	± 1.7E-07	± 8.0E-08	± 5.4E-06	± 1.5E-07			
2584-04E	5.025E-03	2.370E-05	4.107E-06	6.836E-04	1.670E-05	56.62 ± 0.51	1.69 ± 0.78	114 ± 52
	± 2.2E-06	± 1.5E-07	± 6.4E-08	± 4.3E-06	± 1.3E-07			
2584-04F	4.745E-03	2.080E-05	3.757E-06	6.106E-04	1.580E-05	57.67 ± 0.55	1.66 ± 0.82	120 ± 59
	± 1.8E-06	± 1.4E-07	± 6.0E-08	± 4.0E-06	± 1.3E-07			
2584-04G	1.161E-02	5.680E-05	9.371E-06	1.656E-03	3.910E-05	57.16 ± 0.36	0.53 ± 0.47	34 ± 31
	± 3.2E-06	± 2.3E-07	± 9.2E-08	± 8.0E-06	± 1.8E-07			
2584-04H	3.670E-03	2.450E-05	3.186E-06	7.461E-04	1.210E-05	59.66 ± 0.53	3.05 ± 1.05	145 ± 50
	± 1.8E-06	± 1.5E-07	± 5.5E-08	± 4.8E-06	± 1.3E-07			
2584-04I fuse	4.365E-03	9.898E-06	3.342E-06	3.200E-04	1.460E-05	63.36 ± 0.80	0.75 ± 0.81	105 ± 114
	± 1.8E-06	± 9.3E-08	± 5.8E-08	± 2.7E-06	± 1.2E-07			
QL-OSU-28C; J = 0.0000170 ± 0.000000045								
2598-01D	2.785E-03	1.350E-05	2.311E-06	4.324E-04	9.122E-06	62.61 ± 0.66	3.46 ± 1.10	226 ± 72
	± 1.6E-06	± 1.2E-07	± 4.5E-08	± 2.2E-06	± 1.0E-07			
2598-01 fuse	2.263E-03	1.450E-05	2.006E-06	4.795E-04	7.599E-06	64.79 ± 0.74	1.43 ± 1.29	71 ± 64
	± 1.4E-06	± 1.4E-07	± 4.5E-08	± 2.8E-06	± 9.7E-08			
2598-02D	2.421E-03	1.580E-05	2.096E-06	4.793E-04	7.926E-06	59.54 ± 0.62	3.86 ± 1.31	188 ± 64
	± 1.5E-06	± 1.4E-07	± 4.5E-08	± 2.4E-06	± 1.1E-07			
2598-02 fuse	6.454E-03	4.370E-05	5.740E-06	1.487E-03	2.150E-05	66.67 ± 0.40	2.61 ± 0.68	123 ± 32
	± 2.1E-06	± 1.9E-07	± 6.6E-08	± 5.9E-06	± 1.5E-07			
2598-03D	1.947E-03	1.480E-05	1.658E-06	4.712E-04	6.613E-06	62.22 ± 0.61	0.56 ± 1.23	23 ± 51
	± 1.3E-06	± 1.3E-07	± 4.5E-08	± 2.3E-06	± 8.0E-08			
2598-03 fuse	5.091E-03	3.200E-05	4.339E-06	1.069E-03	1.700E-05	65.55 ± 0.47	1.72 ± 0.75	87 ± 38
	± 2.0E-06	± 1.8E-07	± 7.7E-08	± 4.5E-06	± 1.3E-07			
QL-OSU-28C; J = 0.0000170 ± 0.000000035								
2599-01D	4.058E-03	1.870E-05	3.330E-06	5.869E-04	1.370E-05	61.51 ± 0.55	0.56 ± 0.99	39 ± 69
	± 1.9E-06	± 1.4E-07	± 5.2E-08	± 2.8E-06	± 1.3E-07			
2599-01 fuse	4.109E-03	2.640E-05	3.505E-06	8.389E-04	1.370E-05	62.33 ± 0.48	2.39 ± 0.92	119 ± 46
	± 1.8E-06	± 1.6E-07	± 5.5E-08	± 3.9E-06	± 1.3E-07			

^a Lab ID 2584-03M is the data point on the far right-hand side of Extended Data Fig. 3f, which was excluded from the inverse isochron used to calculate the $^{40}\text{Ar}/^{39}\text{Ar}$ age of 79 ± 12 kyr.

^b Radiogenic ^{40}Ar yield.

SUPPLEMENTARY INFORMATION section 6

Supplementary Table 8 | Radiocarbon (^{14}C) dating of charcoal

Charcoal pieces were recovered *in situ* (exact locations indicated by coordinates) and pretreated using acid–base–acid (ABA) procedures. Previous ^{14}C dating studies at Liang Bua have suggested that ABA pretreatment is more effective at reducing sample contamination by ‘old’ carbon (e.g., from dissolved limestone) than are less rigorous chemical pretreatments⁷. However, ABA procedures may not remove all sources of contamination by modern carbon, and the effect of such contamination increases with sample age⁶¹. For example, a 50,000 year-old sample contaminated with just 0.5% of modern carbon would give a measured age of ~40,000 years BP. Sample D-AMS 007548 falls in a challenging time period for ^{14}C dating, so the remaining charcoal from this sample was subjected to a more stringent cleaning procedure (AOx-SC), described in Methods. We consider the resulting age (OxA-X-2648-13) to be more accurate.

Sample code	Sector / depth (cm)	Coordinates (x, y, z)	$\delta^{13}\text{C}$ (‰) ^a	Conventional ^{14}C age (years BP) ^b	Calibrated age range (kyr cal. BP) ^c	
					68% CI	95% CI
D-AMS 007548	XXIII / 189	16, 76, 189	–22.2	40,417 ± 332	44.30–43.59	44.61–43.27
OxA-X-2648-13	XXIII / 189	16, 76, 189	–24.4	42,500 ± 900	46.56–44.91	47.66–44.13
D-AMS 005954	XXII / 431	76, 185, 431	–28.2	10,949 ± 42	12.79–12.72	12.87–12.70
D-AMS 005953	XXII / 432	65, 186, 432	–28.1	10,910 ± 36	12.76–12.71	12.80–12.70

^a Values for prepared graphite measured by AMS and used to correct the conventional ages for isotopic fractionation.

^b Radiocarbon years before present (BP) ± 1 σ , where ‘present’ is defined (by convention) as A.D. 1950.

^c Calendar-year age ranges reported at the 68% and 95% confidence interval (CI), with calibrations performed using the SHCal13 data set⁶² and CALIB 7.1 (<http://calib.qub.ac.uk/calib/>).